

Granular flow and design studies in flighted rotating drums

Dissertation

zur Erlangung des akademischen Grades

Doktoringenieur

(Dr.-Ing.)

vorgelegt von

M.Tech. Koteswara Rao Sunkara

geb. am 02.08.1984

in Guntur, Andhra Pradesh, India

genehmigt durch die

Fakultät für Verfahrens- und Systemtechnik
der Otto-von-Guericke-Universität Magdeburg

Gutachter:

Prof. Dr.-Ing. Eckehard Specht
Institute of Fluid Dynamics and Thermodynamics,
Universität Magdeburg, Germany.

Dr.-Ing. Jochen Mellmann
Department of Post harvest Technology,
ATB Potsdam, Germany.

Eingereicht am: 05.03.2013

Promotionskolloquium am: 11.07.2013

To my

Father

Preface

This dissertation is submitted to Otto von Guericke University, Magdeburg for the degree of Doctor of Philosophy. The research described herein was conducted under the supervision of **Prof. Eckehard Specht** and **Dr.-Ing. Jochen Mellmann** between October 2009 and March 2013. To the best of my knowledge, this work is original, except where suitable references are made to previous works. Neither this, nor any substantially similar dissertation has been submitted for any degree, diploma or qualification at any other university or institution.

Koteswara Rao Sunkara
Magdeburg, 04.03.2013

Acknowledgments

I would like to express my sincere gratitude to my supervisors **Prof. Dr.-Ing. E. Specht** and **Dr.-Ing. J. Mellmann** for providing me the opportunity to work with them and pursue a doctoral degree. Prof. Specht continuously encouraged me to finish this work successfully. His strong motivation and trust enriched my confidence levels helped me to finish my study in time. His friendly way of handling the research students has broken the communication barriers. He has provided free hand on whatever problem I would like to work.

Dr.-Ing J. Mellmann provided his valuable guidance to understand the concepts of granular studies. His valuable comments and suggestions during the discussions has encouraged my interest towards this subject. He has provided me ample information on each and every discussion. He continuously supported and encouraged to publish my work in various journals and proceedings. His way of dealing and understanding the problem has helped me to shape the structure of my work.

I feel immense pleasure in saluting the **Otto von Guericke University, Magdeburg** for giving me a great opportunity to pursue the research study in Germany. I would like to acknowledge the financial support provided by the **Graduiertenkolleg (GKMM)** through the **German Research Foundation (DFG)**. One word thank you is not sufficient to my colleague **Dr. Fabian Herz** who helped me during the discussions and also for experiments. His continuous support for both personal and professional life during the tenure of my work is invaluable. It is my fortunate to being a friend of the three Musketeers of Magdeburg Indians (**Dr. Ashok Kumar Nallathambi, Dr. Thirumalesha Chittipotula, Gourisankar Sandaka**) with whom I always share best moments of my life.

Its my duty to thank Dr.-Ing. Hermann Woche for his valuable technical support. I would love to thank our secretary Frau Hasemann for her continuous support during my tenure here in the administration part of the work. I would like to personally thank all

my colleagues for their encouragement and understanding.

Finally, I would like to express my sincere thanks to every individual German citizens for contributing either directly or indirectly. During my stay in Germany, I learned self discipline, punctuality and time management from the fellow citizens of Germany. Similarly, I would like to thank my home country and Indian Institute of Technology Madras. Further, I extend my thanks to Indian friends **Pavan, Narasimha**, B.V.K. Murthy, Priya, Sai bangaram, Nadine Lorenz, Tino, Hidayath, Siva Krishna, Surendra, Sri Hari, Madhav, Sameer, Sukumar, Polu, Latha, Ravi, Maya, Sanga mithra, and Deepthi.

Especially, I thank my mother who is the reason for my existence and establishment. I would like to thank my sisters and relatives for their continuous encouragement and support.

Abstract

The objective of the present work is to study the particle motion behavior in rotary drums operated with rectangular type flights. As the earlier works made less contribution to determine the optimal gas-solid contact area (curtains), the present study was focused towards maximizing the total particle surface area for a given flight shape at a constant drum loading. A theoretical model has been developed for this purpose, to provide optimum flight design by maximizing the amount of material in the airborne phase of the drum. Initially a model to determine the holdup and the cascading rate of the particles discharging from the flight surface was developed. Further using the unloading studies of the flight, the amount of material distributed into the airborne phase and the rolling bed can be estimated. An iterative scheme is developed to determine the filling degree of the rolling bed. Moreover the height of the curtain was also formulated from the geometrical approach for a over-loaded drum dividing the region of impact into two sectors.

A novel theoretical model for kinetic angle of repose is presented by considering a flowing layer at the flight surface, while the model of Schofield and Glikin neglected the inertial forces in the active layer. Further, an extended model is also proposed to determine the final discharge angle, as the comparison of the old models with the measurements showed a different tendency. The reason for this tendency of the old models are due to neglecting the inertial effects involved during the final flight discharge and approximated Final discharge angle as constant. Whereas it is incorporated in the extended model in order to trace the position of the last particle leaving from the flight by considering a particle layer when the surface of the flight sheet is opposite and parallel to the bed surface.

Experiments were performed with two drum sizes of 500 mm, 1000 mm in diameter and 150 mm, 300 mm in length respectively, which was furnished with rectangular flights around the inner shell of the drum. The flight numbers were operated at 12 and 18, while varying the flight length ratio (l_2/l_1) between 0 and 1.0 by maintaining l_1/R at 0.2.

The experiments were carried out with test materials (quartz sand, glass beads) having good flowability, and bulk material (limestone) having properties close to real materials. The action of the flights were recorded with high definition camera. Kinetic angle at various flight positions were determined by collecting the images from the recorded videos of the experiments. The model predictions depicted that the carrying capacity of the flight was increased while increasing the flight length ratio, but the discharge rate was decreased during the initial discharge. The validation of the model was carried out with different profiles of the flight by varying the tangential length (l_2). Good agreement has been observed between the model predictions and the experiments, for the test materials quartz sand and glass beads.

An example of an industrial dryer of length 6.1 m with a diameter of 3.35 m is considered to determine the influence of operating parameters such as Froude number, drum filling degree, flight length ratio, and number of flights. Influence of each of these parameters on holdup, cascading rate of the flight, and the total particle surface area was examined and presented in detail. This analysis can be used as a bench mark to the field experience during scale up of the drum.

Keywords: Rotary drum, Drying, Flights, Flight length ratio, Discharge rate, Number of flights.

Zusammenfassung

Ziel der vorliegenden Arbeit ist die Untersuchung des Verhaltens der Partikelbewegung in Drehrohren mit rechteckigen Hubschaufeln. Die für den Wärme- und Stoffübergang bedeutende Kontaktfläche zwischen Gas- und Feststoffphase wurde in bisherigen Veröffentlichungen nur unzureichend betrachtet. Diese Arbeit konzentriert sich auf die Optimierung der Gesamtoberfläche der Partikel für eine definierte Hubschaufelgeometrie bei konstanter Beladung. Hierzu wurde ein theoretisches Modell entwickelt, das zur Vorhersage der optimalen Hubschaufelgeometrie und Anordnung unter Maximierung der in der Flugphase befindlichen Menge an Partikeln verwendet werden kann. Zunächst wurde ein Modell zur Bestimmung des Hold-up und der Entleerungscharakteristik der Schaufel entwickelt. Auf Grundlage dieser Untersuchungen konnte die Partikelverteilung in der Gasphase und im unteren Schüttbett ermittelt werden. Zudem wurde die Höhe der Partikelschleier über die geometrischen Bedingungen und die Unterteilung des Querschnitts in zwei Bereiche bestimmt.

Es wird ein neues theoretisches Modell zur Bestimmung des kinetischen Böschungswinkels unter Betrachtung einer Fliebschicht an der Schaufeloberfläche präsentiert. Das Modell von Schofield and Glikin vernachlässigt die Trägheitskräfte in der aktiven Schicht. Zur Bestimmung des maximalen Entleerungspunktes wurde ein neuer Modellansatz hergeleitet, der im Vergleich zu vorherigen Modellen eine bessere Übereinstimmung zu den Ergebnissen der durchgeführten Experimente liefert. Ein Grund für die Modellunterschiede kann die Vernachlässigung der wirkenden Trägheitskräfte während der letzten Phase des Entleerungsvorgangs sein. Wohingegen die Berücksichtigung der Trägheitskräfte im Modell die Verfolgung des letzten Partikels beim Verlassen der Hubschaufel ermöglicht. Hierbei wird eine Partikelschicht betrachtet, wenn sich die Oberfläche des tangentialen Schaufelblatts parallel zur Schüttgutoberfläche befindet.

Es wurden experimentelle Untersuchungen in Drehrohren mit einem Durchmesser von

500 und 1000 mm sowie einer Länge von 150 und 300 mm durchgeführt. Dabei waren die Drehrohre mit 12 bzw. 18 rechteckigen Hubschaufeln bei gleichmäßiger Verteilung auf den inneren Umfang ausgestattet. Das Längenverhältnis der Hubschaufeln (l_2/l_1) wurde zwischen 0 und 1 bei konstantem l_1/R von 0,2 variiert. Die Versuche wurden mit Modellschüttgütern (Quarzsand, Glaskugeln) und realen Schüttgütern (Kalkstein) durchgeführt. Die Schüttgutbewegung wurde dabei mit einer hochauflösenden Kamera aufgezeichnet. Der kinetische Böschungswinkel wurde für verschiedene Positionen der Hubschaufeln aus dem Bildmaterial entnommen. Anhand des Modells wurde mit Zunahme des Längenverhältnisses eine höhere Fördermenge der Hubschaufeln vorhergesagt, allerdings verringerte sich dabei die Ausflussrate. Das Modell wurde mit unterschiedlichen Profilen der Hubschaufeln unter Variation der tangentialen Länge (l_2) validiert. Es konnte eine gute Übereinstimmung zwischen experimentellen Ergebnissen und Modellvorhersage für die Modellschüttgüter Quarzsand und Glaskugeln beobachtet werden.

Am Beispiel eines industriellen Trockners mit 6,1 m Länge und einem Durchmesser von 3,35 m wurde die Wirkung verschiedener Einflussgrößen wie Froudezahl, Füllgrad, Anzahl und Längenverhältnis der Hubschaufeln in einer Parameterstudie analysiert. Der Einfluss dieser Parameter auf das Hold-up, die Ausflussrate, und die Gesamtoberfläche der Partikel wurde untersucht und ausführlich dargestellt. Anhand dieser Analyse wurden die Praxistauglichkeit und die Genauigkeit des Modells für ein Scale-up nachgewiesen. Letztlich wurde ein Ansatz zur Bestimmung des maximalen Ausflusses hergeleitet. Der Vergleich zwischen den experimentellen Ergebnissen und Modellberechnungen bei Variation der Froudezahl wurde ebenfalls ausführlich diskutiert.

Schlüsselwörter: Drehrohre, Trocknung, Hubschaufeln, Schaufellängenverhältnis, Anzahl an Hubschaufeln, Ausflussrate

Nomenclature

a, b, c	constants given in Eqs. (4.31a) to (4.31c)	[-]
A_{11}	area of $\triangle FDC$ in Fig. 3.5(a), see Eq. (3.21)	[m ²]
A_{12}	area of $\triangle OAF$ in Fig. 3.5(a), see Eq. (3.21)	[m ²]
A_{2k}	area of the sections given in Fig. 3.5(b)	[m ²]
A_{cs}	total particle surface area of all curtains	[m ²]
$A_{cs,i}$	total surface area of the particles in i^{th} curtain	[m ²]
A_C	overall contact area between gas and solid	[m ² /m ³]
A_f^*	area of the circular segment \widehat{BA} in Fig. 3.5(b)	[m ²]
$A_{F,i}$	cross sectional area occupied by the material in the i^{th} flight	[m ²]
A_W	area of the wedge $\triangle OAE$ in Fig. 3.5(a), see Eq. (3.21)	[m ²]
d_p	particle diameter	[m]
D	drum diameter	[m]
f_B	filling degree of the solid bed	[-]
$f_{cs,\Sigma}$	total filling degree of the airborne phase	[-]
$\bar{f}_{cs,i}$	mean filling degree of one curtain	[-]
$f_{cs,i}$	filling degree of a single curtain	[-]
f_D	total filling degree of the drum	[-]
$f_{F,\Sigma}$	total filling degree of the active flights	[-]

$f_{F,i}$	filling degree of the material in the i^{th} flight	[-]
Fr	Froude number	[-]
g	acceleration due to gravity	[m/s ²]
G	gas flow rate	[kg/s]
\bar{h}_F	mean curtain height	[m]
H	Drum hold up	[kg]
H_0	hold up of the flight at horizontal position	[kg]
H_D	hold up of the dense phase	[kg]
h_F	height of the curtain	[m]
l_1	radial length of the flight	[m]
l_2	tangential length of the flight	[m]
l_2/l_1	flight length ratio	[-]
L	length of the drum	[m]
$\dot{m}_{F,i}$	discharge rate of one flight	[kg/s]
\dot{M}_a	mass flow rate in the active layer	[kg/s]
\dot{M}_s	mass flow rate in the plug flow	[kg/s]
$m_{cs,i}$	total mass of the particles in i^{th} curtain	[kg]
m_p	mass of the particle	[kg]
$m_{F,i}$	holdup of one flight	[kg]
N	Drum rotational speed	[rps]
n_F	number of theoretical flights	[-]
$n_{F,a}$	number of active flights	[-]
\mathbf{r}	position vector of the particle given by Eq. (3.52)	

r_H	distance from the center to l_1	[m]
r_p	radius of the particle	[m]
r_{HS}	distance from center to the tip of the flight	[m]
R	drum radius	[m]
t^*	dimension less thickness of cascade layer as in Eq. (4.4)	[-]
t_E^*	dimension less thickness of cascade layer at flight tip E	[-]
t	time	[s]
t_F	time of fall	[s]
U	overall heat transfer coefficient between gas and solid	[W/m ² /K]
\bar{v}_x	mean particle velocity in the cascading layer	[m/s]
v_φ	particle velocity in plug flow region	[m/s]
v_x	particle velocity in the cascading layer	[m/s]
$V_{F,i}$	volume occupied by the material in the i^{th} flight	[m ³]
x	Cartesian x-coordinate	[m]
y	Cartesian y-coordinate	[m]

Greek letters

α	flight angle, see Fig. 3.1	[rad]
α_s	drum inclination to horizontal	[rad]
β	angle in Fig. 3.1	[rad]
β_n	modified flight angle, see Eq. (4.1)	[rad]
γ	kinetic angle of repose	[rad]
γ_L	kinetic angle at the final discharge	[rad]
δ	discharge angle	[rad]

δ_{BE}	angle given in Eq. (3.86) and Eq. (3.87)	[rad]
δ_L	final discharge angle of the flight	[rad]
ε_A	characteristic angle given by Eq. (3.84)	[rad]
ε_B	filling angle of the bed	[rad]
ε^*	auxiliary filling angle, see Eq. (3.23)	[rad]
ζ_A	disengaging tip angle of the bed (Fig. 3.1)	[rad]
η	inclination of the boundary line	[rad]
Θ_A	dynamic angle of repose	[rad]
κ	auxiliary coordinate	[rad]
μ	coefficient of friction	[-]
μ_m	modified coefficient of friction according to Eq. (4.32)	[-]
ν	inclination angle between boundary line and bed surface	[rad]
ν_0	angle defined by equation (3.81)	[rad]
ρ	dimension less radial position of the boundary line	[-]
ρ_b	bulk density of the material	[kg/m ³]
ρ_s	density of the particle	[kg/m ³]
τ	mean residence time	[s]
φ	angular coordinate	[rad]
φ	auxiliary coordinate	[rad]
φ_A	angular coordinate at point A see Fig. 4.3	[rad]
φ_E	angular coordinate at point E see Fig. 4.3	[rad]
φ_w	wall friction angle	[rad]
ω	angular velocity	[rad/s]

Contents

Preface	iii
Acknowledgments	v
Abstract	vii
Zusammenfassung	ix
Nomenclature	xiv
1 Introduction	1
1.1 Granular matter and flow patterns	1
1.2 Industrial drying methods	3
1.2.1 Background of drying operations	3
1.2.2 Selection of dryers	4
1.3 Rotary dryers	6
1.3.1 Construction and operation	6
1.3.2 Influence of flight profiles	9
1.3.3 Influence of drum loading on drying rate	11
1.3.4 Design and Scaleup	14
1.4 Thesis outline	14
2 Literature review on flighted rotating drums	17
2.1 Geometrical models on transverse particle flow	17
2.2 Axial solids transport	20
2.3 Heat and mass transfer	25
2.4 Summary	27

3	Geometric model of transverse granular flow	29
3.1	Dimensionless parameters	29
3.2	Model assumptions	31
3.3	Granular flow at the flight surface	31
3.3.1	Model of Schofield and Glikin	31
3.3.2	Extended model	34
3.4	Flight holdup	36
3.5	Cascading rate of the flight	42
3.6	Model of the final flight discharge	44
3.6.1	Mellmann's Final discharge angle model	44
3.6.2	Extended Final discharge angle model	44
3.6.2.1	Assumptions	45
3.6.2.2	Rotating flight frame of reference	46
3.7	Theoretical number of flights	52
3.8	Maximum flight length ratio	53
3.9	Height and time of fall	54
3.9.1	Height of curtains calculation	54
3.9.2	Mean height of fall	57
3.9.3	Falling time	58
3.10	Gas-solid contact area	58
3.10.1	Effective particle surface area	58
3.10.2	Calculation of individual phases of drum	60
4	Modeling of granular transverse flow at flight surface	63
4.1	Analysis of transverse flow	63
4.2	Mathematical modeling	66
4.2.1	Coordinate system and variables definition	66
4.2.2	Velocity and Mass flow	68
4.2.3	Force balance in the active layer	69
4.2.4	Coefficient of friction	72
4.3	Simulation methodology	73
4.3.1	Initial conditions	73
4.3.1.1	Region-I: $0 \leq \delta \leq (\gamma + \alpha + \beta_n)$	74
4.3.1.2	Region-II: $(\gamma + \alpha + \beta_n) < \delta \leq \delta_L$	74
4.3.2	Solution procedure	76

5	Experimental Setup and Description	77
5.1	Experimental Setup and Procedure	77
5.2	Materials and conditions	79
6	Experimental measurements and model validation	83
6.1	Kinetic angle of repose	83
6.2	Flight holdup	87
6.3	Flight cascading rate	89
6.4	Final discharge angle	94
6.5	Theoretical number of flights	98
6.6	Height of fall	100
6.7	Surface area of the falling particles	104
6.8	Estimation of fractional filling degrees	106
7	Analysis and scale up	109
7.1	Analysis of experimental images	109
7.1.1	Number of rotations	109
7.1.2	Filling degree	110
7.1.3	Number of flights	112
7.1.4	Flight length ratio	112
7.1.5	Influence of type of material	114
7.1.6	Influence of moisture	121
7.2	Scale up to real dimensions	122
7.2.1	Froude number	122
7.2.2	Dynamic angle of repose	124
7.2.3	Filling degree	127
7.2.4	Flight length ratio	129
8	Conclusions and Outlook	131
8.1	Conclusions	131
8.2	Outlook	132
	Bibliography	143
	List of Publications	145
	Curriculum Vitae	147

Chapter 1

Introduction

1.1 Granular matter and flow patterns

Granular matter is referred as the collection of particulate material categorized as grain sizes larger than $1 \mu\text{m}$ [1, 2]. In day to day life we observe numerous granular products, for example, sand in hourglass, sugar, cereals, salt, cement, flour etc. Solid like behavior can be observed when these granules form piles, or they can behave like liquid during the flow from silos, and like gas when agitated [3, 4]. The subject of flow of these dry or wet granular materials having wide range of applications (see Fig. 1.1) in industrial processes is not simple to describe. The current knowledge of the granular flow studies is still not perfect when compared with the developed studies in the field of fluid flows [5]. The flow of granular matter can be classified into two categories: the flow confined between two surfaces (Fig. 1.1(a)-(c)) and the free surface flows (Fig. 1.1(d)-(f)) [6]. Free surface flows develop a flowing layer on top of a static bed which is slightly inclined to the horizontal. They have diverse applications in various industries as well as in the geological practice [7]. The applications include the transportation of dry/wet granules, processing in the rotary cylinders such as kilns/dryers, discharge from silos or land slides etc.

The heaps or piles formed by the granular material are stationary until the slope of the bed is less than the angle of repose [8, 9]. A flowing layer will be developed when the bed inclination exceeds this angle. In case of rotating cylinders the material is stable till the inclination of the free surface is less than the dynamic angle of repose (Θ_A) (see Fig. 1.2). Increasing beyond this angle leads to change the stability of the system and a continuous flow of the material is possible only after the maximum angle of stability. Distinct motion behaviors were identified for the granular matter with in the

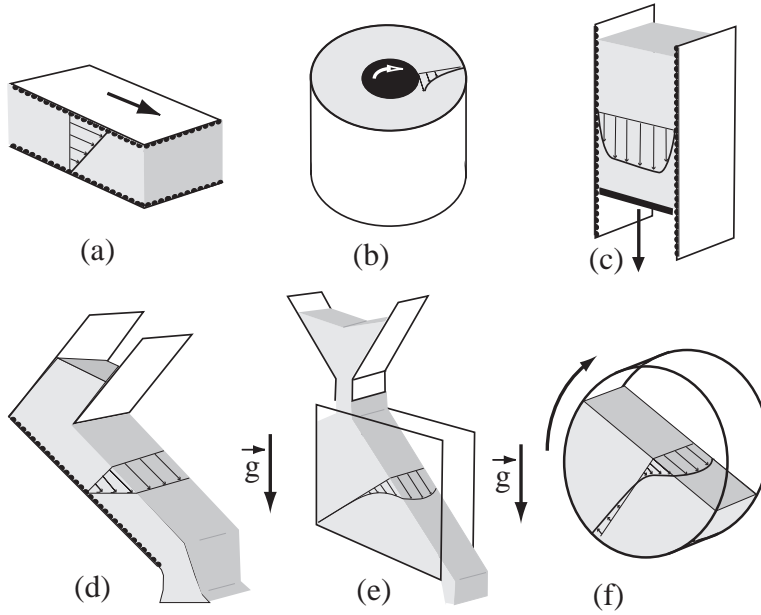


Figure 1.1: Applications of the granular flows: (a) plane shear, (b) annular shear, (c) vertical-chute flows, (d) inclined plane, (e) heap flow, (f) rotating drum [6]

transverse section of a rotating drum: slipping, slumping, rolling, cascading, cataracting, and centrifuging [10–12]. The kind of motion depends on the nature of the material, drum speed, filling degree, and roughness of the drum walls. The most common modes of motion behaviors occur for the industrial kilns are slumping and rolling [13, 14]. During the slumping mode the material oscillates between two angles, upper and lower angles of repose for every avalanche [15]. However, the avalanches are not continuous in this case. Increasing the drum speed progressively, increases the frequency of avalanches, which then leads to rolling motion by rolling down the particles continuously. The surface of the material becomes nearly flat for such motion behavior. This is the desired mode of operation in the industries for a better performance of the kilns, due to the fast renewal of the surface improves the mixing behavior. In rotary kilns the filling degree, and the characteristics of the material changes along the length of the drum. As a result, the rolling and slumping modes occur at different sections of the kiln depending on the filling degree. On the other side the rotating drums can also be used as dryers in order to dry the wet particulates in large quantities. The present study is confined to the design studies of rotary drums as dryers having wide range of applications in the industries.

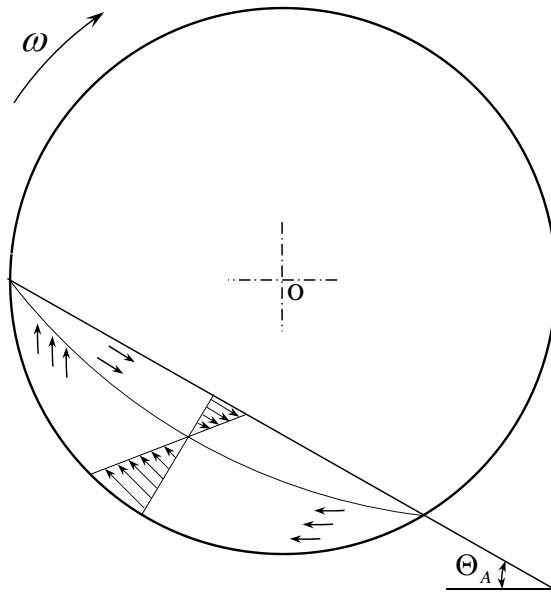


Figure 1.2: Solids motion in a rotating drum

1.2 Industrial drying methods

1.2.1 Background of drying operations

Drying of particulates is an energy intensive operation having a major industrial significance. Some reports suggested that 7-15% of the industrial energy is concentrated in drying operations for countries like United States, UK, Canada, and France, whereas countries like Germany, Denmark is further extended to 15-20% [16, 17]. Since the significance of energy has been rising, it is necessary to develop the optimal solutions by providing minimum energy requirements. Most of the times, the particulates needs to be dried either during the initial or final stage of operations in the processing industries. The source of the wet particulates may be crystallizers, reactors, filters, or the material collected from mining etc. These particulates are wet up to 20-30% in weight, which must be often removed to a considerable extent before it is suitable for further use. In general, they are cohesive in nature and becomes difficult to handle them during the operation. They become free flowing again when being dried. Mostly the wet particulates needs to be dried to remove water, however in some cases valuable solvents has to be recovered from these particulates carefully.

Various methods are available for removing the moisture from the particulates. The common methods of drying are dewatering techniques like natural drying operations by

exposing the material to the atmosphere in a closed or open chamber for several days or drying the material continuously by supplying the external heat source. There are variety of feedstocks available for drying operations that varies from slurries, pastes to free flowing granular materials. Drying of these materials is important for easy transportation, to attain the desired quality of the product or storage for longer durations. As a result a number of drying equipments had been developed during the past century depending on several factors. The decision of selection of a dryer for a specific operations is very critical and necessary precautions needs to be made carefully which is discussed in the following section.

1.2.2 Selection of dryers

If the material to be dried is new then the designer does not have any prior experience about the behavior of the product in the drying equipments. In such cases, by making simple tests in the lab to understand the drying characteristics and the small scale tests would become bench mark to scale up for the industrial operations. A preliminary selection of the kind of dryer is usually made on the basis of production capacity and the properties of the drying material. The selection of the dryer for a given material is a difficult task in the industry which needs to be analyzed carefully from the following points [18]

- Production capacity
- Initial moisture content
- Particle size distribution
- Drying curve
- Maximum allowable product temperature
- Corrosion aspects
- Thermal/mechanical sensitivity
- Toxicological properties.

Van't Land [18] provided an outline for the selection of batch or continuous dryers. Batch dryers are more suitable when the production capacities are small (<200 kg/hr) [19]. It can handle variety of materials with different drying characteristics in the same system.

The choice between the batch dryers and the continuous dryers primarily depends on the kind of feedstock. The most commonly used batch type dryers are fixed bed dryer, tray dryer, agitated pan dryer, vacuum tray dryer, and agitated vacuum dryer. Vacuum dryers are more suitable when the product temperatures are not allowed to exceed 30°C, or when the recovered solvent is toxic. Tray dryers are more applicable for very fine and dusty materials with particle sizes smaller than 100 μm .

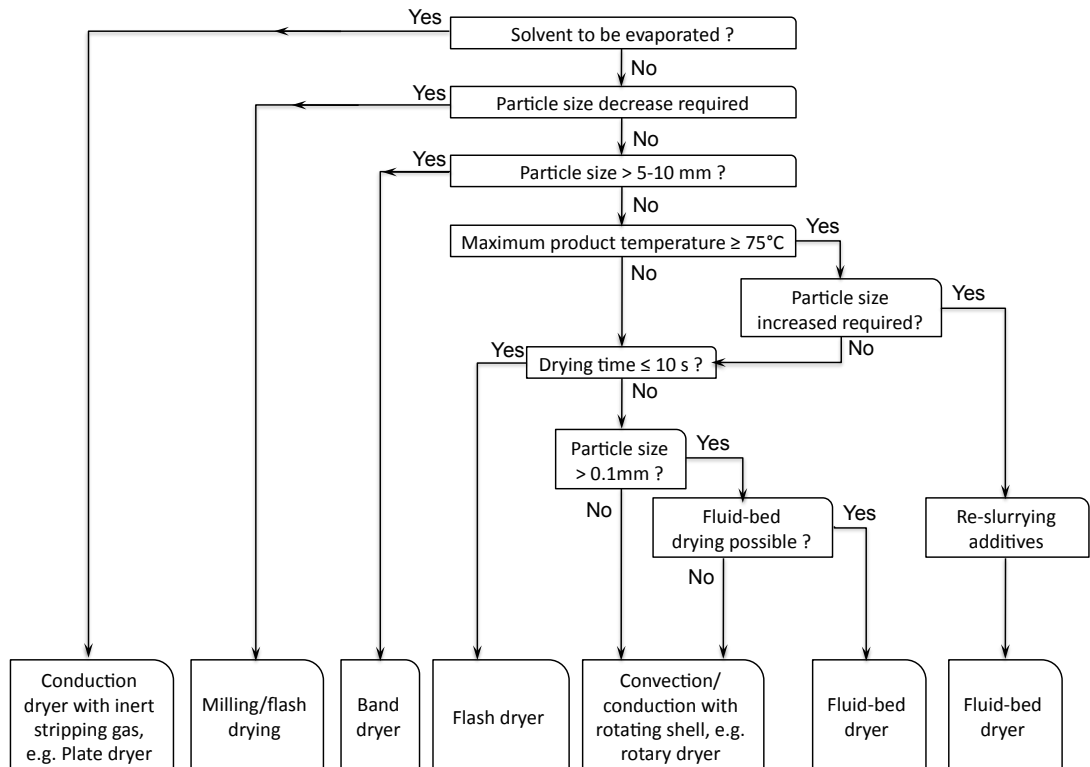


Figure 1.3: Decision tree for the selection of continuous dryers [18]

In general, the continuous dryers are easy to integrate into the process with minimum cost and less handling than batch dryers. The continuous dryers that are more important to the industry are rotary, fluid bed, flash, and spray dryers. Fluidized bed dryers can be used to treat for heat sensitive materials due to its ability to accomplish high heat transfer rates. Flash dryers are used to treat nonporous particulate feeds. Rotary dryer is probably the workhorse of mineral processing industries where large and broken solids have to be processed. Figure 1.3 describes the flow sheet for selection of these dryers based on feedstock and drying characteristics. In the following section we describe about the rotary dryers and their applications. The objective of the present thesis is to provide

detail understanding of the material distribution in rotary dryers which can be coupled with the field experience to design the dryer.

1.3 Rotary dryers

1.3.1 Construction and operation

Rotary dryers are one of the most commonly used devices to dry granular or particulate material due to its ability to handle wide range of feed stocks providing large throughputs. They are often used in mineral, food, sugar, fertilizer, and metallurgical industries to remove the moisture from the humid material and raise its temperature [20–26]. Especially in mineral industries such as nickel, the ore collected from the mining approximately contains 15-20% of moisture which has to be dried before passing as feed to the kiln where the reduction of nickel takes place. The unit can also accept sticky and the heat sensitive materials. These dryers are long cylinders rotated axially and slightly inclined (approx. $0-5^\circ$) to the horizontal [27–29]. The size of these dryers vary from 2 m in length and 0.3 m in diameter in pharmaceutical industries to 120 m long and diameters of 6 m in mineral ore industries. One such dryer during the manufacture is shown in Fig. 1.4. The process and operating parameters of these dryers are presented in the Table. 1.1. The mechanical construction of these dryers is complicated but easy to understand as compared to other dryer types, however the maintenance requires more manual effort. The maintenance cost of these dryers can reach up to 10% of the investment cost per annum.

The wet feedstock to be treated is introduced at the upstream side of the kiln and the dried product is collected at the downstream end (Fig. 1.5). In general, the rotary dryers can be classified based on the method of heating, such as direct and indirect rotary dryers. In a direct heat dryers the wet feed is in direct contact with the hot air. It can be further classified based on the direction of flow of solids and the hot gases: (a) cocurrent (b) countercurrent and (c) cross flow (e.g. Roto-Louvre dryers). In indirect heat rotary dryer the heat transfer occurs indirectly to the wet solids. The energy source comes either from a high pressure steam or by the natural gas or oil passing through a series of tubes surrounded to the circumference of the drum. The construction of this type is more complicated than the direct contact dryers, however the heat losses to surroundings can be minimized in this case [18, 34].

Mostly the rotary dryers are equipped with longitudinal fins/flights attached to the

Table 1.1: Process and operating parameters from literature

Parameter	Williams-Gardner [30] (1971)	Kneule [31] (1975)	Kröll [32] (1978)	Green and Perry [33] (1997)
Geometrical				
Diameter	[m]	0.5 ... 4	0.3 ... 5.5	<0.3 ... >3
Drum length	[m]		2 ... 35	
L/D	[-]	4 ... 6	4 ... 8	4 ... 10
l_1/D	[-]	4 ... 10		0.08 ... 0.125
r_H/R	[-]	0.08 ... 0.125		0.75 ... 0.83
n_F	[-]	0.75 ... 0.83		(7.8 ... 10)*D
		(6.5 ... 13.1)*D		(D [m])
		(D [m])		
Operating				
Rotational speed	[rpm]	1 ... 15	1 ... 15	0.25 ... 0.5
Froude number	[-]	0.005 ... 0.03	0.003 ... 0.04	0.004 ... 0.04
Drum inclination	[°]	0 ... 4.6	0 ... 5.7	0 ... 4.6
Filling degree	[-]	0.1 ... 0.12	<0.1	0.1 ... 0.15
Residence time	[min]		10 ... 150	
Gas velocity	[m/s]	4 ... 5		
Gas mass flow rate	[kg/m ² /s]	0.22 ... 10.7		
		0.27 ... 13.6		



Figure 1.4: Direct heat rotary dryer during manufacture [18]

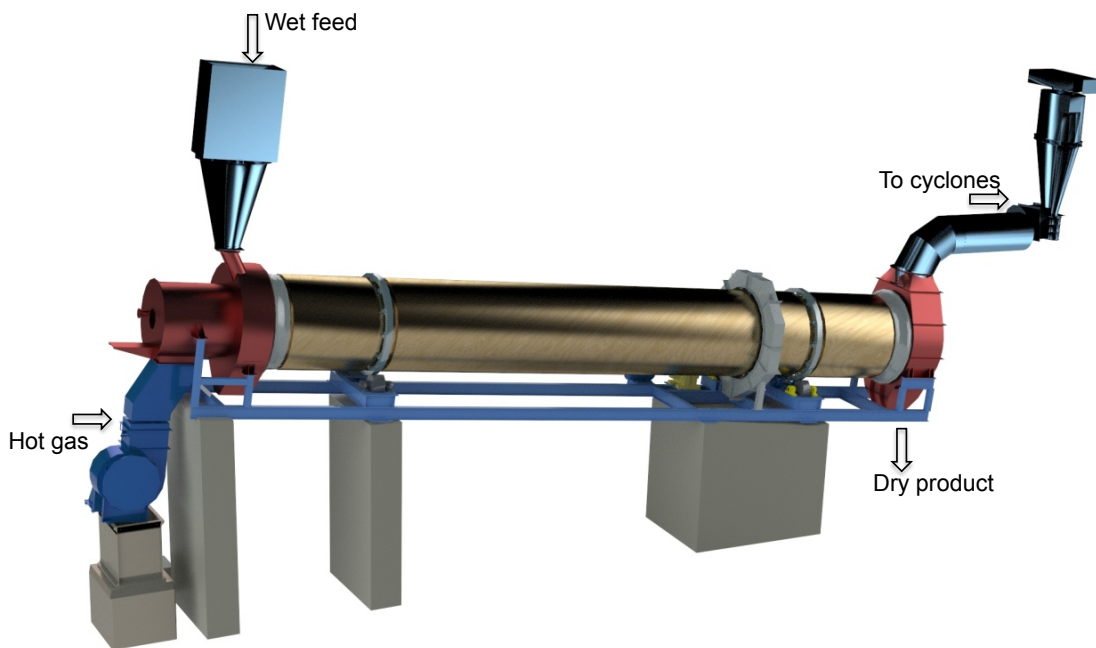


Figure 1.5: Direct contact cocurrent rotary dryer

wall of the drum. As the drum rotates the flights lift the solid material up to certain distance to shower them across the free gas stream [35–38] by developing a series of curtains. In direct contact dryers hot gas is passed through the drum which provides

enough heat to vaporize the moisture from the showering solid particles. The material falling from the flight is advanced to a specific distance in each cascade depending on the gas flow and various flight actions such as bouncing, and kilning. Due to the inclination of the drum and the action of the flights, the material is transported to the other end of the dryer. The material within the drum has been exposed to three different phases during the drying process as illustrated in Fig. 1.6. The dense phase at the drum bottom, dense phase or soaking period in the flights, and the airborne phase where the material is exposed to hot air.

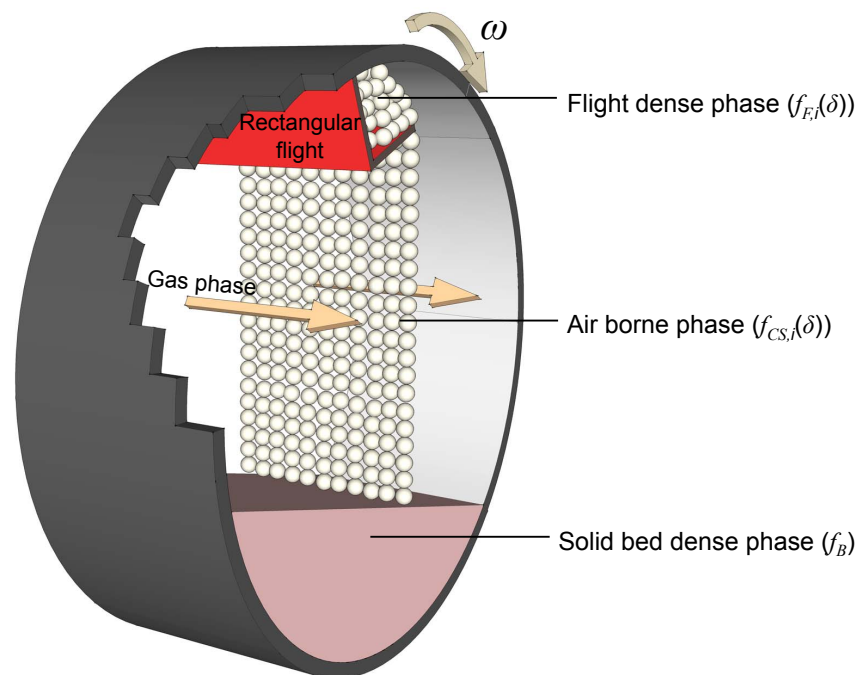


Figure 1.6: Different phases of the solids in the flighted rotary drum

1.3.2 Influence of flight profiles

The effectiveness of the flighted rotary drum greatly depends on the extent and uniformity of the gas-solid contact and the residence time of the material in the dryer, which in turn depends on the number, size and shape of the flights. The selection of the shape of the flight is largely governed by the behavior of flow of the particulates. The most commonly used flight profiles are shown in Fig. 1.7. In general, rectangular flights are mostly used for free flowing bulk materials. Radial flights are used for sticky materials and circular flights are applicable for developing a uniform distribution of the particulates.

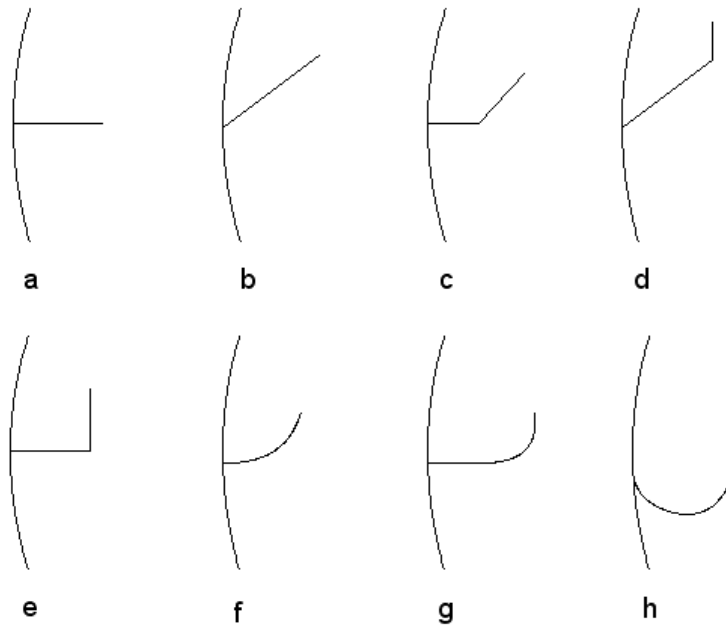


Figure 1.7: Common flight profiles: (a) radial flights, (b-d) angular flights, (e) rectangular flight, (f-h) circular flights

Different flight shapes are employed in the standard dryer designs to accommodate the change in flow properties of the material during the drying along the length of flighted rotary drum [39]. Radial flights with 0° lip are employed in the first third of the drum from the feed section, flights with 45° lip are used in the second third of the drum, whereas the rectangular flights are equipped when the material becomes free flowing at the discharge end [40]. The uniformity of the flying curtains may be attained by providing an offset between the flights along the drum length for every 0.6 m to 2 m. The cross sectional image of an industrial rotary drum with interior flight arrangement is shown in Fig. 1.8. In some cases, the spiral flights are used for few meters at the feed section of the drum for a quick forward flow of the feed from the chute or conveyor to prevent leakage of the material. Long chains are attached under the flights in order to scrape the sticking solids, however these chains contribute significantly for the heat transfer leads to use another mechanism. The effective way of removing the solids sticking to the flights can be done by using external shell knockers. Use of internal flights in the rotary dryers, increases the difficulties of maintenance due to the less space available for any person to enter and clean the inner shell of the drum. Sometimes the flights can be omitted before the discharge of the product in order to avoid the excessive solid entrainment by the gas

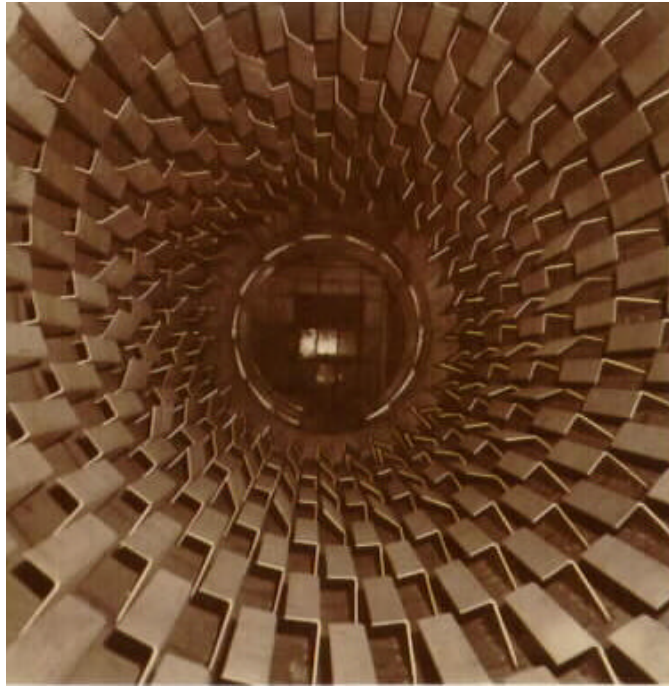


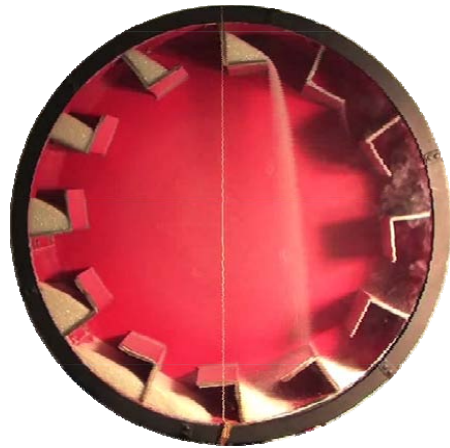
Figure 1.8: Cross sectional view of rotary dryer with flights (Swenson, Inc., Harvey, Illinois)

in cocurrent operation of the gas-solid system [30].

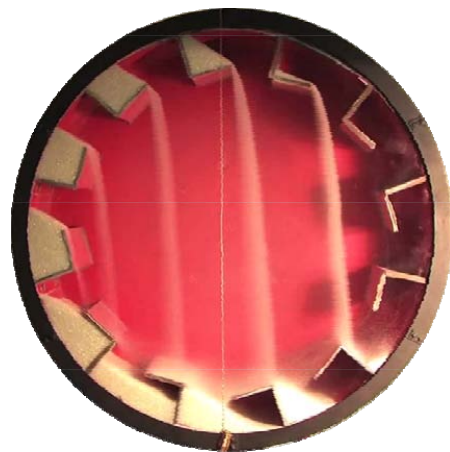
In general, the flight should be occupied to its maximum extent so that the formation of curtains can occur when the flight is in the upper half of the drum. The flight elevate the material and cascades into the airborne phase. This happens to be a periodic process where each individual particle in the airborne phase is exposed to hot conditions thus increasing the rate of drying. Therefore, the performance of the drum mainly depends on the amount of material in this phase which is controlled by the design and the number of flights. Other parameters that also influence the rate of drying: residence time, drum speed, gas velocity, and drum inclination. For a proper design of the flight the entire cross section of the drum should be covered with a shower of material.

1.3.3 Influence of drum loading on drying rate

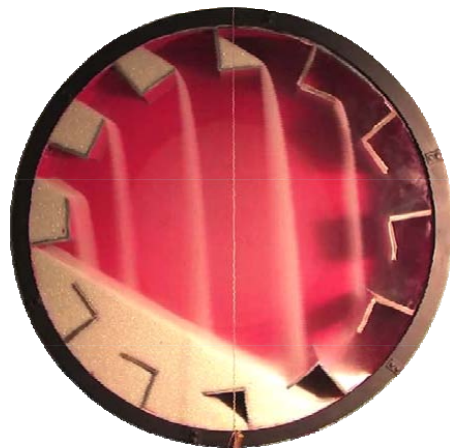
There are three different states of the drum loading that can be observed within the rotary dryer, which is characterized based on the first unloading of the flight [27, 41, 42]. If the flight discharge starts when it is in the upper half of the drum, it is said to be under-loaded. In such conditions, the time spent by the particles in the airborne phase is



(a) Under loaded



(b) Design loaded



(c) Overloaded

Figure 1.9: Different loading conditions of flighted rotary drum

minimum, which can lead to smaller residence times than required. This kind of loading is illustrated in Fig. 1.9(a). As the loading state of the drum is gradually increased, first unloading position of the flight is ultimately decreased and at some point the unloading starts when the flight tip is at 0° . At this point the drum is said to be design-loaded (Fig. 1.9(b)). In this case maximum amount of material is distributed in the airborne phase, hence the maximum heat transfer can be expected between the solids and the hot gas stream. Further increasing the feed rate does not increase the airborne solids, but the flight is completely crowded with the material which is defined as over-loaded drum (Fig. 1.9(c)). The discharge of the material in this case starts immediately as the flight tip detaches from the bed surface. Increasing the drum loading further can only roll the material in the lower half of the drum but the flight can not increase its carrying capacity. Hence, increase in drum loading increases the bed height thus decreasing the falling height of the material further reducing the drying rate. Therefore the efficiency of the dryer depends on the uniformity of the material distribution over the dryer cross section.

The key design parameters having influence on the material distribution include: diameter of the drum (D), geometrical parameters of the flight (l_1 , and l_2), total number of flights (n_F), material properties such as the particle diameter (d_p), dynamic angle of repose (Θ_A). All these parameters affect the heat transfer in the dryer. The particles falling, sliding into the drum space may develop fine fragments after impacting the shell or flight sheets, since the fall height is almost equal to the drum diameter which results the dust to escape with the exhaust gas. Therefore these dryers must be operated in such a way that the excessive dusting should not take place and the material should stay enough time in the drum for uniform drying otherwise it can result non uniform drying. Entrainment of fine particles in the system like large drying equipments is a great challenge for the designers to accomplish a balance between the dryer performance and economical situations. As increase in the drum diameter or decrease in the particle size will lead to excessive dust, which must be accounted during the design. In some industrial dryers the dust can be recovered by employing cyclones or bag collectors at the discharge end of the drum. The recovered material may be a fine particles or highly expensive materials which can be introduced into the process by recycling into the feed section again [40]. On the other side increasing the number of flights increases the number of curtains which in turn increases the gas-solids contact area. However increasing or decreasing this number solely depends on the flight geometry. As increasing the tangential length

of the flight, this number decreases consequently the number of curtains, whereas the final discharge angle increases. As the final discharge increases the material distribution in the upper half of the drum increases which in turn also increases the contact area. Therefore, there exists an optimal solution for the gas-solid contact area which is the primary objective of the present work.

1.3.4 Design and Scaleup

Design of any dryer for drying of an existing product with the help of the earlier experience is easy. However, drying of new material in rotary dryers is a challenging task due to the lack of previous experience in handling the feedstock. Therefore, initially the drying characteristics of the material needs to understand by performing simple bench scale tests. The test data collected from the experiments carried out in a pilot plant will serve as a bench mark with the field experience of the rotary dryers to scale up from the pilot plant to the production scale.

The pilot plant experiments will be performed to understand the material distribution for different design parameters, solid transportation, and heat and mass transfer studies. Since there are many operating parameters that influences the quality of the product, large number of tests need to perform to know the effect of design parameters. Hence a mathematical model can be developed by representing the ideal behavior of the dryers which can be then used to simulate for the production scales after validation of these models. In order to validate the model, dried materials with ideal flow behavior will be selected to collect the test data from the bench scale experiments. During the scale up of the drum, the scaling of flight design should maintain constant and the Froude number of both the pilot plant and real scale must be same [41].

1.4 Thesis outline

The objective of the present thesis is to study the rectangular flight design to enable uniform material distribution which can be used as a bench mark to scale up from the pilot plant to industrial sizes. For this purpose, a mathematical model is developed to determine the dense phase of the flights which is used to predict the unloading behavior of the flights. Geometrical approach has been followed for this purpose. As the flight unloading characteristics primarily depends on the kinetic angle of repose, hence more attention is devoted to extend the model of Schofield and Glikin [43] by incorporating

the inertial force at the flight surface. Further, the geometrical model is extended in order to predict the total surface area of the particles in the airborne phase and different phases of the drum using the basic principles which is presented in detail in Chapter 3. Chapter 4 is devoted to obtain the flow behavior of the active layer at the flight surface. Eulerian approach has been followed by considering the granular flow as continuum. The mathematical formulation and the solution procedure is presented in detail. In Chapter 5, the description of the experimental setup and the parameters operated for the experiments has been discussed.

Validation of the extended model of kinetic angle of repose, and the geometrical model are addressed in Chapter 6, for different flight designs (rectangular shape) at various rotational speeds, filling degree and different flight numbers. In Chapter 7, the analysis of the experiments for different materials and their unloading behavior has been studied with the aid of images collected for different conditions. The scaling of the drum to the industrial dimensions along with the parametric study is also discussed.

Chapter 2

Literature review on flighted rotating drums

Research on rotary dryers has evolved continuously from past few decades. Many research articles had been published till date on the subject of the flighted rotary drums involving various applications. Due to its wide range of industrial applications a significant contributions had been made understanding these units both theoretically and experimentally. Simple models to complex physical models are available in the literature to describe them mathematically. The literature on this subject has been divided into geometrical models, residence time studies, empirical relations on heat and mass transfer effects. The review of the articles in the context of each subject is presented in this chapter.

2.1 Geometrical models on transverse particle flow

A large amount of contributions had been devoted to predict the solids transport in rotary dryers. Various geometrical models were developed to demonstrate the discharge characteristics of a flight [44–47]. The quantity of material present in the flight at any given position can be traced if the surface angle of the material over the flight is known. This angle is named as the kinetic angle of repose (γ). Many researchers attempted to predict the kinetic angle as a function of the flight position. The angle was first calculated by Schofield and Glikin [43] by balancing the forces acting at the tip of the flight while neglecting the thickness of the material flowing over the tip. The resultant force balance equation had been validated with the experimental drum filled with glass spheres [44]

and pumice granules [45], by taking the photographs of the drum. The angle of repose is calculated from the resultant images and compared with the theoretical values of it. It was suggested that the practically operated range of Froude numbers for rotary dryer is in between 0.0025 to 0.04 [46]. However, the deviations for this equations were observed only for Fr above 0.4 [44]. The experimental setup of Kelly [48] consists of a rotary drum which has eight circular flights mounted at an equal angular distance of 45° around the internal circumference of the drum as shown in Fig. 2.1. The kinetic angle was calculated from the images for various conditions (particle size and drum speed), which is used further to compute the kinetic coefficient of friction. It was found that as the particle size decreases below $500 \mu\text{m}$, the friction coefficient also decreases, however above this range it is constant. Recently Lee and Sheehan [49] proposed that this angle maintains a linear relation with the rotational speed of the drum which is presented in empirical form.

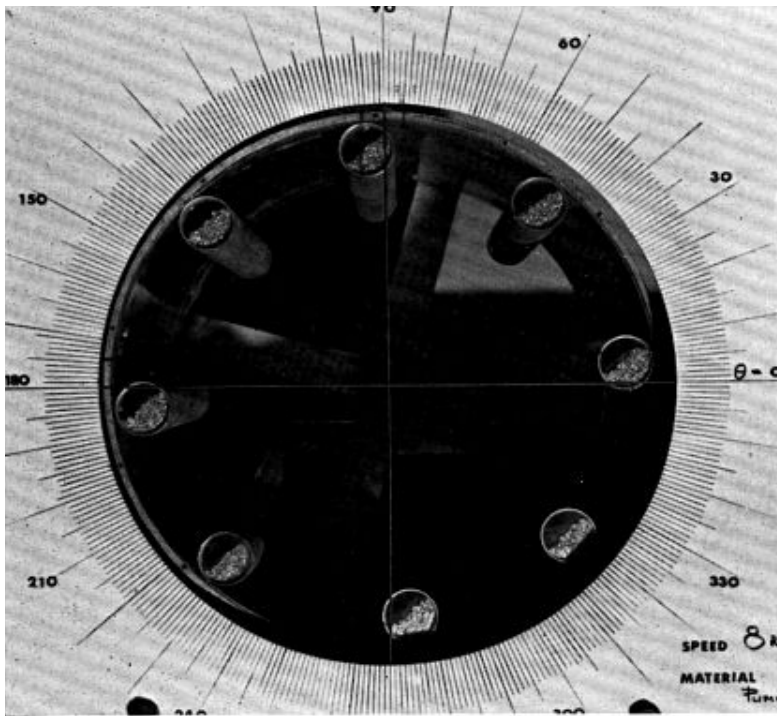


Figure 2.1: Experimental setup of Kelly [48] to measure kinetic angle

The holdup of a single flight as a continuous function of the tip angle was formulated with geometrical approximations to demonstrate the particle distribution velocities through the drum [46]. The average approach technique had been followed by Glikin

[46] to predict the mean height of fall. Baker [37] successfully extended this work to compute the holdup of the angular and extended circular flights. The maximum number of flights to be installed for a given design of the flights were also investigated in his study.

These studies had shown that the researchers concentrated primarily on the design of the angular flights with two segments alone. Kelly [50] proposed a method in order to get the optimal and equal distribution of the particles over the drum cross section with an idealized flight profile named as Equal Horizontal Distribution flights. The design of this flight is done on the basis of discharging equal quantity of material between any two discrete locations. This will improve the efficiency of the dryer, however it was not practical to implement in the industries for sticky and wet materials. Also the complex structure of the flight is complicated to manufacture. The design of the flights with three segments was the study of Revol et al. [51]. A generalized model was developed to find the holdup and flux of solids, which can also be implemented to two segmented angular flights. This study had been further used to predict the power required to elevate the solids. This model showed poor validation with the measurements towards the solid flux, which the authors opined due to the influence of the flight geometry on the surface angle.

Wang et al. [52] addressed some issues regarding the average value approach which is insufficient at high deviations over the mean value, and pointed that no model has been developed to describe the behavior of the flights with arbitrary geometry. A model has been developed in order to address these issues for particle transport in the flighted rotary drums using differential approach. The change in cross sectional area of the material in the flight had been used to predict the discharge rate of the flight. An outline was also proposed for the optimization problem to achieve the maximum drying efficiency, which is again an open challenge for the next investigation. The calculated discharge flow rate was validated with the experiments and it is found that the measurement errors are as high as 33% which can not be regarded as acceptable. The average porosity and width of the curtains have been calculated theoretically based on these studies. Wang et al. believed that the retention time has the influence of bouncing and kilning actions and needs to be implemented in the model. A normalized model was developed by linearizing the flight holdup as a function of angular position to depict the discharge characteristics of particles [53].

Recently Van Puyvelde [54] described a GFRLift model to predict the holdup profile of the complex geometries. The area occupied by the material in the lifters had been predicted based on the geometrical analysis by approximating the influence of arc of the

cylindrical drum as linear. He observed that an inclined flight holds higher amount of material when compared to the one perpendicular to the drum wall. The radial lifters attain higher solids flux when compared to any other flights that were presented in his study. Lee and Sheehan [49] also developed a geometrical model to determine the holdup and unloading profile of two segmented flights. They pointed that the model was sensitive to the mean angle of repose and it should be measured accurately in order to eliminate the experimental errors. The experiments were performed to find the mass flow rate of the solids discharging from the flight using four 50 kg button load cells. They found fluctuations in the discharge of the flight from the experimental images which depict that the unloading of the flight is not a continuous process. These fluctuations are independent on the drum speed and the flight position.

Image analysis techniques had been followed in order to estimate the optimum loading of these drums [42]. The authors presented four different approaches to predict the design loading of the flighted rotary dryers: visual analysis approach, gradient of total flight dense phase (both in upper half and lower half of the drum), saturation of the air borne phase, saturation of the total flight dense phase in the upper half of the drum, and saturation of the first unloading flight. The first approach involves the prediction of first discharge of the flight while operating at different loadings of the drum. The design loading is presumed to be the point at which the flight unloading starts when the tip of the flight meets the horizontal axis. This approach is a time consuming process and can mislead due to the fluctuating nature of the flight discharge. In the other cases, it was observed that the saturation of the air borne phase and the flight dense phase in the upper half of the drum produced similar profiles. However with these approaches more accurate prediction of these areas is necessary.

2.2 Axial solids transport

Mean residence time (τ) is a promisingly influencing parameter in rotary dryers which defines the quality of the product. Smaller residence time causes uneven drying of the feedstock, whereas the higher residence times lead to over drying of the material which involves huge energy loss to the industry. Therefore it is necessary to investigate the optimal residence times of the particles which can provide the desired nature of the product. It can be defined as the average time spent by the particles from the feed end to the discharge end. It is dependent on the particle flow direction involving the solid-gas interactions and the movement in the dense phase (in flights and at the drum

bottom). The forward motion of the particles occurs by the combination of three different mechanisms [28, 55].

- Flight action

It occurs due to the lifting of material by flight and cascading into the gaseous stream. During this period the material falls freely under the influence of gravity to a distance almost equal to the drum diameter. In each cascade the material moves forward to a certain distance due to the drag by gas and the inclination of the drum.

- Kiln action

The forward movement occurs at the bottom half of the drum due to the rolling of the material on the flight surface or over itself. It can be observed more at higher filling degrees or if the number of flights increases.

- Bouncing

In this case, the forward motion of the particles occur due to the bouncing when the particles impact on the rolling bed or the flight sheets. This action can be noticed more in design loaded or under loaded drums.

Most of the earlier research had provided empirical [56] and theoretical models to describe the axial transport. Saeman and Mitchell [57] developed the following equations for retention time as a function of the gas velocity (u_g) and length of the drum (L).

$$\tau = \frac{L}{f(H)ND(\phi \pm mu_g)} \quad , \quad (2.1)$$

where, $f(H)$ is a cascade rate of the particles per one revolution of the drum, and it can vary from 2 for underloaded dryer to π for fully loaded dryer with small flights while H is flight holdup. Constant m is an empirical coefficient which depends on the nature of the material, it holds 0.005 for Ammonium nitrate in a 1 ft diameter dryer. N is the number of revolutions, diameter of the drum (D), and ϕ is the slope of the dryer ($\tan \alpha_s$). Positive symbol in the equation applies for cocurrent flow and negative symbol stands for counter current flow of the gas. Later, Matchett and Baker [27] extended this work by proposing similar kind of expression using a two phase analysis, but providing a relation

for the empirical constants $f(H)$ and m

$$\begin{aligned} \tau &= \frac{L}{f(H)ND(\phi \pm mV)} \quad , \\ \text{when, } f(H) &= \frac{a}{2Nt_a^* + 1} \quad , \\ m &= \frac{2t_a^*}{a_n D} \quad , \end{aligned} \quad (2.2)$$

where, t_a^* is the average time of fall under design loaded condition, a_n dense phase velocity number, and V is the velocity of the cascading particles. The relation between particle velocity (V) and gas velocity had been found from the measurements such that $V = Cu_g^n$, where $2.65 < n < 3.76$. The authors did not account the influence of the flight geometry and flight number.

Matchett and Sheikh [58] improved this two stream model by considering the influence of number and shape of the flights. The dense phase holdup has been modified by introducing a new constant Φ

$$\begin{aligned} H_D &= \Phi n_F H_0 \quad , \\ \text{where, } \Phi &= \frac{\int_{H_0}^0 \delta dH}{\pi H_0} + \frac{1}{n_F} \quad . \end{aligned} \quad (2.3)$$

The constant Φ is determined from the experiments for the underloaded and design loaded conditions, n_F is number of flights, and H_0 is flight holdup when flight angle $\delta = 0$. It is the function of flight geometry and number of flights. The mean residence time was determined from the total drum holdup (total dense phase (H_D), and airborne phase), and solids feed rate. Miskell and Marshall [59] found that the residence time is normally distributed by passing a radioactive tracer into a 140 mm diameter drum. Johnstone and Singh [60] proposed the following expression in order to show the dependency of drum characteristics on the average particle residence time

$$\tau = \frac{0.043(L\Theta_A)^{1/2}}{ND\phi} \quad , \quad (2.4)$$

where, τ is mean residence time (min), Θ_A is dynamic angle of repose of the material ($^\circ$). The significance of the constant in the equation includes the influence of the flights in rotary drums. This equation is only valid for the dryers without any gas flow, since there is no term included in the equation which can incorporate the effect of gas flow, therefore

it over predicted the residence times. This model is the extension of the earlier works of Sullivan et al. [61], where he proposed the similar equation for rotary dryers without flights. The authors primarily concentrated on the solid transportation but without considering the effect of gas flow.

Kamke [62] investigated the axial displacement of the particles due to the influence of the gas flow. Mostly his study had concentrated on the drag force acting on single particle by the gas stream and these studies over predicted the non-ideal characteristic nature of the rotary dryer, where the particles are being prevented to be displaced from the gas stream due to the shielding effect offered by the neighboring particles. Sherritt et al. [63] performed experiments in a wind tunnel by pouring the particles forming curtains into a gaseous stream in order to address the shielding effect of the curtains. A velocity correction factor for gas velocity was introduced to incorporate this effect. Due to the developing trends of the continuum approaches for the fluid systems focused to apply for the granular and gas flow systems. Therefore these approaches had been successfully applied for a single curtain by considering the gas as a continuous fluid phase and the solid phase as a dispersed phase [64, 65].

Kamke and Wilson [66] proposed a model to predict the retention time also by considering drag acting on a single particle. The longitudinal advancement of the particle x_l per cascade was given by the following expression

$$x_l = u_g t_F + \frac{1}{K} \ln \left\{ \frac{\cos(\tan^{-1}(u_g/a_1))}{\cos(-a_1 K t_F + \tan^{-1}(u_g/a_1))} \right\} \quad (2.5)$$

where a_1, K are constants depending on the drum inclination and drag coefficient respectively. Using the above relation the total residence time can be determined by the total number of cascades times the sum of time of travel at flight surface and the time of fall. The model has been validated with an experimental drum of 1.2 m in diameter and 5.5 m in length, with six centered flights and 12 flights installed to the outer shell of the dryer. The experiments were performed with wood particles having a sphericity of 0.75 and exposed to hot gas stream in cocurrent passion. The retention time was measured by injecting a radioactive tracer particles at the inlet along with the feed. They noticed that within a curtain, the particles may be effected by the other particles and shielding of the gas flow can also occur. Due to this the model over predicted the data collected, since the model assumes that the particles are independent to the gas flow. They noted that the particles may be attributed as a bulk material and the mean diameter can be used

in order to measure the drag coefficient. It has been found that the root mean square error was 109.6% in the case of discrete particle size where as, in case of mean diameter it was around 14.2%.

Friedman and Marshall [28] studied the holdup and dusting in the dryer with various materials. Higher values of the holdup in the dryer was observed with the materials such as saw dust and wood chips for a given feed rate due to the higher values of angle of repose. They also investigated the effect of number of flights against the dryer holdup. In order to maintain constant dryer holdup, it is suggested that the feed rate should be decreased when the number of flights are increased.

A two stream model was developed by Matchett and Baker [27] in order to obtain a relation for the mean residence time of the particles in the drum. This was done by subdividing the material into two phases: airborne phase and dense phase. The flight borne solids and the solid bed at the bottom were considered as one single dense phase. However, this treatment was not sufficient enough to represent the behavior of the drum. Since, with this approach it is difficult to determine the quantity of material in the non-discharging flights accurately. Also, the authors neglected the bouncing and kilning mechanisms which are more dominant in under-loaded and design-loaded drums. Further, they also obtained a transition point from the experiments between the under-loaded and over-loaded drums, where this transition region was considered as the condition for design-loaded drums [67]. Sherritt et al. [38] proposed a model to estimate the contribution of each phase (dense phase of the solid bed, dense phase of the flights, and air borne phase) for over-loaded and under-loaded drums based on the surface length of the flight. The total holdup of the material at any cross section becomes the sum of the holdups of each phase.

In a recent study, Ajayi and Sheehan [26] proposed a method to estimate the design load of the flighted rotary drum experimentally using image analysis techniques. The design load condition was presumed to be the point of loading where the cross sectional area of initial discharge of the flight was saturated. They also presented an approach to determine the airborne phase by measuring the cross sectional areas of all the curtains the voidage of which they obtained from CFD simulations. It was found that the material in the air borne phase increased as the rotational speed increased.

However, these models were developed by assuming that each particle spend the same amount of time in the dryers, whereas in reality this is not true. In order to address these limitations the compartment models had been developed by dividing the dryer into

number of slices and that each slice is considered as combination of ideal reactors [68–71]. The solid transport takes place between each slice and this system can be considered as reactors connected in series. Duchesne et al. [68] proposed two models to represent the solid transportation within the dryer. The modified Cholette-Cloutier model was able to reproduce the dynamic nature of the particle transportation that occur in the real dryer system, which is further used to predict the bed depth and axial profiles. Sheehan et al. [72] extended this model by considering the material transport between the dense phase to the current and subsequent active phases. This model was able to give better predictions for the filling degree variations along the drum length. Recently a probabilistic approach had been followed by [73] to analyze the particle motion by combining the transition phase of the particle between the flights and axial movement. However, this approach had been applied to a very simple case of considering four radial flights and needs further investigation to employ for the industrial units.

2.3 Heat and mass transfer

Heat transfer in rotary dryers is a complex phenomenon due to the influence of different modes of transport mechanisms. It includes various transfer surfaces such as covered drum wall-contact bed surface, gas-exposed surface of the bed, gas-solids at the flight surface, and gas-solids in the airborne phase. Among all these mechanisms, the most significant heat transfer surface is the contact area between the gas-solids in the airborne phase. As in this case each solid particle in the curtain is exposed to the gas stream leading to rapid drying or cooling rates.

There has been numerous studies available in order to predict the heat transfer between the hot gas and the curtain of solids [74–80]. The key parameter that mainly controls the gas to solid heat transfer is the cascading rate of the flight [57]. It involves predicting the total particle surface area that is chiefly responsible for the heat and mass transfer. It can be regulated either by varying the Froude number of the drum or the flight length ratio. In general, industrial rotary drums operate at particular Froude numbers, in order to attain required throughput, filling degree and residence time. Therefore, the other possibility is to vary the flight length ratio in order to achieve the optimal cascading rates to give a better performance. No major predictions were carried out till now to address the surface area of the particles that is in contact with the hot gas.

Friedman and Marshall [28] developed an empirical relation for the volumetric heat transfer coefficient (U) and studied the influence of number of flights (n_F), rotational

speed, and the feed rate for different materials

$$UA_C = \frac{0.477}{D} \left(\frac{n_F - 1}{2} \right) G^{0.46} \quad , \quad (2.6)$$

where A_C is the overall contact area between gas and solid, and G is the gas flow rate. The factor with the number of flights in the equation signifies the number of curtains [81]. The volumetric coefficient was observed to be smaller when no flights were used, and a significant improvement had been observed while increasing the number of flights to two and four. No rapid change was observed when increasing the flight number to eight.

Saeman and Mitchell [57] developed a relation for the volumetric cascade rate which was studied against the heat transfer coefficient in order to estimate the performance of the dryer. The estimated heat transfer factor was observed to be decreased as the number of rotations increased. This is due to the fact that the air-material entrainment ratio decreased as the curtain density had increased. However, the variation of cascading rates due to the change in flight length ratios were not investigated. According to Porter [44], the concentration of the falling curtains in the gas stream depends on the ratio of cascade rate to the exposed surface of the series of curtains, however this ratio should not exceed 1.3 min^{-1} but it can be increased by experience. The shielding effect of the falling particles depends on the number of layers formed during the formation of the curtain. A boundary value for the number of particles falling from the flight was proposed by Hirose and Mujumdar [82] based on a single layer assumption. An empirical relation was determined to estimate the correction factor in order to evaluate the influence of the surrounding particles in the gas stream. It was found that this factor stands close to unity when the density of the falling particles was small and becomes smaller than 1 as the curtain concentration increases [83]. According to Blumberg and Schlünder [53], the performance of the dryer mainly depends on the contact area between the particles and the hot gas, which depends on the distribution of the material over the drum cross section. The effective transfer area was calculated based on the mean height of fall and the number of flights. However, this approach can lead to greater area of heat transfer than is possible.

In the recent studies, heat transfer analysis of the curtain falling into a duct while passing a stream of hot gas was studied by Wardjiman and Rhodes [84]. The authors developed a basic model for the single particle to evaluate the temperature variations of

the curtain. They assumed uniform gas flow across the curtain, however in practice a non uniform flow exists under these circumstances.

2.4 Summary

Among all these studies either the geometrical modeling or the studies of gas-solid contact area are independently existing. Many authors had focused on determining the holdup of single flight and its unloading characteristics. Using these studies the exposed area between gas-solid and the material distributed in the drum phases can be determined. However, very less contribution has been made to model the combination of the gas-solid contact area and determining each phase of the drum depending on the flight length ratio. Therefore the present study was focused on determining the optimal contact area for a rectangular type flights, by developing an independent model for the flight borne solids which is easy to extend to other flight types. Also no attempt has been made till date to extend the model of Schofield and Glikin [43] as it assumed a thin/single layer at the flight surface although there exists an active flowing layer. Therefore, another approach has been followed in this thesis to determine kinetic angle of repose by considering an active layer at the flight surface.

After having the detailed description about the rotary dryers and presenting the contributed literature on this subject, the next chapter presents the development of the geometrical model for different phases of the drum.

Chapter 3

Geometric model of transverse granular flow

3.1 Dimensionless parameters

The study of transverse motion of granular flow is significantly important in flighted rotating drums to determine the gas-solids contact area. The gas-solids contact area responsible for heat and mass transfer due to lifting flights is the total surface area of the particles flowing down with the curtains. In order to predict this parameter, it is necessary to estimate each phase of the material present in the drum, and the height of fall of the particles. Therefore, the dense phase of the flights and the height of fall can be determined from the geometrical approaches. Then from the mass balance and basic principles the other two phases can be modeled. In order to scale the drum from laboratory scale to industrial scale, the dimensionless approach has been followed for the modeling. The dimensionless parameters used in the study for the rotary drum with rectangular flights are described as follows.

Radial length of the flight (l_1) and tangential length (l_2) are the typical dimensions of the flight cross-section as shown in Fig. 3.1. The effective radial distance (r_H) of the flight is given by

$$\frac{r_H}{R} = 1 - \frac{l_1}{R} \quad , \quad (3.1)$$

where R is the radius of the drum. The characteristic angle made by the tangential length of the flight (l_2) to the effective radius of the flight (r_H) is

3.2 Model assumptions

- Free flowing and non-cohesive material
- The drum is assumed to be either design or over-loaded
- Uniform axial profile and no gas flow
- Free and vertical fall of the particles from flight tip (vertical drag and axial drag is neglected)
- All particles in the airborne phase behave independently
- Considered one axial section of the dryer

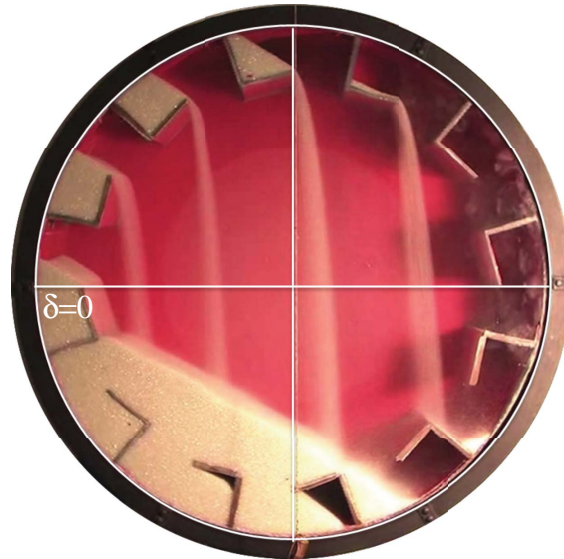


Figure 3.2: Experimental image of the drum with flight unloading at $\delta = 0$

3.3 Granular flow at the flight surface

3.3.1 Model of Schofield and Glikin

The quantity of material available in the flight can be determined as a function of the discharge angle if the free surface of the material flowing over the flight surface is known which is called as kinetic angle of repose. The free surface of the material in a rotary drum operated under rolling motion with no internal flights, forms an angle with the horizontal

known as dynamic angle of repose. Initially, the bed surface remains stable till the slope of the material is increased to the upper angle of repose or the maximum angle of stability [11, 15] and the avalanche occurs when the surface angle exceeds this angle. Further increasing the speed of the drum leads to rolling motion due to increase in the frequency of avalanches. Whereas in a flighted rotating drum, the material resting on the flight surface is being tilted due to the rotation of the drum, and the avalanches will start when the tilting surface of the material exceeds the maximum angle of stability [85–87]. At this point, the material organizes itself to reach the angle of repose by transmitting the extra material through avalanche and try to achieve the stable position. However, the change in the flight position imposes to exceed the maximum angle of stability again and further cascades a discrete amount of material. Therefore, the avalanche formation depends on the frequency of material surface reaching the upper angle of repose, rather than change in the flight position. Increasing the frequency leads to roll down the particles continuously over the surface of the static material in the flight which depends on the drum speed.

As the particles at the flight surface already at the maximum angle of stability, the flight starts cascading immediately while the tip of the flight is at horizontal position ($\delta = 0$) (see Fig. 3.2). This will continue till the material in the flight is being emptied at certain angle less than 180° . Since, it is unsure that when the avalanches will occur, a mean surface angle or kinetic angle of repose (γ) can be considered by assuming only a layer of particles flowing over flight surface and the surface to be flat. It is the material property that depends on the position of the flight (δ), Froude number (Fr), the geometrical properties, cohesion of the material, and also on the coefficient of dynamic friction ($\mu = \tan \Theta_A$). It was first calculated by Schofield and Glikin [43] by balancing the forces acting at the tip of the flight. The rolling particles on the surface of the flight are being influenced by the gravitational (F_G), centrifugal (F_C), and frictional forces (F_F). The Inertial force and the Coriolis forces were neglected. The block diagram of representing the forces acting at the tip of the flight is shown in Fig. 3.3.

$$\Sigma \mathbf{F} = \mathbf{F}_F + \mathbf{F}_N + \mathbf{F}_G + \mathbf{F}_C = \mathbf{0} \quad (3.6)$$

Normal force acting perpendicular to the bed surface is given by

$$F_N = F_G \cos \gamma - F_C \sin (\delta - \gamma) \quad . \quad (3.7)$$

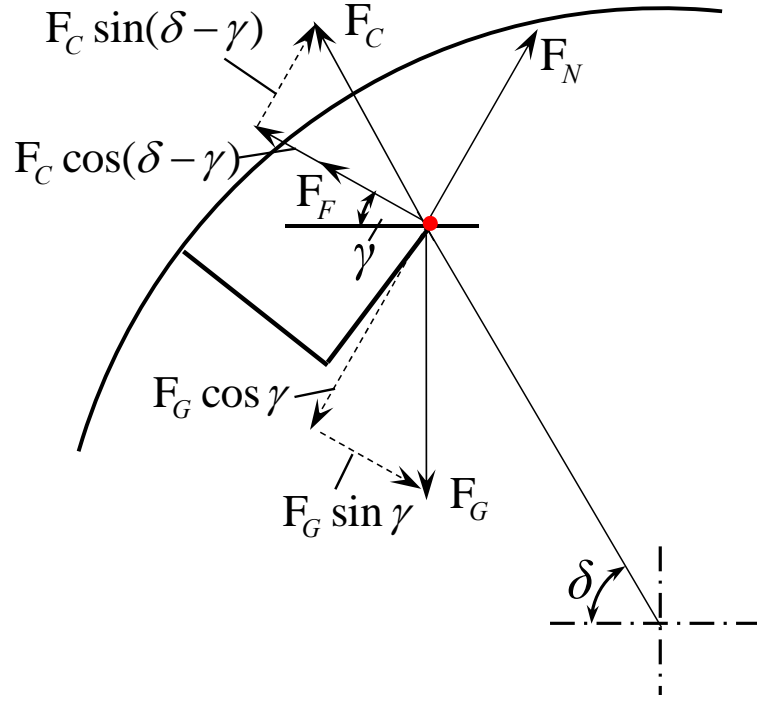


Figure 3.3: Force balance diagram of a particle during the time of falling from flight

The resultant force acting parallel to the bed surface is given by

$$F_F = F_G \sin \gamma - F_C \cos(\delta - \gamma) \quad . \quad (3.8)$$

Gravity acting on the particle of mass m_p is given by

$$F_G = m_p g \quad . \quad (3.9)$$

The particles that are ready to fall from the flight will undergo to the centrifugal force

$$F_C = m_p \omega^2 r_{HS} \quad , \quad (3.10)$$

where, r_{HS} is the radius formed by the tip of the flight. From Coulomb's law of friction, the resultant force is the coefficient of friction μ times the normal force

$$F_F = \mu F_N \quad . \quad (3.11)$$

Rearranging the above equations to get the kinetic angle of repose as a function of Froude

number, and tip angle (δ) to the center of the drum

$$\tan \gamma = \frac{\mu \cos \alpha + \text{Fr} \left(\frac{r_H}{R} \right) (\cos \delta - \mu \sin \delta)}{\cos \alpha - \text{Fr} \left(\frac{r_H}{R} \right) (\sin \delta + \mu \cos \delta)} \quad . \quad (3.12)$$

The kinetic angle (γ) approaches dynamic angle (Θ_A) as the Froude number approaches to 0, and $\frac{d\gamma}{d\delta} = 0.5$ while $\text{Fr}_m = \text{Fr} \left(\frac{r_{HS}}{R} \right) = 1$. One important limitation of this equation is, it is applicable only to the free flowing materials but not to highly cohesive solids, sticky and wet materials [37].

3.3.2 Extended model

The model of Schofield and Glikin [43] assumed only a layer of particles exists at the flight surface while determining the kinetic angle of repose by including centrifugal force and neglecting inertial force, although a flowing region exists similar to cascading layer in the drums without flights. Better prediction of this angle is truly important since this parameter is responsible to determine all phases of the drum. Therefore in the present study the model of Schofield and Glikin [43] has been extended by assuming a active layer at the flight (see Fig. 3.4(a)) and also incorporating the inertial term. The modified force balance diagram for this case is shown in Fig. 3.4(b)

$$F_F + F_I = F_G \sin \gamma - F_C \cos(\delta_c - \gamma) \quad , \quad (3.13)$$

where $\delta_c = \gamma - \theta \pm 90$, '-' is for $\delta < \gamma$ and '+' for $\delta > \gamma$, and $\tan \theta = x_E / (-R \cos \epsilon^*)$. The resultant force acting vertical to the bed surface is given by

$$F_N = F_G \cos \gamma - F_C \sin(\delta_c - \gamma) \quad . \quad (3.14)$$

The particles that are ready to fall from the layer over the flight surface will undergo to the centrifugal force

$$F_C = m_p \omega^2 r_{dHS} \quad , \quad (3.15)$$

where r_{dHS} is given by

$$r_{dHS} = \frac{x_E}{\sin \theta} \quad . \quad (3.16)$$

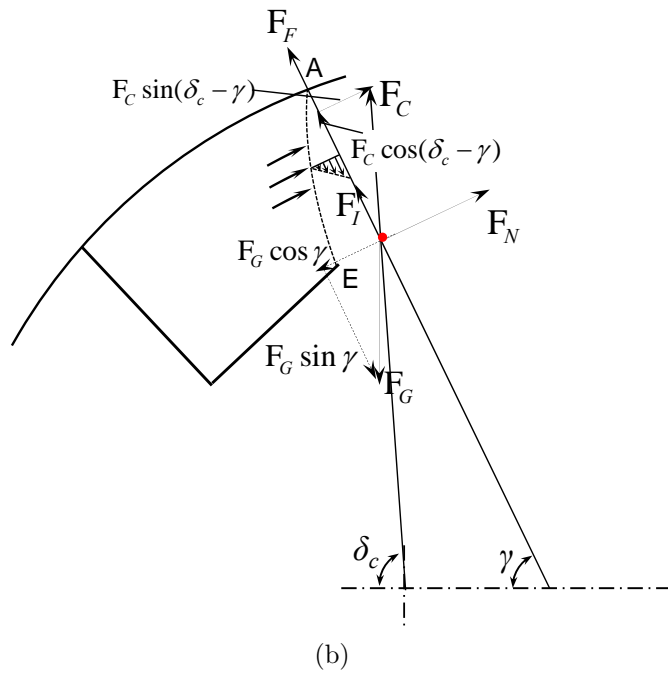
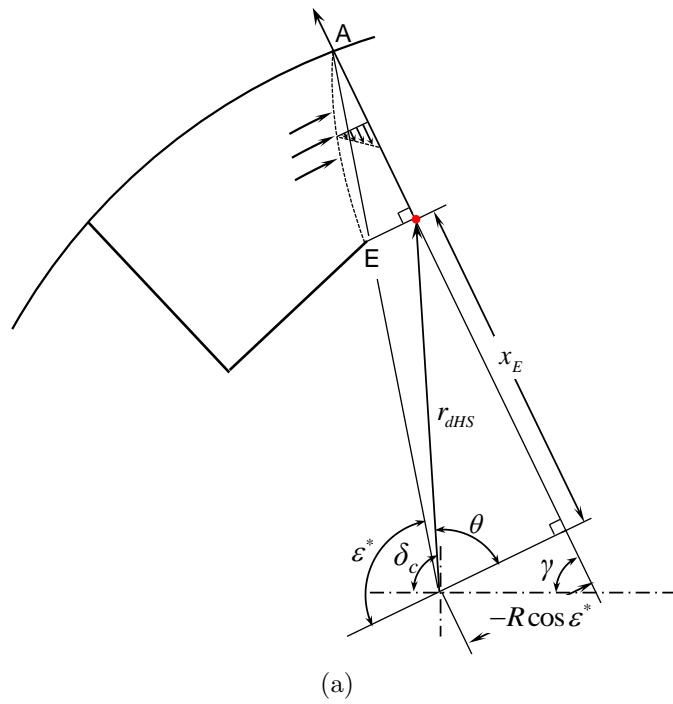


Figure 3.4: Representation of active layer at the flight surface a) Influencing variables
 b) Modified force balance diagram

The flow motion at the flight surface induces inertial force which can be expressed as [88]

$$F_I = m_p \bar{v}_x \frac{d\bar{v}_x}{dx} \quad , \quad (3.17)$$

\bar{v}_x is the average velocity of the particles in the active layer. After simplifications of the above equations and rearranging, the final form of the kinetic angle is given by

$$\tan \gamma = \frac{\mu + \text{Fr} \left(\frac{r_{dHS}}{R} \right) (\cos \delta_c - \mu \sin \delta_c) + \text{Fr} \frac{\bar{v}_x^*}{\cos \gamma} \frac{d\bar{v}_x^*}{dx^*}}{1 - \text{Fr} \left(\frac{r_{dHS}}{R} \right) (\sin \delta_c + \mu \cos \delta_c)} \quad . \quad (3.18)$$

here $\bar{v}_x^* = \frac{\bar{v}_x}{R\omega}$ and $\frac{d\bar{v}_x^*}{dx^*} = \frac{\bar{v}_x^* |A - \bar{v}_x^*|_E}{x_A^* - x_E^*}$. From the above equation, at $\text{Fr}=0$ i.e. when the drum is at rest, $\gamma = \tan^{-1}(\mu)$. The detailed description of the velocity gradient term has been presented in Chapter 4.

3.4 Flight holdup

The discharge characteristics of a flight (i) depends on the geometrical lengths of the flight, kinetic angle of repose, and the discharge point of the flight (δ) at a given Froude number. The bulk mass occupied by the flight $m_{F,i}(\delta)$ can be calculated from the bulk density (ρ_b), and the volume occupied by the material in the flight $V_{F,i}(\delta)$ at a given tip position as

$$m_{F,i}(\delta) = \rho_b V_{F,i}(\delta) = \rho_b \cdot L \cdot A_{F,i} \quad , \quad (3.19)$$

where, $A_{F,i}$ is the cross sectional area of material occupied by the flight, and L is the length of the drum. Divide above equation with the total volume of the cylinder in order to scale the drum at higher size ratios. Most of the earlier works include empirical models and non dimensional analysis of the rotary dryers. The scaling methodologies published in this area are very limited including drum without flights [89]

$$\frac{m_{F,i}(\delta)}{\rho_b \pi R^2 L} = \frac{A_{F,i}(\delta)}{\pi R^2} = f_{F,i}(\delta) \quad . \quad (3.20)$$

The filling degree of the flight $f_{F,i}(\delta)$, is the volume of the material occupied by the flight per unit volume of the cylinder. According to Glikin [46], it is difficult to develop a single relation for the flight holdup during the period of discharge, hence each region is

considered individually in order to represent it as a continuous function of the discharge point.

Three different regions (R-I, R-II, and R-III) can be identified along the discharge of the rectangular flight such as shown in Fig. 3.3. In the region-I, the material will have the influence of drum wall and mostly supported by the radial length of the flight. The transition to the region-II occurs when the flight tip exceeds the kinetic angle γ . Here, the tangential length of the flight influences the material discharge, whereas in region-III the material has been influenced by the flight surface alone. Since the material expose to different transitions during the discharge, it is difficult to derive a single expression to describe the complete unloading profile of the flight. Therefore, each transition can be represented by an independent equation for the holdup of the flight [88, 90], which is clearly described in the following.

Region I ($\delta \leq \gamma$): The formation of the regions is categorized based on the discharge angle. The first region can be observed between the points, where the flight comes out of the bed and the position of the flight tip is lower than the kinetic angle of repose. Area of the material occupied ($A_{F,i}$) by the flight in this region can be found by the following expression (from Fig. 3.5(a))

$$A_{F,i} = A_W - A_{11} - A_{12} \quad . \quad (3.21)$$

The individual areas of this expression are given by

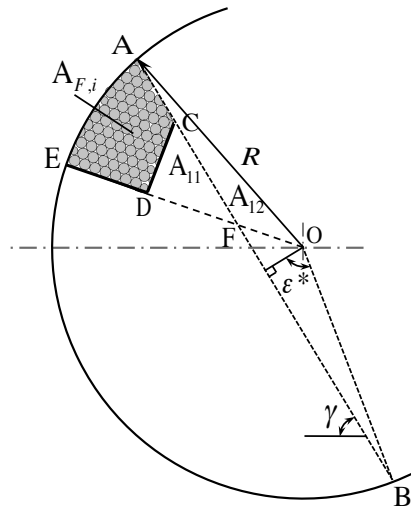
$$\begin{aligned} A_W(\wedge OAE) &= (\gamma + \varepsilon^* - \varphi) \cdot \frac{\pi R^2}{360^\circ} \quad , \\ A_{11}(\triangle FDC) &= \frac{1}{2} \cdot FD \cdot l_2 \quad , \\ A_{12}(\triangle OAF) &= \frac{1}{2} \cdot h \cdot R \quad , \end{aligned} \quad (3.22)$$

ε^* is the auxiliary filling angle formed by the surface of the material in the flight, and can be expressed as

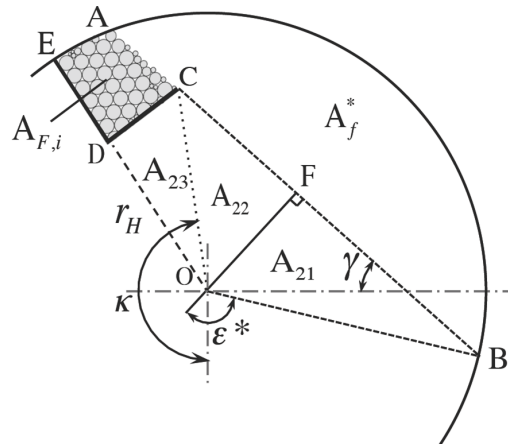
$$\varepsilon^* = \arccos \left[\left(\frac{r_H}{R} \right) \cdot \frac{\cos(\kappa - \gamma)}{\cos \alpha} \right] \quad . \quad (3.23)$$

The length FD can be found from

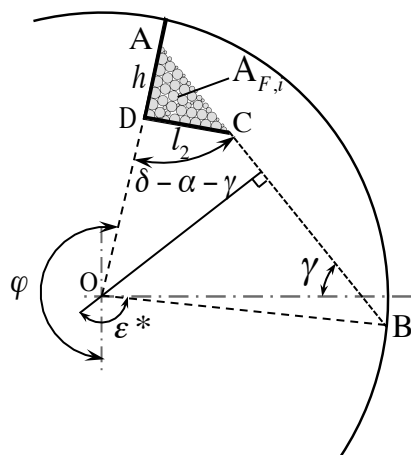
$$FD = l_2 \cdot \tan(\varphi - \gamma) \quad , \quad (3.24)$$



(a) R-I ($\delta \leq \gamma$)



(b) R-II ($\gamma < \delta \leq (\gamma + \alpha + \beta)$)



(c) R-III ($(\gamma + \alpha + \beta) < \delta \leq \delta_L$)

Figure 3.5: Cross sectional representation of the three regions during flight discharge process

From Fig. 3.6 h is given by

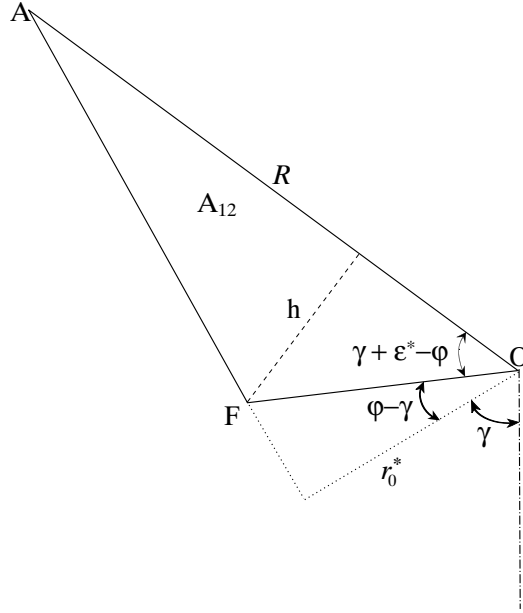


Figure 3.6: Calculation of area A_{12}

$$\begin{aligned}
 h &= OF \cdot \sin(\gamma + \varepsilon^* - \varphi) \quad , \\
 OF &= \frac{r_0^*}{\cos(\varphi - \gamma)} \quad , \\
 r_0^* &= r_{HS} \cdot \cos(\kappa - \gamma) = R \cos \varepsilon^* \quad ,
 \end{aligned} \tag{3.25}$$

κ, φ are the auxiliary coordinates represented as $\kappa = 90^\circ + \delta$, and $\varphi = \kappa - \alpha$. Finally, the filling degree of the material in this region can be calculated by substituting the equations Eq. (3.21) to Eq. (3.25) in Eq. (3.20)

$$\begin{aligned}
 f_{F,i}(\delta) &= \frac{1}{2\pi} \left[\frac{\pi(\gamma + \varepsilon^* - \varphi)}{180^\circ} - \left(\frac{r_H}{R} \right) \cdot \frac{\cos(\kappa - \gamma)}{\cos \alpha} \right. \\
 &\quad \left. \frac{\sin(\gamma + \varepsilon^* - \varphi)}{\cos(\varphi - \gamma)} - \left(\frac{l_2}{R} \right)^2 \tan(\varphi - \gamma) \right] \quad .
 \end{aligned} \tag{3.26}$$

Region II ($\gamma < \delta \leq (\gamma + \alpha + \beta)$): The transition into the second region occurs when the position of the flight exceeds the value of the kinetic angle. The material occupied by the flight in this region is less than the volume of the flight's ideal capacity, unlike in the first phase of unloading where the flight holds more than its capacity. The cross sectional area occupied by the material ($A_{F,i}$) during this phase (see Fig. 3.5(b)) can be

calculated from the following equation

$$A_T = \sum_{k=1}^3 A_{2k} + A_f^* + A_{F,i} \quad . \quad (3.27)$$

A_T is the total area of the sector ($\wedge OEB$)

$$A_T = \frac{R^2}{2} \cdot \frac{\pi}{180^\circ} \cdot \sphericalangle EOB \quad . \quad (3.28)$$

The angle subtended by the arc at the center can be given by the following relation

$$\sphericalangle EOB = 2 \cdot \phi^* + \Delta\phi \quad ,$$

where, ϕ^* is the angle subtended at center $\sphericalangle FOB$ given by $\phi^* = 180^\circ - \epsilon^*$, and $\Delta\phi$ from Fig. 3.7 becomes $(90^\circ + \gamma + \alpha - \phi^* - \delta)$. A_f^* is the area of the circular segment (\widehat{BA}) in

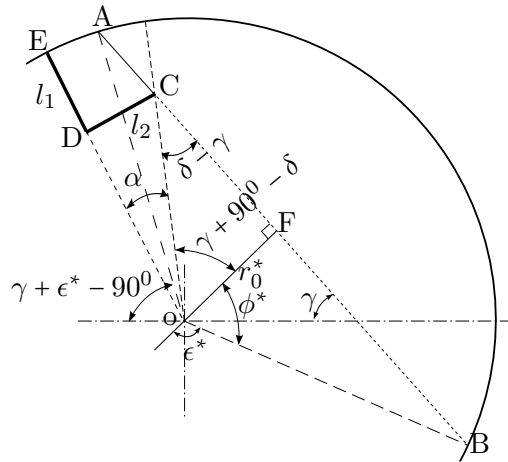


Figure 3.7: Calculation of area A_{21} , A_{22} , and A_{23}

Fig. 3.5(b), which can be calculated from

$$A_f^* = R^2 \cdot \left(\frac{\pi\phi^*}{180^\circ} - \sin\phi^* \cdot \cos\phi^* \right) \quad . \quad (3.29)$$

The subscript '2' in Eq. (3.27) indicates Region II and 'i' stands for the areas of triangles depicted in the Fig. 3.5(b) and the respective angles to calculate these areas are shown in Fig. 3.7. A_{21} from $\triangle OBF$ can be given by

$$A_{21} = \frac{R^2}{2} \cdot \cos\phi^* \cdot \sin\phi^* \quad . \quad (3.30)$$

A_{22} from $\triangle OFC$

$$A_{22} = \frac{1}{2} \cdot r_0^* \cdot FC \quad , \quad (3.31)$$

where, $FC = \frac{r_0^*}{\tan(\delta - \gamma)}$, and $r_0^* = R \cos \phi^*$. From $\triangle ODC$, area A_{23} can be given by

$$A_{23} = \left(\frac{R^2}{2} \right) \cdot \left(\frac{l_2}{R} \right) \cdot \left(\frac{r_H}{R} \right) \quad . \quad (3.32)$$

By substituting the above equations in Eq. (3.27), results the cross sectional area occupied by the material in region-II. Using this area, the filling degree of the flight valid in this region can be calculated as

$$f_{F,i}(\delta) = \frac{1}{2\pi} \left[\frac{\pi(\gamma + \varepsilon^* - \varphi)}{180^\circ} - \sin \varepsilon^* \cos \varepsilon^* - \frac{\cos^2 \varepsilon^*}{\tan(\delta - \gamma)} - \left(\frac{r_H}{R} \right) \cdot \left(\frac{l_2}{R} \right) \right]. \quad (3.33)$$

Region III ($(\gamma + \alpha + \beta) < \delta \leq \delta_L$): Along the way, the material crosses the two regions discussed above and enters into the third region, where the solid particles detach from the drum wall and touch the flight surface alone as shown in Fig. 3.5(c). Sliding behavior can be observed when the last layer of the solids are about to discharge, and the flight will be emptied at final discharge angle ($\delta_L = 90^\circ + \alpha + \gamma_L$). The cross sectional area occupied by the material in this region can be found from $\triangle ADC$

$$A_{F,i} = \frac{1}{2} \cdot h \cdot l_2 \quad , \quad (3.34)$$

where $h = \frac{l_2}{\tan(\delta - \alpha - \gamma)}$.

The filling degree of the flight in the final region is given by the following equation

$$f_{F,i}(\delta) = \frac{1}{2\pi} \cdot \left(\frac{l_2}{R} \right)^2 \frac{1}{\tan(\delta - \gamma - \alpha)} \quad . \quad (3.35)$$

The total filling degree or the total dense phase of the active flights can be predicted based on the average approach, as a function of the individual flight holdup and the total number of active flights

$$f_{F,\Sigma} = n_{F,a} \cdot \bar{f}_{F,i}(\delta) \quad , \quad (3.36)$$

where $n_{F,a}$ is the number of active flights depending on the theoretical number of flights (n_F) given by

$$n_{F,a} = \frac{\delta_L}{360^\circ} \cdot n_F \quad , \quad (3.37)$$

and $\bar{f}_{F,i}(\delta)$ is the mean filling degree of the flights

$$\bar{f}_{F,i}(\delta) = \frac{1}{\delta_L} \cdot \int_0^{\delta_L} f_{F,i}(\delta) d\delta \quad . \quad (3.38)$$

here, δ_L is the final discharge angle.

3.5 Cascading rate of the flight

The material cascades out of the flight due to the formation of continuous avalanches at the surface. The flow cannot be developed fully, but breaks at the tip of the flight by cascading the material into the free space where it encounters the hot gaseous stream. The unloading of the flight, thus measures the amount of material to be in contact with the gaseous phase which becomes an important parameter to study. The material in the flight reduces by certain amount per unit time which primarily depends on its material properties such as kinetic angle, bulk density of the material (ρ_b), and rotational speed of the drum. The rate of change of the flight holdup is given by the following equation

$$\dot{m}_{F,i} = -\frac{dm_{F,i}(\delta)}{dt} \quad (3.39)$$

$$= \rho_b \cdot \pi R^2 L \cdot \left(-\frac{df_{F,i}(\delta)}{dt} \right) \quad . \quad (3.40)$$

The negative sign in the equation indicates the decrease in the holdup of the flight. The rate of change of filling fraction is written as

$$\left(-\frac{df_{F,i}(\delta)}{dt} \right) = \left(-\frac{df_{F,i}(\delta)}{d\delta} \right) \cdot \frac{d\delta}{dt} \quad . \quad (3.41)$$

Since $\frac{d\delta}{dt} = \omega$, the discharge rate of the flight can be estimated from the following equation

$$\frac{\dot{m}_{F,i}}{\rho_b \cdot \omega \cdot \pi R^2 L} = \left(-\frac{df_{F,i}(\delta)}{d\delta} \right) \quad . \quad (3.42)$$

Differentiating the eqs. (3.26), (3.33), and (3.35) for all the three regions

Region-I

$$\begin{aligned} \frac{df_{F,i}}{d\delta} = & \frac{1}{2\pi} \cdot \left\{ \frac{d\gamma}{d\delta} + \frac{d\varepsilon^*}{d\delta} - 1 - \left(1 - \frac{d\gamma}{d\delta}\right) \cdot \right. \\ & \left[\left(\frac{l_2}{R}\right)^2 \cdot (1 + \tan^2(\varphi - \gamma)) - \left(\frac{r_H}{R} \cdot \frac{\sin(\kappa - \gamma) \cdot \sin(\gamma + \varepsilon^* - \varphi)}{\cos \alpha \cdot \cos(\varphi - \gamma)}\right) \right] - \\ & \left(\frac{r_H}{R}\right) \cdot \frac{\cos(\kappa - \gamma)}{\cos \alpha \cdot \cos(\varphi - \gamma)} \quad (3.43) \\ & \left. \left[\left(\frac{d\gamma}{d\delta} + \frac{d\varepsilon^*}{d\delta} - 1\right) \cos(\gamma + \varepsilon^* - \varphi) + \left(1 - \frac{d\gamma}{d\delta}\right) \tan(\varphi - \gamma) \sin(\gamma + \varepsilon^* - \varphi) \right] \right\} . \end{aligned}$$

Region-II

$$\frac{df_{F,i}}{d\delta} = \frac{1}{2\pi} \cdot \left\{ 2 \sin \varepsilon^* \cdot \frac{d\varepsilon^*}{d\delta} \left[\sin \varepsilon^* + \frac{\cos \varepsilon^*}{\tan(\delta - \gamma)} \right] + \left(1 - \frac{d\gamma}{d\delta}\right) \cdot \left[\frac{\cos^2 \varepsilon^*}{\sin^2(\delta - \gamma)} - 1 \right] \right\} . \quad (3.44)$$

Region-III

$$\frac{df_{F,i}}{d\delta} = \frac{1}{2\pi} \cdot \left(\frac{l_2}{R}\right)^2 \cdot \left(\frac{d\gamma}{d\delta} - 1\right) \cdot \frac{1}{\sin^2(\delta - \alpha - \gamma)} . \quad (3.45)$$

The unknown quantities of the eqs. (3.43), (3.44), and (3.45) are subsequently calculated. The first derivative of the kinetic angle is given from the following equation

$$\frac{d\gamma}{d\delta} = \frac{\text{Fr}^2 \left(\frac{r_H}{R}\right)^2 \cdot [(\sin \delta + \mu \cos \delta)^2 + (\cos \delta - \mu \sin \delta)^2] - \text{Fr} \left(\frac{r_H}{R}\right) (1 + \mu^2) \cos \alpha \cdot \sin \delta}{\left[\mu \cos \alpha + \text{Fr} \left(\frac{r_H}{R}\right) (\cos \delta - \mu \sin \delta) \right]^2 + \left[\cos \alpha - \text{Fr} \left(\frac{r_H}{R}\right) (\sin \delta + \mu \cos \delta) \right]^2} . \quad (3.46)$$

The first derivative of the auxiliary filling angle is given by

$$\frac{d\varepsilon^*}{d\delta} = \frac{\left(\frac{r_H}{R}\right) \sin(\kappa - \gamma) \cdot \left(1 - \frac{d\gamma}{d\delta}\right)}{\sqrt{\cos^2 \alpha - \left(\frac{r_H}{R}\right)^2 \cos^2(\kappa - \gamma)}} . \quad (3.47)$$

3.6 Model of the final flight discharge

3.6.1 Mellmann's Final discharge angle model

The angle at which the material completely discharges from the flight is the Final discharge angle. The feeding of the flight starts in the lower half of the drum. However, the discharge of the solids happens at tip angles of above 0° under design loaded conditions, it continue until the flight is completely emptied at certain angle less than 180° . At the point of final discharge, the amount of material in the flight is relatively small and is subjected to only the friction between the particles and the wall, and also collisional stresses between the particles. The particles roll/slide over the wall surface under such conditions. Principally the flight empties at a point given by the following equation [37, 46, 53, 54]

$$\delta_L = 90^\circ + \alpha + \gamma_L \quad . \quad (3.48)$$

The kinetic angle at empty point (γ_L) can be calculated by applying the above equation in Eq. (3.12), which leads to the following equation. The equation can be solved by iteration procedure, to get the final discharge angle [88]

$$\tan \gamma_L = \frac{\mu \cdot \cos \alpha + \text{Fr} \cdot \left(\frac{r_H}{R}\right) \cdot [\cos(90^\circ + \alpha + \gamma_L) - \mu \cdot \sin(90^\circ + \alpha + \gamma_L)]}{\cos \alpha - \text{Fr} \cdot \left(\frac{r_H}{R}\right) \cdot [\sin(90^\circ + \alpha + \gamma_L) + \mu \cdot \cos(90^\circ + \alpha + \gamma_L)]} \quad . \quad (3.49)$$

Final discharge angle is one of the major influencing parameter on the quality of the product. It depends on various profiles of the flights as shown in Fig. 1.7, and special profiles like EAD and EHD [50] and the dimensions of the flights. The more is this angle, more is the contact time of the hot gas with the material. In general, this angle will be higher at higher tangential lengths of the flight at a given rotational speed of the drum. However, as we increase this length the number of flights to be occupied will become smaller, in turn there is a possibility to decrease the exposed area for heat and mass transfer which tells that the necessity to develop an optimal solution for such behavior.

3.6.2 Extended Final discharge angle model

During the period of final discharge, the bed height at the flight decreases as the holdup of the flight tends to zero. As a result the material flowing from the static bed to the active

layer decreases, which then leads to small cascading rates. The granular flow behavior at this stage can be expected different as compared to the earlier stages, since the layer of solids flowing in this region is a diluted phase. Hence the motion of solids changes from bulk motion to sliding or slipping at the flight sheet. As the solids in the flight become diluted, the Froude number influences on the final discharge angle. Therefore, to determine this phenomenon only one layer of particles is considered in order to evaluate the position of last particle leaving from the flight. However the transition point to this phase is still unpredictable, but it can be presumed that this transition occurs while the thickness of the flowing layer at the flight tends to close to the total height of the bed at the flight. Previous models does not accounted the diluted phase by assuming that the flight empties when the surface of the flight sheet is parallel to the bed surface.

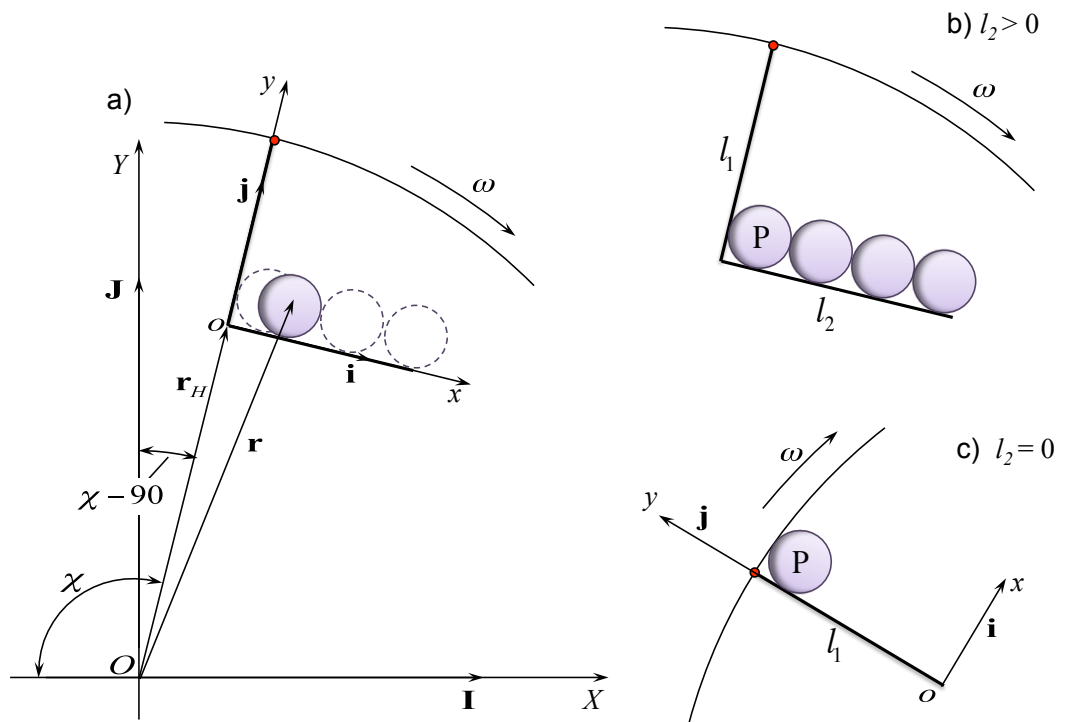


Figure 3.8: Schematic of rotating frame of flight

3.6.2.1 Assumptions

- Single layer of particles is assumed
- Initial condition for the system is considered from the previous model

- No rolling friction between the particle and the flight surface is considered

3.6.2.2 Rotating flight frame of reference

Consider a layer of particles on the flight surface that are ready to slide downwards from the flight tip as shown in Fig. 3.8. Therefore, Final discharge angle of the flight can be determined by predicting the position of the last particle (P) that leaves from the flight surface. Consider oxy be a rotating frame of flight which is moving about a fixed frame OXY . Here 'o' is the intersection of the radial length (l_1) and tangential length (l_2) of the flight and 'O' is fixed at the center of the drum. Let \mathbf{I} and \mathbf{J} are the unit vectors along XY axis, and \mathbf{i} and \mathbf{j} are the unit vectors of xy axis. \mathbf{r} be the position vector of the particle (P) and χ representing the position of the flight.

The unit vectors of the rotating frame (\mathbf{i} , \mathbf{j}) can be expressed in terms of fixed frame of reference (\mathbf{I} , \mathbf{J}) from the triangle law of addition of vectors as

$$\begin{aligned}\mathbf{i} &= \sin \chi \cdot \mathbf{I} + \cos \chi \cdot \mathbf{J} \quad , \\ \mathbf{j} &= -\cos \chi \cdot \mathbf{I} + \sin \chi \cdot \mathbf{J} \quad .\end{aligned}\tag{3.50}$$

It is to be noted that the vectors \mathbf{i} , \mathbf{j} are time dependent, therefore

$$\begin{aligned}\dot{\mathbf{i}} &= \frac{d\mathbf{i}}{dt} = -\mathbf{j}\dot{\chi} \quad , \\ \dot{\mathbf{j}} &= \frac{d\mathbf{j}}{dt} = \mathbf{i}\dot{\chi} \quad .\end{aligned}\tag{3.51}$$

The position vector of the particle can be expressed as

$$\mathbf{r} = X\mathbf{I} + Y\mathbf{J} \quad ,\tag{3.52}$$

where X, Y are the coordinates of the particle with respect to fixed frame. Similarly, the position vector can also be expressed as a function of the rotating frame

$$\mathbf{r} = \mathbf{r}_H + (x\mathbf{i} + y\mathbf{j}) \quad ,\tag{3.53}$$

where \mathbf{r}_H is the position of the origin (o)

$$\begin{aligned}\mathbf{r}_H &= r_H (-\cos \chi \mathbf{I} + \sin \chi \mathbf{J}) \quad , \\ &= r_H \mathbf{j} \quad ,\end{aligned}\tag{3.54}$$

substituting the above relation in Eq. (3.53)

$$\mathbf{r} = x \mathbf{i} + (y + r_H) \mathbf{j} \quad , \quad (3.55)$$

Hence, from this relation the velocity of the particle to an observer in the fixed frame of reference can be obtained by differentiating Eq. (3.52) with time

$$\frac{d\mathbf{r}}{dt} = \dot{X} \mathbf{I} + \dot{Y} \mathbf{J} \quad , \quad (3.56)$$

However to an observer in the rotating frame, the velocity of the particle can be written as

$$\frac{\Delta \mathbf{r}}{\Delta t} = \dot{x} \mathbf{i} + \dot{y} \mathbf{j} \quad , \quad (3.57)$$

here, $\Delta/\Delta t$ is represented as differential term for the rotating frame of flight [91]. Further a relation can be developed for both the frames by differentiating Eq. (3.55)

$$\frac{d\mathbf{r}}{dt} = (\dot{x} \mathbf{i} + \dot{y} \mathbf{j}) + (x \dot{\mathbf{i}} + (y + r_H) \dot{\mathbf{j}}) \quad . \quad (3.58)$$

Substituting Eqs. (3.51), (3.55) and (3.57) and $\dot{\chi} = \omega$ yields the following relation

$$\begin{aligned} \frac{d\mathbf{r}}{dt} &= \frac{\Delta \mathbf{r}}{\Delta t} + ((y + r_H) \omega \mathbf{i} - x \omega \mathbf{j}) \quad , \\ &= \left(\frac{\Delta \mathbf{r}}{\Delta t} + \boldsymbol{\omega} \times \mathbf{r} \right) \quad , \end{aligned} \quad (3.59)$$

where $\boldsymbol{\omega} = \omega \mathbf{k}$, \mathbf{k} is the unit vector orthogonal to \mathbf{i} , \mathbf{j} .

$$\frac{d\mathbf{r}}{dt} = \left(\frac{\Delta}{\Delta t} + \boldsymbol{\omega} \times \right) \mathbf{r} \quad . \quad (3.60)$$

Finally the relation between the fixed frame of reference and rotating frame can be written as

$$\frac{d}{dt} = \left(\frac{\Delta}{\Delta t} + \boldsymbol{\omega} \times \right) \quad . \quad (3.61)$$

According to Newton's second law of motion, the sum of the forces acting on a body is

$$\sum \mathbf{F} = m_p \ddot{\mathbf{r}} \quad . \quad (3.62)$$

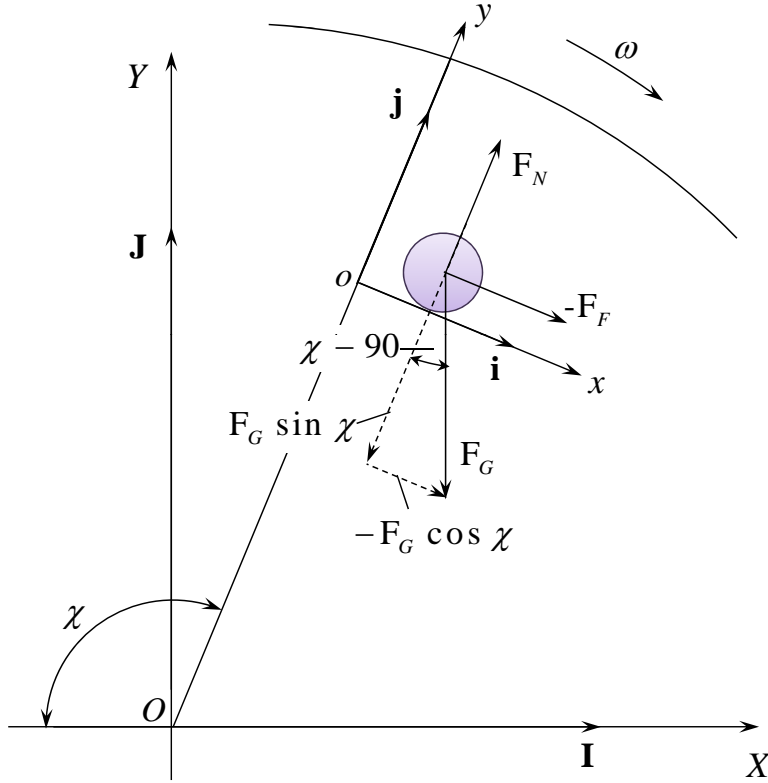


Figure 3.9: Force balance diagram of the particle sliding over the rotating flight

Using Eqs. (3.60) and (3.61) in the above relation

$$\begin{aligned}
 \sum \mathbf{F} &= m_p \cdot \left(\frac{\Delta}{\Delta t} + \boldsymbol{\omega} \times \right) \left(\frac{\Delta}{\Delta t} + \boldsymbol{\omega} \times \right) \mathbf{r} \quad , \\
 &= m_p \cdot \left(\frac{\Delta}{\Delta t} + \boldsymbol{\omega} \times \right) \left(\frac{\Delta \mathbf{r}}{\Delta t} + \boldsymbol{\omega} \times \mathbf{r} \right) \quad , \\
 &= m_p \cdot \left(\frac{\Delta^2 \mathbf{r}}{\Delta t^2} - \left(\boldsymbol{\omega} \times \frac{\Delta \mathbf{r}}{\Delta t} \right) - \frac{\Delta}{\Delta t} (\boldsymbol{\omega} \times \mathbf{r}) + (\boldsymbol{\omega} \times (\boldsymbol{\omega} \times \mathbf{r})) \right) \quad , \\
 &= m_p \cdot \left(\frac{\Delta^2 \mathbf{r}}{\Delta t^2} - \left(\boldsymbol{\omega} \times \frac{\Delta \mathbf{r}}{\Delta t} \right) - \left(\boldsymbol{\omega} \times \frac{\Delta \mathbf{r}}{\Delta t} \right) - \left(\frac{\Delta \boldsymbol{\omega}}{\Delta t} \times \mathbf{r} \right) + (\boldsymbol{\omega} \times (\boldsymbol{\omega} \times \mathbf{r})) \right) \quad .
 \end{aligned} \tag{3.63}$$

Expanding the fourth term in the equation

$$\begin{aligned}
 \boldsymbol{\omega} \times (\boldsymbol{\omega} \times \mathbf{r}) &= (\boldsymbol{\omega} \cdot \mathbf{r}) \boldsymbol{\omega} - (\boldsymbol{\omega} \cdot \boldsymbol{\omega}) \mathbf{r} \\
 &= -\omega^2 \mathbf{r} \quad (\because \boldsymbol{\omega} \cdot \mathbf{r} = 0).
 \end{aligned}$$

By substituting the above equation and $\frac{\Delta \boldsymbol{\omega}}{\Delta t} = \dot{\boldsymbol{\omega}}$ in Eq. (3.63), the final form of the force

balance equation becomes

$$\sum \mathbf{F} = m_p \cdot \left(\frac{\Delta^2 \mathbf{r}}{\Delta t^2} - 2 \left(\boldsymbol{\omega} \times \frac{\Delta \mathbf{r}}{\Delta t} \right) - (\dot{\boldsymbol{\omega}} \times \mathbf{r}) - \omega^2 \mathbf{r} \right) \quad . \quad (3.64)$$

The second and fourth terms in the right hand side of the equation represent apparent forces, where $-2m_p (\boldsymbol{\omega} \times \Delta \mathbf{r}/\Delta t)$ is called Coriolis force and $-m_p \omega^2 \mathbf{r}$ represent Centrifugal force [91, 92]. To an observer at the moving frame the Coriolis force act perpendicularly to the direction of the moving object. Whereas the third term in the equation becomes $(\dot{\boldsymbol{\omega}} = \mathbf{0})$ since, the rotating frame of flight is moving at a constant angular velocity. Therefore finally the force balance equation can be written as

$$\sum \mathbf{F} = m_p \cdot \left(\frac{\Delta^2 \mathbf{r}}{\Delta t^2} - 2 \left(\boldsymbol{\omega} \times \frac{\Delta \mathbf{r}}{\Delta t} \right) - \omega^2 \mathbf{r} \right) \quad . \quad (3.65)$$

Now apply the equations to the problem of particle sliding over the rotating flight. Let x_p, y_p represent the position of the particle relative to moving frame of flight. Assuming that the particle always contacts the wall surface, $y_p = r_p$, where r_p is the radius of the particle. The terms in Eq. (3.55) has been reduced to

$$\begin{aligned} \mathbf{r} &= x_p \mathbf{i} + (y_p + r_H) \mathbf{j} \quad , \\ \frac{\Delta \mathbf{r}}{\Delta t} &= \dot{x}_p \mathbf{i} + \dot{y}_p \mathbf{j} = \dot{x}_p \mathbf{i} \quad , \\ \frac{\Delta^2 \mathbf{r}}{\Delta t^2} &= \ddot{x}_p \mathbf{i} \quad . \end{aligned} \quad (3.66)$$

The sum of forces acting on the particle sliding over the flat surface inclined to horizontal can be represented as,

$$\sum \mathbf{F} = \sum F_x \mathbf{i} + \sum F_y \mathbf{j} \quad . \quad (3.67)$$

Therefore, by resolving the component of forces from Fig. 3.9, acting on the particle while sliding over the flight surface is given by

$$\begin{aligned} \sum F_x &= -(F_G \cos \chi + F_F) \quad , \\ \sum F_y &= (F_N - F_G \sin \chi) \quad , \end{aligned} \quad (3.68)$$

where, F_G is the gravitational force acting on the particle given by

$$F_G = m_p g \quad , \quad (3.69)$$

F_F and F_N are the frictional and normal forces respectively acting on the particle. From the coulomb's law the frictional and normal forces can be related as

$$F_F = \mu_w F_N \quad , \quad (3.70)$$

where μ_w is the wall friction coefficient ($\mu_w = \tan \Theta_w$). Simplifying Eqs. (3.65) to (3.67)

$$\sum F_x \mathbf{i} + \sum F_y \mathbf{j} = m (\ddot{x}_p \mathbf{i} - 2\omega \dot{x}_p (\mathbf{k} \times \mathbf{i}) - \omega^2 (x_p \mathbf{i} + (r_p + r_H) \mathbf{j})) \quad . \quad (3.71)$$

After resolving the above equation into the respective components

$$\begin{aligned} \sum F_x &= m_p (\ddot{x}_p - \omega^2 x_p) \quad , \\ \sum F_y &= m_p (-2\omega \dot{x}_p - \omega^2 (r_p + r_H)) \quad . \end{aligned} \quad (3.72)$$

Substituting Eq. (3.68) in Eq. (3.72) and rearranging the terms

$$\begin{aligned} F_F &= -m \ddot{x}_p + m \omega^2 x_p - F_G \cos \chi \\ F_N &= F_G \sin \chi - 2m \omega \dot{x}_p - m \omega^2 (r_p + r_H) \end{aligned} \quad (3.73)$$

Using Eqs. (3.69) and (3.73) in Eq. (3.70) and after simplification

$$\ddot{x}_p - 2\mu_w \omega \dot{x}_p - \omega^2 x_p = \mu_w \omega^2 (r_p + r_H) - \mu_w g \sin \chi - g \cos \chi \quad (3.74)$$

where $\ddot{x}_p = \frac{\Delta^2 x_p}{\Delta t^2}$, $\dot{x}_p = \frac{\Delta x_p}{\Delta t}$. Since $\Delta t = \Delta \chi / \omega$, substituting in Eq. (3.74) we get

$$\omega^2 \frac{\Delta^2 x_p}{\Delta \chi^2} - 2\mu_w \omega^2 \frac{\Delta x_p}{\Delta \chi} - \omega^2 x_p = \mu_w \omega^2 (r_p + r_H) - \mu_w g \sin \chi - g \cos \chi \quad . \quad (3.75)$$

Divide the above equation with $(\omega^2 R)$ to convert into dimension less form and finally

$$\boxed{\frac{\Delta^2 x_p^*}{\Delta \chi^2} - 2\mu_w \frac{\Delta x_p^*}{\Delta \chi} - x_p^* = \mu_w \left(\frac{r_p + r_H}{R} \right) - \frac{1}{\text{Fr}} (\mu_w \sin \chi + \cos \chi)} \quad . \quad (3.76)$$

where $x_p^* = \frac{x_p}{R}$, $\text{Fr} = \frac{\omega^2 R}{g}$.

Equation (3.76) is valid when $l_2 > 0$, however for the case of radial flights when ($l_2 = 0$) similar equation can be developed while in this case x_p is constant but y_p varies with

time. Hence Eq. (3.66) is transformed to

$$\begin{aligned} \mathbf{r} &= x_p \mathbf{i} + (y_p + r_H) \mathbf{j} \quad , \\ \frac{\Delta \mathbf{r}}{\Delta t} &= \dot{x}_p \mathbf{i} + \dot{y}_p \mathbf{j} = \dot{y}_p \mathbf{j} \quad , \\ \frac{\Delta^2 \mathbf{r}}{\Delta t^2} &= \ddot{y}_p \mathbf{j} \quad . \end{aligned} \quad (3.77)$$

The force components had been modified to

$$\begin{aligned} \sum F_x &= F_N - F_G \cos \chi \quad , \\ \sum F_y &= F_F - F_G \sin \chi \quad , \end{aligned} \quad (3.78)$$

Now following the similar procedure as discussed above the final form for the particle position in radial flights can be written as

$$\boxed{\frac{\Delta^2 y_p^*}{\Delta \chi^2} - 2\mu_w \frac{\Delta y_p^*}{\Delta \chi} - y_p^* = \left(\frac{r_H - \mu_w r_p}{R} \right) + \frac{1}{Fr} (\mu_w \cos \chi - \sin \chi)} \quad . \quad (3.79)$$

where $y_p^* = \frac{y_p}{R}$.

In order to solve Eq. (3.76), it has been transformed to two simultaneous differential equations by considering

$$x_p^* = x_1, \quad \frac{\Delta x_p^*}{\Delta \chi} = x_2, \quad \text{and} \quad \frac{\Delta^2 x_p^*}{\Delta \chi^2} = \frac{\Delta x_2}{\Delta \chi} \quad .$$

Substituting these terms in Eq. (3.76) to get the following equations

$$\begin{aligned} \frac{\Delta x_1}{\Delta \chi} &= x_2 \quad , \\ \frac{\Delta x_2}{\Delta \chi} &= (2\mu_w x_2 + x_1) + \mu_w \left(\frac{r_p + r_H}{R} \right) - \frac{1}{Fr} (\mu_w \sin \chi + \cos \chi) \quad . \end{aligned} \quad (3.80)$$

Initial conditions to solve the above equations are

$$\chi_{\text{init}} = \gamma_L + 90^\circ = \delta_L - \alpha \quad ,$$

where δ_L is the Final discharge angle considered from the previous model. $x_1|_{\chi_{\text{init}}} = \left(\frac{r_p}{R} \right)$ and $x_2|_{\chi_{\text{init}}} = 0$, since the velocity of the particle for an observer in the rotating frame

is zero before sliding occurs. These equations can be solved in MATLAB using Runge-Kutta (ODE 45) method.

3.7 Theoretical number of flights

Selection of number of flights is the crucial step in the design of FRD, since this number defines the amount of material responsible for the heat and mass transfer. As this number increases, more flights can accommodate maximum quantity of material that results higher number of curtains, hence the higher contact between the gas stream and the material. This number mainly depends on the dimensions of the flight and the kinetic angle of repose. Theoretically it is maximum at minimum flight length ratio and minimum at maximum flight length ratio. However, at minimum flight length ratio the final discharge angle is very small that the number of curtains formed also become less as a result small area of contact between the solids and gas. The optimal situation for number of flights could be when the flights at the bottom of the drum must feed by the material from the cascading flights alone and there should not be any overflow of solids to the immediate flight. However, sometimes too many curtains develop negative effect due to decrease in the gap between the curtains does not allow the gas to pass through, hence poor contact can happen between the falling particles and the gas stream. Hence the prediction of the number of flights is not an easy task to accomplish, therefore a simple model can be developed by allowing a minimum angular space ($\Delta\varphi \geq \alpha + v_0$) between two adjacent flights as shown in Fig. 3.10 [37]. Where, v_0 is given by the following expression

$$\tan v_0 = \left(1 - \frac{\left(\frac{r_H}{R}\right)}{\cos \alpha} \right) \cdot \tan \gamma|_{\delta=0^\circ} \quad . \quad (3.81)$$

It is assumed that the flight holds maximum amount of material when $\delta = 0^\circ$ (see Fig. 3.10). Even though it retains more when the flight tip disengages from the bed, it can be considered ineffective, since the material overflows over the flight surface alone but cannot develop any curtain. Therefore, the expression for the theoretical number of flights allowed in the drum is given by

$$n_F = \frac{360^\circ}{\alpha + v_0} \quad . \quad (3.82)$$

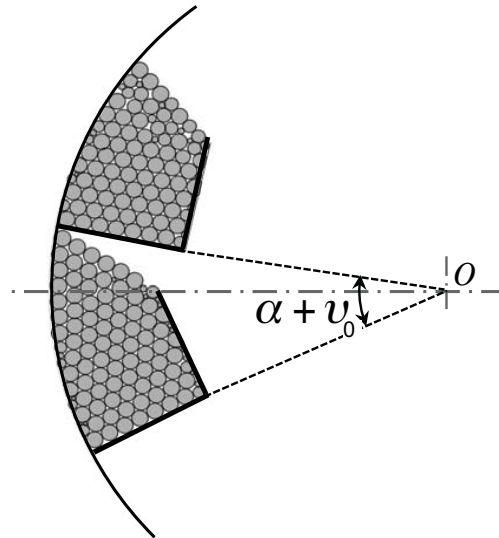


Figure 3.10: Schematic diagram to estimate the theoretical number of flights

The number of active flights can be predicted from the above relation.

3.8 Maximum flight length ratio

The geometrical parameters of the flight have great influence in the performance of the dryer. One must know that, what are the specific values to be given for the better design. With the increase of the flight length ratio ratio l_2/l_1 , the emptying point of the flight increases, which then increases the average fall time and average height. However, it is not good practice to vary this ratio arbitrarily, because at higher tangential lengths (l_2), the filling of the flight becomes more difficult which can lead to under-crowded conditions and in turn the dryer efficiency decreases. The condition to get maximum allowable tangential length can be said to be when it is equal to half of the length of the free surface of the bed (see Fig. 3.11). Therefore, the extreme value of this length can be given by

$$\left(\frac{l_2}{l_1}\right)_{max} = \frac{\sqrt{1 - \left(\frac{r_H}{R}\right)^2}}{\left(\frac{l_1}{R}\right)} \quad . \quad (3.83)$$

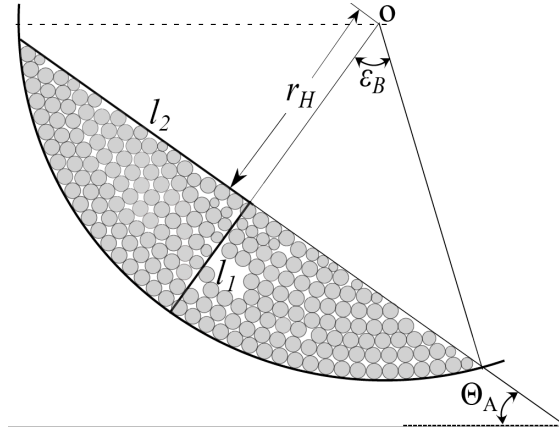


Figure 3.11: Maximum possible geometrical lengths of the flight

3.9 Height and time of fall

3.9.1 Height of curtains calculation

Height of fall determines the amount of time the particles reside in the airborne phase where they are exposed to the gas flow. It mainly depends on the filling angle of the bed (ε_B) at the bottom of the drum and the position of the flight. The particles are accelerated during the path of the travel over the flight surface, and a trajectory of particles can be observed after detaching from the flight tip. The path of the trajectories and the time of fall can be calculated from the momentum balance when the drag by gas is neglected [93, 94] or considered [95, 96]. A geometrical model has been developed in the current study to predict this height by assuming that the particles are in vertical free fall. However, in the non-vertical case the fall height increases very slightly. Blumberg and Schlünder [53] proposed a model to estimate the height of the cascading particles as a function of the discharge angle, which is only applicable for higher drum loadings. The impact of the particles on the flight sheets and on the shell wall has been neglected while calculating this height, which is considered in the present study. The curtain formation starts at that moment when the flight arises from the solid bed located at the bottom of the drum. The flight tip disengages from the bed at a certain angle ($\delta = -\zeta_A$) depending on the filling degree given by $\zeta_A = 90^\circ - \varepsilon_A - \Theta_A$ (ref. Fig. 3.1) [88]

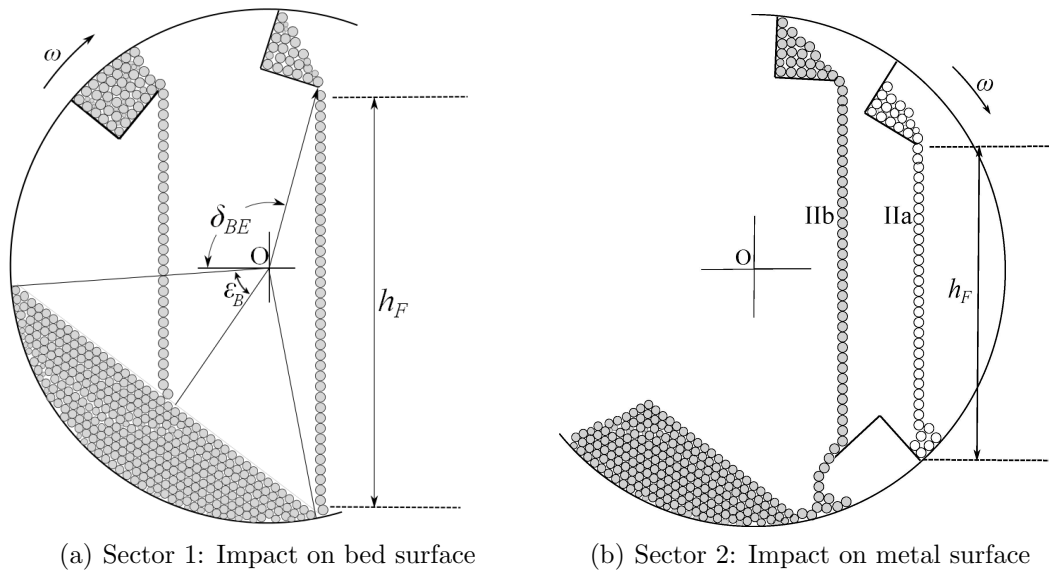
$$\varepsilon_A = \arccos \left(\frac{\cos \alpha \cdot \cos \varepsilon_B}{\left(\frac{r_H}{R} \right)} \right) . \quad (3.84)$$

The flight cannot hold the excess volume of the bed material that has been carried from the solid bed which is a measure for the over-crowded flight. At the moment when it comes out of the bed (ζ_A), the extra material i.e. higher than the angle of repose will be trickled down from the flight in the form of a big avalanche. However, this behavior can be observed only in the region $-\zeta_A < \delta < 0$. Until this point ($\delta = 0$) mostly slipping and rolling can be observed over the bed surface at the flight. The bulk motion of such behavior at the flight is said to be the kiln action. The free fall of the particles can be observed at tip angles above 0° . In earlier studies of Kelly and Ó Donnell [45] and Baker [97], the operating range of the flight tip has been considered in between $0^\circ < \delta < 180^\circ$ to calculate the height of fall. This range can be further divided into two sectors in our calculations.

Sector 1- Impact of particles on the bed surface ($0 \leq \delta < \delta_{BE}$): The particles falling from the flight will have the influence of gravity alone under no gas flow conditions. Under these circumstances, the particles hit the bed surface at the bottom of the drum until the flight tip angle is equal to δ_{BE} . This is the case when the flight tip is located vertically over the lower end of the bed as shown in Fig. 3.12(a). The scaled height of fall during this period can be given by the following equation, which is derived purely based on the geometrical considerations

$$\frac{h_F}{R} = \frac{\cos \varepsilon_B}{\cos \Theta_A} + \left(\frac{r_H}{R} \right) \cdot \frac{\sin \delta - \tan \Theta_A \cdot \cos \delta}{\cos \alpha} \quad . \quad (3.85)$$

Sector 2- Impact of particles on the metal surface ($\delta_{BE} \leq \delta < \delta_L$): In most cases, the dryers are operated in design loaded conditions, where the dense phase at the bottom is small. Hence, the cascading material does not only impacts on the bed surface but also impacts either the rotating wall or the flight sheets. The particles that are hitting the wall can become feed to the nearest flight. Various actions can be observed in this case such as bouncing, rolling or sliding. Determination of the height in this sector is rather complex than in sector 1, since the falling particles possess different components of velocity magnitudes. It is difficult to know whether if they hit the wall or flight in such cases (ref. Fig. 3.12(b)). It can be addressed depending on the number of flights equipped to the circumference of the drum. If the number of flights is small then the particles hit preferably on the wall surface, whereas in the other case the flight sheets almost form a closed circle, so that the particles strike regularly on the flight as is the case in Fig. 3.13. The latter case has been considered in the current study, since we used the theoretical number of flights for the predictions [90]. The falling height for both cases



(a) Sector 1: Impact on bed surface

(b) Sector 2: Impact on metal surface

Figure 3.12: Schematic diagram of the curtain height for the two sectors

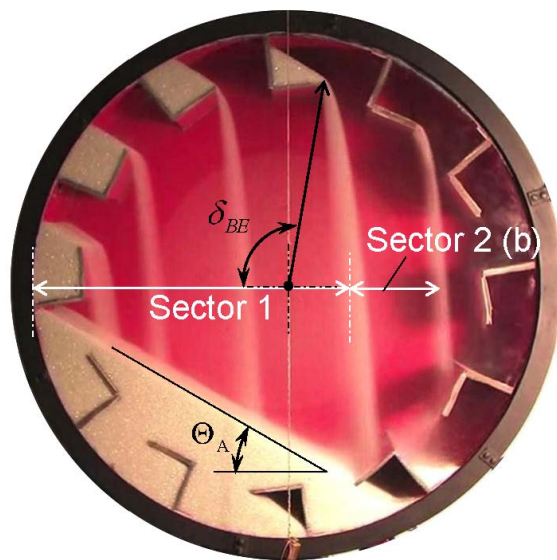


Figure 3.13: Experimental drum showing the sectors considered in the model

is given in the following.

a) Impact on inner shell of the rotating drum

$$\frac{h_F}{R} = \left(\frac{r_H}{R}\right) \cdot \frac{\sin \delta}{\cos \alpha} + \sqrt{1 - \left(\frac{r_H}{R}\right)^2 \cdot \left(\frac{\cos \delta}{\cos \alpha}\right)^2} . \quad (3.86)$$

The point of impact starts when

$$\delta_{BE} = 180^\circ - \arccos \left(\frac{\cos \alpha \cdot \sin (\varepsilon_B - \Theta_A)}{\left(\frac{r_H}{R}\right)} \right) .$$

b) Impact on flight sheets [27]

$$\frac{h_F}{R} = 2 \cdot \left(\frac{r_H}{R}\right) \cdot \frac{\sin \delta}{\cos \alpha} , \quad (3.87)$$

when, $\delta_{BE} = 90^\circ + \varepsilon_A - \Theta_A$.

3.9.2 Mean height of fall

The mean height (\bar{h}_F) of the curtains can be determined by integrating the local height over the cascading region of the flight ($0 \leq \delta \leq \delta_L$) as

$$\frac{\bar{h}_F}{R} = \frac{1}{\delta_L} \cdot \int_0^{\delta_L} \frac{h_F(\delta)}{R} d\delta . \quad (3.88)$$

The above equation can be solved numerically. Blumberg and Schlünder [53] proposed a semi empirical relation for the mean height of fall as a function of the drum filling degree (f_D), dynamic angle of repose (Θ_A) and flight length ratio.

$$\frac{\bar{h}_F}{R} = 0.85 \cdot (1 - f_D) \cdot (1.3 + \Theta_A^2) \cdot \left(\frac{l_2}{l_1}\right)^{0.13} . \quad (3.89)$$

However, the valid range of the filling degree was observed to be too high to use for the industrial application

$$\begin{aligned} 0.2 &\leq f_D \leq 0.4 & , \\ \frac{\pi}{8} &\leq \Theta_A \leq \frac{\pi}{4} & , \\ 0.75 &\leq \frac{l_2}{l_1} \leq 1.0 & . \end{aligned} \quad (3.90)$$

3.9.3 Falling time

The time of fall of the particles (t_F) is the time of travel of the particles in the gas zone from the flight tip to the point of impact, which can be calculated based on the vertical free fall [38, 98]. Therefore, we write t_F as a function of Froude number

$$t_F = \frac{1}{\omega} \cdot \sqrt{2 \cdot \text{Fr} \cdot \frac{h_F(\delta)}{R}} \quad . \quad (3.91)$$

Average time of fall is given based on the average height of fall

$$\bar{t}_F = \sqrt{\frac{2 \cdot \bar{h}_F}{g}} \quad . \quad (3.92)$$

Dimensionless form is given by

$$\bar{t}_F = \frac{1}{\omega} \cdot \sqrt{2 \cdot \text{Fr} \cdot \frac{\bar{h}_F}{R}} \quad . \quad (3.93)$$

3.10 Gas-solid contact area

3.10.1 Effective particle surface area

The transfer coefficients and the area of transfer are the necessary parameters to be known to predict the amount of heat and mass transfer. In general, various heat transfer surfaces can be observed in rotary dryers similar to kilns [99]. They include the transfer surface between the drum wall to the solid bed, gas to the exposed surface of the bed, gas to wall, and gas to the solids in the curtain. Among all, the heat transfer is mainly influenced by the gas to solids contact area. This is because individual particles are exposed to hot gas during the time of fall while the rest of the time they spend in the dense phase. This happens to be a periodic process, since an individual particle is exposed to hot conditions in regular intervals, whereas the material in the dense phase has less possibility of exposure to the hot conditions. Therefore, the rate of exposure to the hot gas is higher for the particles in the air borne phase. Since the measurements of this subject are limited, the importance of the model development increases. In this study, the total surface area of the falling particles is calculated by assuming that all particles are spherical in shape and no shielding of the neighboring particles are considered. It is also assumed that the curtain porosity is higher (close to unity), as compared to the bulk

bed porosity, hence neglected. The local transfer area of the i^{th} curtain can be defined as

$$A_{cs,i}(\delta) = \frac{6 \cdot m_{cs,i}(\delta)}{d_p \cdot \rho_s} \quad . \quad (3.94)$$

where $m_{cs,i}(\delta)$ is the amount of material presented in the form of curtain given by

$$\frac{m_{cs,i}(\delta)}{\rho_b \cdot \pi R^2 L} = \sqrt{2 \cdot Fr \cdot \left(\frac{h_F}{R}\right)} \cdot \left(-\frac{df_{F,i}(\delta)}{d\delta}\right) \quad (3.95)$$

$$= f_{cs,i}(\delta) \quad . \quad (3.96)$$

The total surface area of the particles in the curtain then results from Eq. (3.94) to

$$\frac{A_{cs,i}}{L \cdot R} = 3\pi \cdot \left(\frac{\rho_b}{\rho_s}\right) \cdot \left(\frac{D}{d_p}\right) \cdot f_{cs,i}(\delta) \quad . \quad (3.97)$$

The area responsible for the heat transfer due to the lifting flights in rotating drums is the total particle surface area of all the curtains [53, 74], estimated based on the average value approach. The particles in every curtain are subjected to different time of exposures due to varying height of fall. This is a function of the current position of the flight and curtain filling degree described by

$$A_{cs} = n_{F,a} \cdot \bar{A}_{cs,i} \quad , \quad (3.98)$$

where $n_{F,a}$ is the active number of flights given by

$$n_{F,a} = \frac{\delta_L}{360^\circ} \cdot n_F \quad , \quad (3.99)$$

n_F is the theoretical number of flights, and δ_L is the point at which flight becomes empty, $\delta_L = 90^\circ + \alpha + \gamma_L$. $\bar{A}_{cs,i}$ is the mean particle surface area of the curtains expressed as

$$\frac{\bar{A}_{cs,i}}{L \cdot R} = 3\pi \cdot \left(\frac{\rho_b}{\rho_s}\right) \cdot \left(\frac{D}{d_p}\right) \cdot \bar{f}_{cs,i} \quad , \quad (3.100)$$

where $\bar{f}_{cs,i} = \frac{1}{\delta_L} \cdot \int_0^{\delta_L} f_{cs,i}(\delta) d\delta$.

3.10.2 Calculation of individual phases of drum

In flighted rotary dryers, the loading of the drum play essential role to determine the mean residence time of the material. It varies along the axial direction from the feed end to dryer end. However, in a given section of the drum this can be attributed to be constant, from which the distribution of solids in each phase can be obtained. Kelly and Ó Donnell [45] formulated an approach to determine the design load condition for the drum filling ratio based on the assumption that the flight loading in the lower half of the drum is the mirror image of that flight unloading process in the upper half of the drum [46]

$$f_D = \frac{n_F + 1}{2} \cdot f_{H,i}|_{(\delta=0^\circ)} \quad . \quad (3.101)$$

However, this treatment was not sufficient enough to determine each phase of the drum accurately, as it can over predict these phases due to the assumption.

Filling degree of the rotary drum with flights can be estimated from the sum of the filling degree of the dense phase of the drum at the bottom (f_B), total hold up of the active flights ($f_{F,\Sigma}$), and total hold up of the curtains ($f_{cs,\Sigma}$) [88, 100]

$$f_D = f_B + f_{F,\Sigma} + f_{cs,\Sigma} \quad , \quad (3.102)$$

where

$$\begin{aligned} f_B &= \frac{1}{\pi} \cdot (\varepsilon_B - \sin \varepsilon_B \cdot \cos \varepsilon_B) \quad , \\ f_{F,\Sigma} &= \frac{n_{F,a}}{\delta_L} \cdot \int_0^{\delta_L} f_{F,i}(\delta) d\delta \quad , \\ f_{cs,\Sigma} &= n_{F,a} \cdot \bar{f}_{cs,i}(\delta) \quad . \end{aligned}$$

The particles in a dense phase slides down the surface in the flights as well as in the rolling bed. The particles advance to a specific distance, if the drum is inclined to the horizontal, otherwise no axial displacement of the particles can be observed. However, in the present study no axial displacement or bouncing of the particles is considered.

The above equations can be applied for both design-loaded and over-loaded drums, for a given drum filling degree (f_D). In the former case the curtain height can be predicted according to Eq. (3.87) for all flight positions. Since in this case no rolling bed can be observed at the bottom of the drum, hence it can be assumed that the particles strike

only on the flight sheets during the entire period of discharge which is usual in flighted rotary drums [27]. Whereas in the later case, using the same equation over the discharge period will be subjected to large errors, since the curtain height strictly depends on the filling angle of the bed (ε_B). It can be estimated using Eq. (3.102) from the iterative procedure, to determine the filling degree of the rolling bed for a proper convergence of the solution. Earlier works on this subject neglected the influence of bed filling degree on the time of fall [53, 63]. The major assumption to solve the above relations is that the flight is filled to its maximum extent and unloading should start when the flight tip is at or below 0° .

Chapter 4

Modeling of granular transverse flow at flight surface

4.1 Analysis of transverse flow

As discussed in the previous chapter, a flowing layer develops as the material cascades over the flight surface. Continuous rolling of the particles can be observed on the flight surface, while the material is being supplied continuously by the static bed which is resting in the flight. This phenomenon can be expected similar to the transverse motion of material in rotating cylinders without flights, where a larger part of the bulk bed moving with the wall (plug flow) is transported into a flowing cascading layer on the surface of the bed [13, 101]. However a interfacial boundary exists between these two regions having few particles thickness (see Fig. 4.1). The interchange of material between the two layers occur above and below the vortex point (W). The bed surface is considered to be flat and equal to dynamic angle of repose in this case. Similarly the material surface in the flight is assumed to be flat and inclined towards the horizontal at an angle equal to kinetic angle of repose (γ). However in this case the developing cascading layer breaks at the intermediate region at the flight tip to cascade the material into the airborne phase.

Various authors studied the rolling motion behavior theoretically and modeled it successfully [13, 89, 101, 103–105] in the drums without flights. Perron and Bui [103] proposed a model by considering the material to be a non-Newtonian and the resulted mass and momentum equations were solved using FLUENT. The model of Khakhar et al. [104] described the flow motion in the active layer by considering the collisional

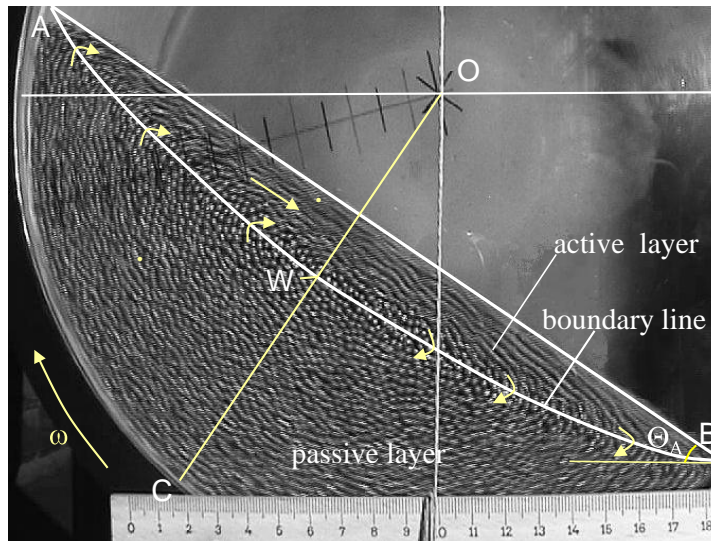


Figure 4.1: Granular motion of rolling bed in drum without flights [102]

interactions between the particles. However this model needs a fitting parameter to determine the layer thickness in order to agree with the experimental data. Mellmann et al. [101] developed a model for the rolling motion without the necessity of these fitting parameters. However, all these models regarded granular flow motion as continuum and followed Eulerian approach to model the solids motion in the cascading layer. Usually in the Eulerian approach the continuity and momentum based equations are coupled together to solve for the flow properties. In which, it is assumed that the particles are cohesionless, thin active layer when compared to the height of the bed, and the transverse velocity is several times greater than the axial velocity. Similar approach has been followed in the present study to track the developing layer at the flight surface by considering a rolling mode at the flight surface. The main objective of this work is to determine the velocity profile along the surface layer of the flight over the flight discharge which can be used in Eq. (3.18). For this purpose, a mathematical model has been developed to study the transverse motion at the flight surface based on the earlier works of Mellmann et al. [101], and Khakhar et al. [104]. In the present study these models were applied to the drum equipped with flights to determine the flow properties at the flight surface.

The schematic of the rolling bed at the flight surface for a given flight position is shown in Fig. 4.2. The surface of the layer always intersects with the drum wall at point A in region I, whereas in region II it intersects with the flight wall as shown in Fig. 4.2(b).

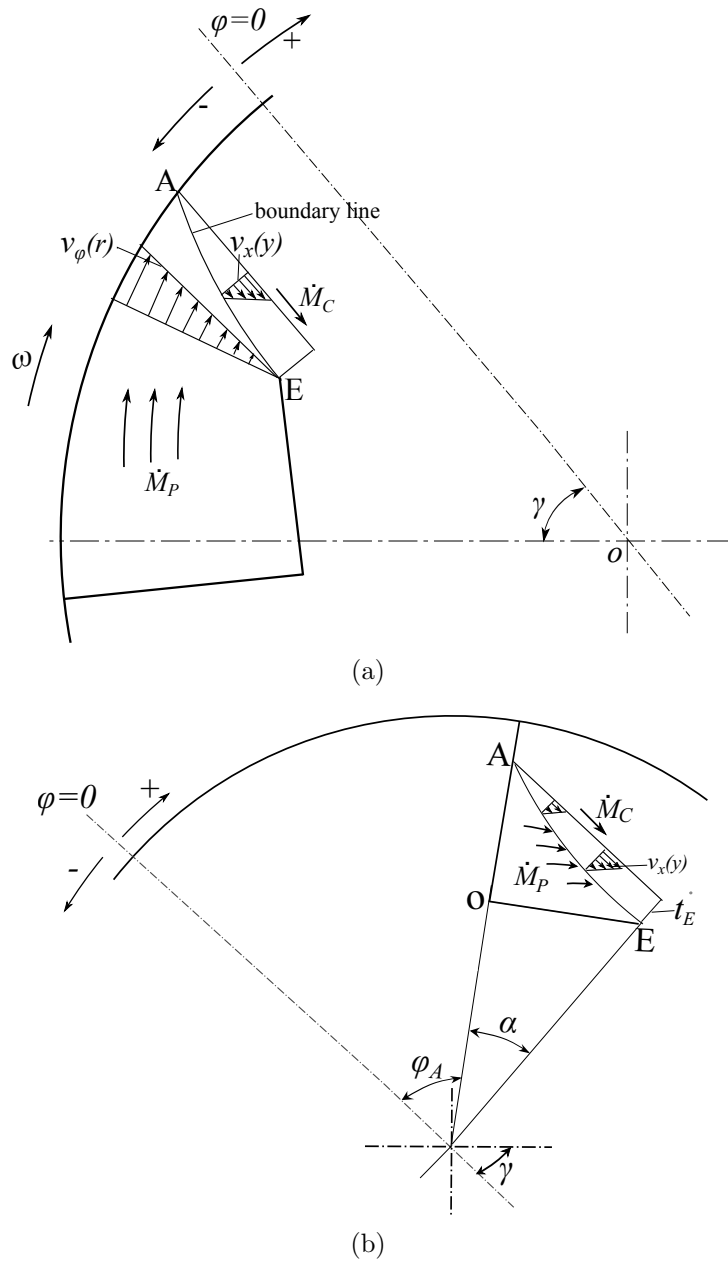


Figure 4.2: Flow motion at the flight surface in a flighted rotating drum (a) Region I: $0 \leq \delta \leq (\gamma + \alpha + \beta_n)$, b) Region II: $(\gamma + \alpha + \beta_n) < \delta \leq \delta_L$

The transition between these two regions occurs when $OA = l_1$ i.e. at $\delta = (\gamma + \alpha + \beta_n)$, where β_n is given by

$$\tan \beta_n = \frac{l_2 + p}{l_1} \quad . \quad (4.1)$$

The expression for p is given later in the chapter. The particles moving with the wall detach from the rigid bed at the boundary line to start flowing into the active layer. These particles are accelerated along the flow until the tip of the flight before cascading into the air borne phase while forming a thin layer at the surface. The maximum layer thickness (t_E) occurs at the flight tip E.

4.2 Mathematical modeling

4.2.1 Coordinate system and variables definition

At a given position of the flight (δ), the transverse motion can be assumed to be uniform in the axial direction, hence only two dimensional case is considered. The origin of the coordinate system is always fixed at the center of the drum whose x-axis is parallel to the bed surface and y-axis is perpendicular to it. The coordinate system always changes with respect to the change in flight position. The position of the differential element in Cartesian coordinates (x, y) can be determined from the polar coordinates of position (r) and the angular coordinate (φ)

$$\begin{aligned} x &= -r \cos \varphi \quad , \\ y &= -r \sin \varphi \quad . \end{aligned} \tag{4.2}$$

The coordinate system and the influencing variables of the problem were illustrated in the Fig. 4.3(a). Defining the dimension less variables as follows

$$x^* = \frac{x}{R}, \quad y^* = \frac{y}{R}, \quad \rho = \frac{r}{R}, \quad t^* = \frac{t}{R}, \quad r_E = \frac{r_H}{\cos \alpha}.$$

The local thickness of the active layer at the flight surface $t(x)$ is written as

$$t = r \sin \varphi - R \cos \epsilon^* \quad . \tag{4.3}$$

Transforming this equation into dimensionless form as

$$t^* = \rho \sin \varphi - \cos \epsilon^* \quad . \tag{4.4}$$

The auxiliary filling angle (ϵ^*) can be calculated by applying this equation at point E

$$\cos \epsilon^* = \rho_E \sin \varphi_E - t_E^* \quad . \tag{4.5}$$

4.2.2 Velocity and Mass flow

Since the particles in the rigid bed move along with the wall, hence no slip condition can be assumed within the plug flow at the boundary [13]. Therefore, the velocity of the particles in the static bed of the flight is only a linear function of the radius at constant angular velocity (ω)

$$v_\varphi(r) = \omega r \quad . \quad (4.6)$$

Mass flow of the particles from the bulk static bed to the thin active layer in the differential element of length dr is given by

$$d\dot{M}_s = \rho_{b,s} v_\varphi(r) dr L \quad . \quad (4.7)$$

Integrate from r to R after substituting Eq. (4.6) in the above equation

$$\begin{aligned} \frac{\dot{M}_s}{L} &= \rho_{b,s} \omega \cdot \int_r^R r dr \quad , \\ &= \rho_{b,s} \omega \cdot \frac{(R^2 - r^2)}{2} \quad . \end{aligned} \quad (4.8)$$

Mass flow in the active layer

$$\frac{\dot{M}_a}{L} = \rho_{b,a} \cdot \int_0^t v_x(y) dy \quad , \quad (4.9)$$

here v_x is the velocity of the particles along the active layer. However it varies across with the layer which can be assumed to be a simple shear [89, 101, 104, 105]. Therefore the velocity profile in the transverse motion distributed in linear profile with the layer thickness given by

$$v_x(y) = 2\bar{v}_x \cdot \frac{y}{t} \quad , \quad (4.10)$$

where, \bar{v}_x is the average velocity of the particles in the active layer. By substituting for $v_x(y)$ in eq. (4.9) results

$$\frac{\dot{M}_a}{L} = \rho_{b,a} \cdot \bar{v}_x t \quad . \quad (4.11)$$

By defining the dimensionless mass flow as $M^* = \frac{\dot{M}_s}{\rho_{b,s}\omega R^2 L} = \frac{\dot{M}_a}{\rho_{a,s}\omega R^2 L}$. From the principle of continuity, Eq. (4.8) and (4.11) become equal ($\dot{M}_a = \dot{M}_s$). Although the density of the cascading layer is different from the density of bulk static bed the change is neglected by considering $\rho_{b,s} = \rho_{b,a} = \rho_b$. Applying these conditions and transform into dimension less form for the mass flow

$$M^* = \frac{(1 - \rho^2)}{2} \quad , \quad (4.12a)$$

$$= \bar{v}_x^* t^* \quad . \quad (4.12b)$$

Finally from the above relation we obtain

$$\bar{v}_x^* = \frac{(1 - \rho^2)}{2t^*} \quad . \quad (4.13)$$

4.2.3 Force balance in the active layer

Figure 4.3(a) shows a differential element of the layer of length dx , and radial length of dr , the thickness of which increased by dt . The element is inclined to horizontal about an angle η , and v is the angle between the surface line and boundary line. The varying gradient of the layer is expressed as

$$\tan v = -\frac{dy}{dx} = \frac{dt}{dx} = \frac{dt^*}{dx^*} \quad . \quad (4.14)$$

The relation between the increase in the radial length and transverse length is written as [14]

$$\frac{dr}{dx} = -\frac{\cos(\varphi + v)}{\cos v} \quad . \quad (4.15)$$

The particles in the flowing layer have been subjected to frictional, gravitational, and inertial forces along the transverse direction. Since the flowing particles are less subjected to centrifugal force hence it can be neglected. The length related force balance for the differential element as shown in Fig. 4.3(b) is written as

$$\Sigma \mathbf{F} = \mathbf{F}_F + \mathbf{F}_N + \mathbf{F}_G + \mathbf{F}_I = \mathbf{0} \quad (4.16)$$

The component of the forces are given by

$$\begin{aligned} F_N &= F_G \cos \eta + F_I \sin v \quad , \\ F_F &= F_G \sin \eta - F_I \cos v \quad , \end{aligned} \quad (4.17)$$

where, $\eta = \gamma + v$.

Gravity acting on the particle of mass of the element dm_p is given by

$$F_G = \rho_b t dx \cdot g \quad , \quad (4.18)$$

The rolling particles undergoes to inertial force along the layer given by

$$F_I = \rho_b t dx \cdot \bar{v}_x \frac{d\bar{v}_x}{dx} \quad . \quad (4.19)$$

From Coulomb's law of friction, the resultant force is (μ_m) times the normal force at the boundary.

$$F_F = \mu_m \cdot F_N \quad . \quad (4.20)$$

The coefficient of friction (μ_m) varies at each location of the boundary, the calculation of which is discussed later in the chapter. Substituting for F_F and F_N from Eq. (4.17) in the above equation, we obtain the following equation for the motion of particles after dividing with $\rho_b t dx$ and rearranging

$$\bar{v}_x \frac{d\bar{v}_x}{dx} + \frac{g[\mu_m \cos \eta - \sin \eta]}{\mu_m \sin v + \cos v} = 0 \quad . \quad (4.21)$$

Transform the above equation into dimensionless form by defining, $\bar{v}_x^* = \frac{\bar{v}_x}{R\omega}$, $Fr = \frac{\omega^2 R}{g}$

$$\bar{v}_x^* \frac{d\bar{v}_x^*}{dx^*} + \frac{1}{Fr} \cdot \frac{\mu_m \cos \eta - \sin \eta}{\mu_m \sin v + \cos v} = 0 \quad . \quad (4.22)$$

Differentiate eq. (4.12b), to derive a relation for the mass flow gradient

$$\tan v = \left(\frac{dM^*}{dx^*} - t^* \cdot \frac{d\bar{v}_x^*}{dx^*} \right) \cdot \frac{1}{\bar{v}_x^*} \quad . \quad (4.23)$$

Further the mass flow gradient can be expressed as $\frac{dM^*}{dx^*} = \frac{dM^*}{d\rho} \cdot \frac{d\rho}{dx^*}$.

Taking the differential terms as

$$\frac{d\bar{v}_x^*}{dx^*} = v'_x, \frac{dM^*}{dx^*} = M', \frac{dt^*}{dx^*} = t' \quad .$$

Then using eq. (4.12a) and Eq. (4.15)

$$\begin{aligned} M' &= \rho \cdot \frac{\cos(\varphi + v)}{\cos v} \quad , \\ &= (\rho \cos \varphi - \rho \sin \varphi \cdot \tan v) \quad , \\ &= (-x^* + y^* t') \quad . \end{aligned} \tag{4.24}$$

Substitute eq. (4.23) in eq. (4.24).

$$M' = \left\{ -x^* + \frac{y^*}{\bar{v}_x^*} \cdot (M' - t^* v'_x) \right\} \quad . \tag{4.25}$$

After simplification of the above equation we obtain the equation of the following form

$$\boxed{M' = -\frac{(x^* \bar{v}_x^* + y^* t^* v'_x)}{\bar{v}_x^* - y^*}} \quad . \tag{4.26}$$

Substituting for η in eq. (4.22) and rearranging yields the following relation

$$\bar{v}_x^* \frac{d\bar{v}_x^*}{dx^*} (1 + \mu_m \tan v) = \frac{1}{Fr} \cdot (a_2 + a_1 \tan v) \quad , \tag{4.27a}$$

$$\bar{v}_x^* v'_x (1 + \mu_m t') = \frac{1}{Fr} \cdot (a_2 + a_1 t') \quad , \tag{4.27b}$$

where

$$a_1 = \cos \gamma + \mu_m \sin \gamma \quad ,$$

$$a_2 = \sin \gamma - \mu_m \cos \gamma \quad .$$

To represent t' in terms of v'_x , substitute M' from eq. (4.26) in eq. (4.23) after simplification

$$t' = \frac{(x^* + t^* v'_x)}{y^* - \bar{v}_x^*} \quad . \tag{4.28}$$

To evaluate v'_x , substitute t' from eq. (4.28) in eq. (4.27b) we obtain a quadratic equation

$$a (v'_x)^2 + b v'_x + c = 0 \quad . \quad (4.29)$$

The solution of this equation becomes

$$v'_x = \frac{(-b - \sqrt{b^2 - 4ac})}{2a} \quad , \quad (4.30)$$

where a, b, and c can be written as

$$a = \frac{\mu_m \bar{v}_x^* t^*}{y^* - \bar{v}_x^*} \quad , \quad (4.31a)$$

$$b = \left[\frac{\mu_m \bar{v}_x^* x^*}{y^* - \bar{v}_x^*} + \bar{v}_x^* - \frac{a_1 t^*}{\text{Fr}(y^* - \bar{v}_x^*)} \right] \quad , \quad (4.31b)$$

$$c = - \left[a_2 + \frac{a_1 x^*}{y^* - \bar{v}_x^*} \right] \frac{1}{\text{Fr}} \quad . \quad (4.31c)$$

4.2.4 Coefficient of friction

To determine the motion behavior at the flight surface, it is important to predict the coefficient of friction at each position of the layer at a given position of the flight. According to Mellmann et al. [101], the frictional coefficient is considered to vary with the local position of the boundary line between the static bed and the cascading layer. Since the boundary profile does not vary linearly, the coulombic friction is not constant along the boundary line. Generally, in drums without flights, the coefficient of friction is referred to the coulombic form as the tangent of dynamic angle of repose at the vortex position (W), where there is no interchange of material between the two layers [102]

$$\mu_m|_{x=0} = \tan \Theta_A \quad .$$

Similarly in the case of rotary drum with flights assuming an auxiliary vortex point, the coefficient of friction can be written as

$$\mu_m|_{x=0} = \tan \gamma \quad .$$

Above this point, the friction at the boundary line increases from the vortex point where it is maximum at the apex position (point A), hence the angle at the boundary line should also increase. Therefore the friction coefficient at point A is characterized with

$$\mu_m|_{x=x_A} = \tan \eta_A = \tan (\gamma + v_A) \quad .$$

By taking these points as reference the friction coefficient is considered to vary linearly at the boundary line along the transverse motion which can be expressed as

$$\mu_m = \tan \gamma + [\tan (\gamma + v_A) - \tan \gamma] \frac{x}{x_A} \quad , \quad (4.32)$$

where v_A is the angle between the surface line and boundary line. To predict the coefficient of friction the characteristics of the material v_A and γ should be known. Here, v_A is the material property which can be measured with the aid of photos collected from the experiments. In the present study the empirical equation developed by Liu [102] has been used, which is assumed to be independent of flight position until $\delta \leq \gamma$

$$v_A = 0.32\Theta_A (1 + f_D) + 1800\sqrt{\frac{d_p}{D}} \text{Fr} \quad , \quad (4.33)$$

here Θ_A in $[\circ]$, v_A also in $[\circ]$. When $\delta > \gamma$, it is assumed that v_A decreases linearly with the flight position by a factor of

$$v_A = \frac{\delta_L - \delta}{\delta_L - \gamma} \left[0.32\Theta_A (1 + f_D) + 1800\sqrt{\frac{d_p}{D}} \text{Fr} \right] \quad . \quad (4.34)$$

4.3 Simulation methodology

4.3.1 Initial conditions

The initial positions (x_A^*, y_A^*) to solve the system of equations (eqs. (4.26) and (4.30)) varies for the two regions. Therefore they are described separately for each case in the following. However, the exit points (x_E^*, y_E^*) are unique in both the cases

$$\begin{aligned} x_E^* &= -\rho_E \cos \varphi_E \quad , \\ y_E^* &= -\rho_E \sin \varphi_E \quad . \end{aligned} \quad (4.35)$$

where $\varphi_E = (\gamma - \delta)$.

4.3.1.1 Region-I: $0 \leq \delta \leq (\gamma + \alpha + \beta_n)$

The position of the point A is initially unknown, since the thickness of the layer is unknown. The initial point depending on the layer thickness at flight tip (δ_E) is given by

$$\begin{aligned} x_A^* &= -\sin \epsilon^* \quad , \\ y_A^* &= -\sin \varphi_A \quad . \end{aligned} \quad (4.36)$$

where

$$\varphi_A = \arcsin(\cos \epsilon^*) \quad . \quad (4.37)$$

4.3.1.2 Region-II: $(\gamma + \alpha + \beta_n) < \delta \leq \delta_L$

The schematic for the second region is shown in Fig. 4.4(a). It is clear from the figure that the boundary points are different from the first region. Since in the first case the surface line intersects the cylinder wall (see Fig. 4.4(a)), whereas in the second region it intersects the flight. Therefore ρ_A varies for each flight position as it continuously discharges the material from the flight, which can be calculated as follows from Fig. 4.4(b)

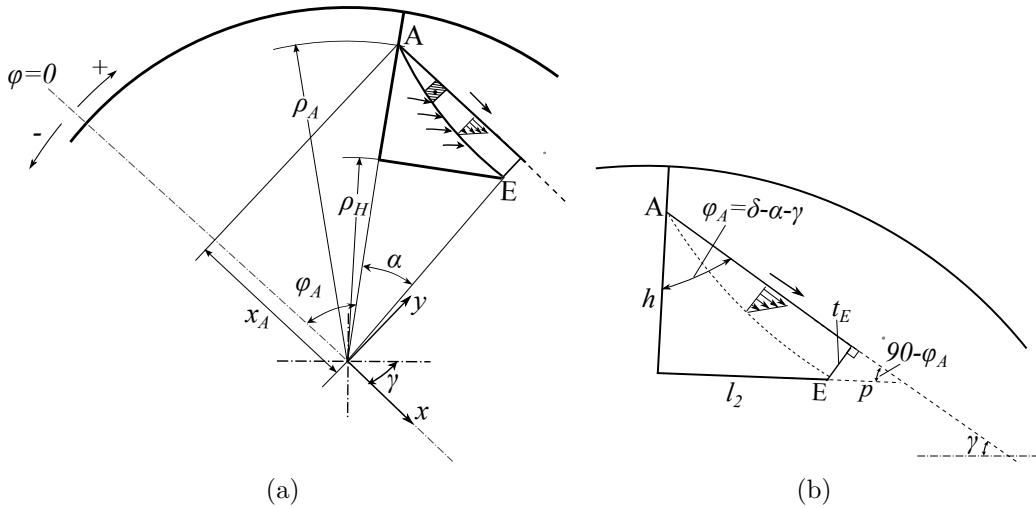


Figure 4.4: Schematic of the flighted rotary drum to model the cascading layer profile in region-II

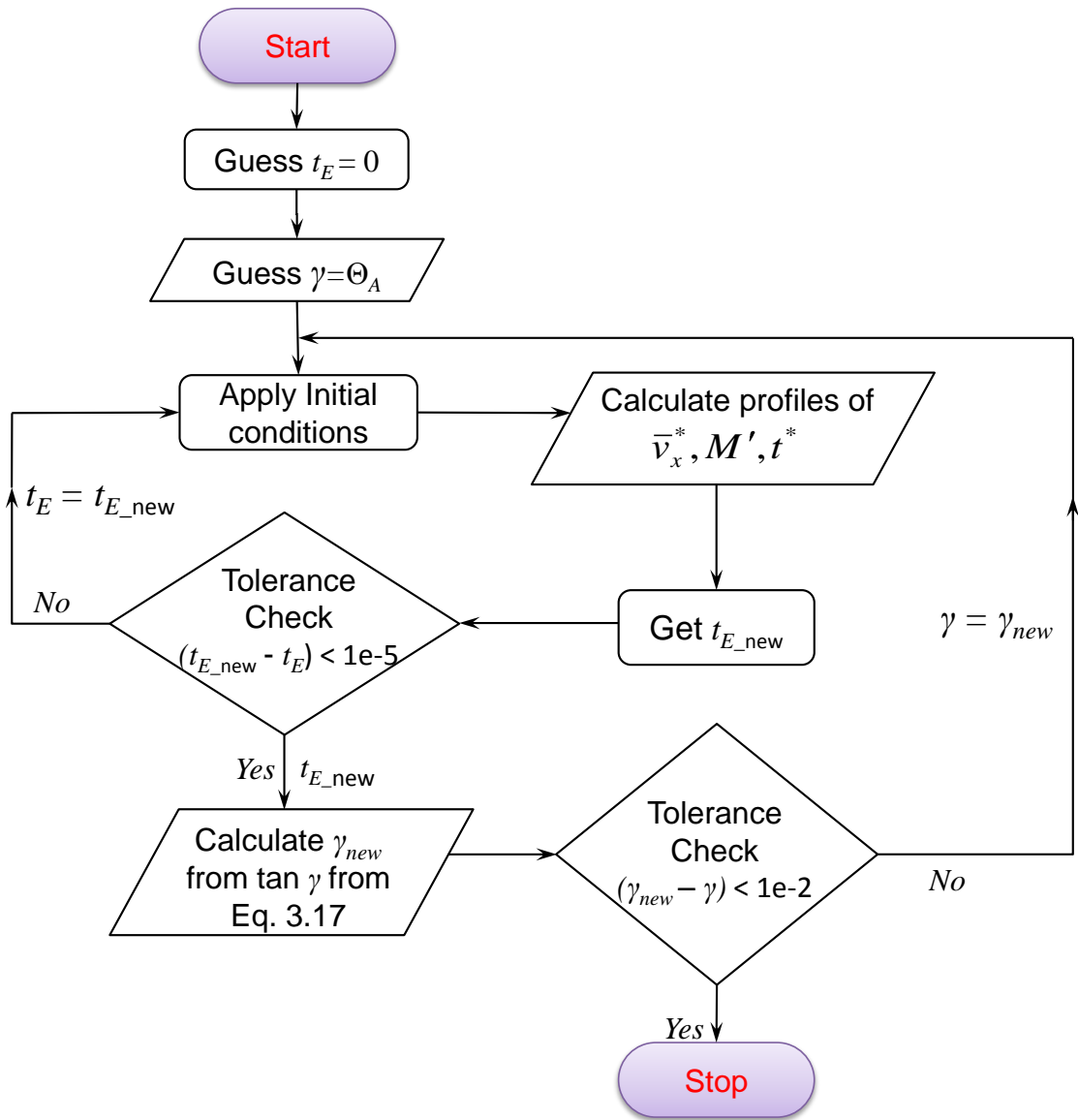


Figure 4.5: Simulation flow sheet for the motion equations

$$\begin{aligned}\rho_A &= \rho_H + (h/R) \quad , \\ h &= \frac{l_2 + p}{\tan \varphi_A} \quad , \\ p &= \frac{t^*_E}{\sin(90 - \varphi_A)} = \frac{t^*_E}{\cos \varphi_A} \quad .\end{aligned}$$

where φ_A in this case is given by $\varphi_A = \delta - \gamma - \alpha$.

Initial conditions for the two dependent variables from eqs. (4.30) and (4.26) are

$$\begin{aligned}\bar{v}_x^*|_{x_A^*} &= \rho_A \quad , \\ M'|_{x_A^*} &= \bar{v}_x^*|_{x_A^*} \cdot t^*|_{x_A^*} \quad .\end{aligned} \tag{4.38}$$

In order to get proper numerical solution, $t^*|_{x_A^*}$ is assumed to be a thickness equal to half of one particle diameter [101]. Therefore $t^*|_{x_A^*} = d_p/D$, where d_p is the particle diameter and D is the drum diameter.

4.3.2 Solution procedure

The motion equations for \bar{v}_x^* , M^* (Eqs. (4.26) and (4.30)) were solved in MATLAB. After including the friction coefficient (Eq. (4.32)) in the motion equations the differential equations become more complex. It becomes substantially difficult to solve explicitly for γ and t^* . One would start by taking some initial guess for both γ and t^* . The flow sheet to solve these expressions is shown in Fig. 4.5. For each γ a local convergence for the layer thickness at flight tip (t_E) must be accomplished and then using this converged profiles for velocity a new γ can be obtained using Eq. (3.18). The motion profiles are calculated until a converged solution for both γ and t_E is attained.

Chapter 5

Experimental Setup and Description

5.1 Experimental Setup and Procedure

The experimental setup employed for the present study is shown in Fig. 5.1. Experiments were performed with two drum sizes of diameter 500 mm and 1000 mm (see Fig. 5.2) by maintaining $L/D=0.3$. The drum was directly fixed at the shaft of a gear motor (0.18kW IP 55, 300Nm B3i=252.75, 230/400V 50Hz 1.16/0.67A) attached to a base frame standing on a table. The drum was aligned horizontally with no inclination to maintain uniform axial profiles. The front end of the drum was covered with a circular glass plate and the rear end with a metal wall. The provision of the glass provides to enable high quality images from the videos of the experiments. The inner part of the drum was painted with red color in order to observe the showering particles clearly in the recorded videos. High definition camera (1080p, 30 fps, JVC GZ-HD7E) had been arranged perpendicular to the plane of the glass and focusing always to the center of the drum. The usage of the camera enables to record the videos of the experiments, which later can be processed to analyze the images. Enough care must be taken to position the camera in order to avoid parallax errors. The drum was equipped with rectangular flights separated by equal angular distance. The experiments were carried out in a dark room to avoid the light reflections on the glass plate. A plumb bob was suspended vertically with the help of a stand at the center of the drum to locate the drum center position and to measure the dynamic and kinetic angles of repose.

At the beginning of the experiment, the drum was filled with the granular material

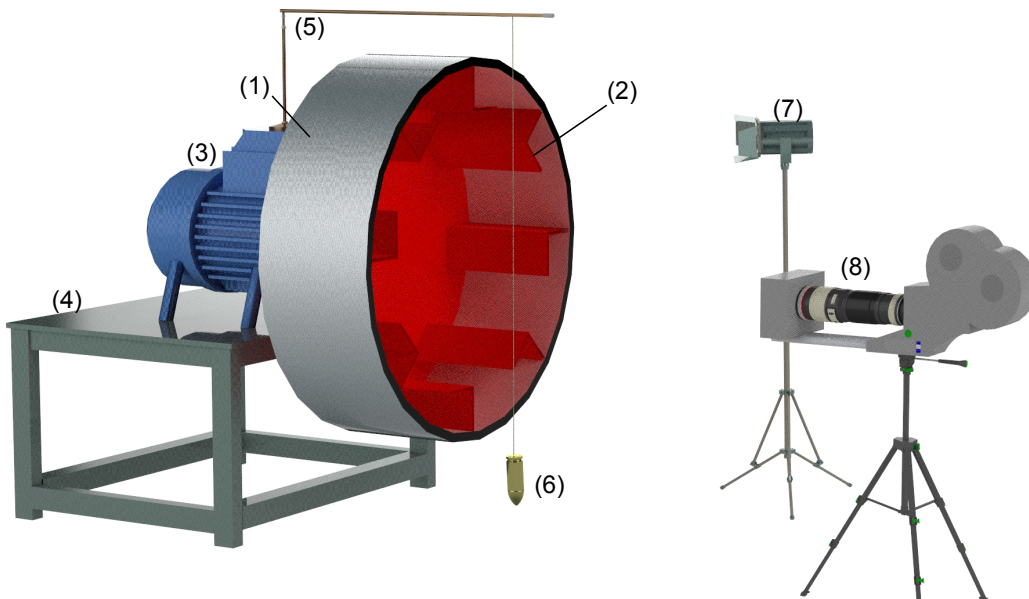


Figure 5.1: Experimental setup of the flighted drum: 1) experimental drum 2) rectangular flights 3) gear motor 4) table 5) stand 6) plumb bob 7) light 8) camera

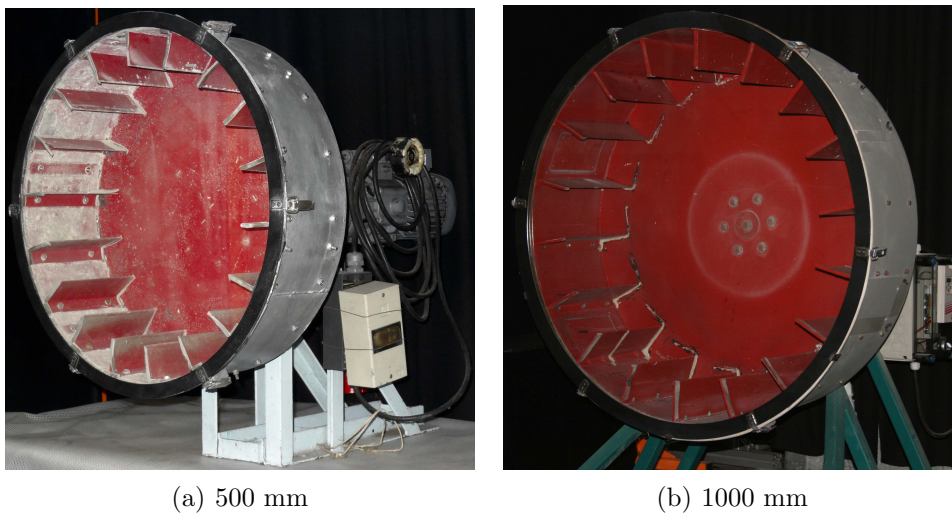


Figure 5.2: Experimental drums

to the desired filling degree. Enough care had to be taken to position the camera perpendicular to the drum. Then the drum was adjusted to the desired rotational speed. The action of the flights that shower the material in the free space was captured with a high definition camera that has the strength of recording 30 frames per second. Later the im-

ages were collected from these videos to estimate the kinetic angle of repose of a single flight and the height of the curtains at various positions of the flight tip. This angle was given as input to the model to predict the flight cascading rate. In order to reduce the errors, more data was collected from different flights and the procedure was repeated. The standard deviation of the kinetic angle of repose was about $\pm 0.6^\circ$.

Table 5.1: Bed material properties used for the experiments

Material	d_p (mm)	ρ_b (consolidated) (kg/m ³)	Moisture (%)	Θ_A ($^\circ$)
quartz sand	0.2	1570	0	32.4
glass beads	0.7	1560	0	28.0
limestone(Y14)	6.1	1200	14	48.6
limestone(Y0)	6.1	1293	0	31.4
limestone(G2.5)	2.5	1380	0	37.5
limestone(G5)	3.0	1460	1-3	36.5
limestone(G25)	8.8	1654	1-3	35

5.2 Materials and conditions

Two different materials such as quartz sand (0.2 mm) and glass beads (0.7 mm) were used in the study for the model validation. These test materials are free flowing and non-cohesive in nature. However, the experiments were also performed with other cohesive materials (see Fig. 5.3) to observe their motion behavior for the same set of conditions. The properties of which are given in Table 5.1. The consolidated bulk density of the material is the mean density of the material evaluated for different samples at room

Table 5.2: Parameters operated for the experiments

S.No	Parameter	Value
1.	Diameter, D	0.5 m, 1 m
1.	L/D	0.3
2.	l_1/R	0.2
3.	l_2/l_1	1.0, 0.75, 0.375, 0
4.	n	2-12 rpm
5.	f_D	0.05-0.3
6.	n_F	12, 18

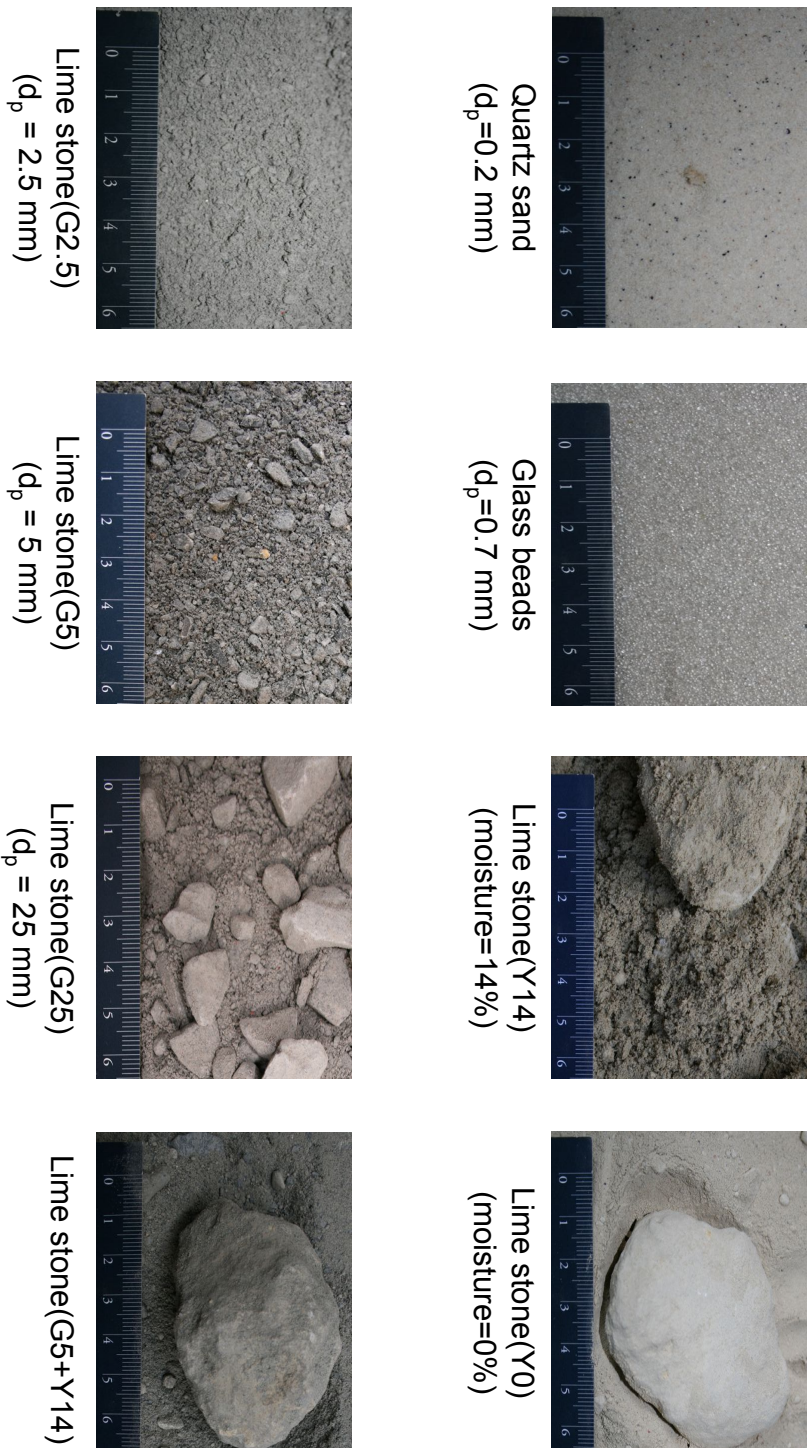


Figure 5.3: Images of the materials used to perform experiments

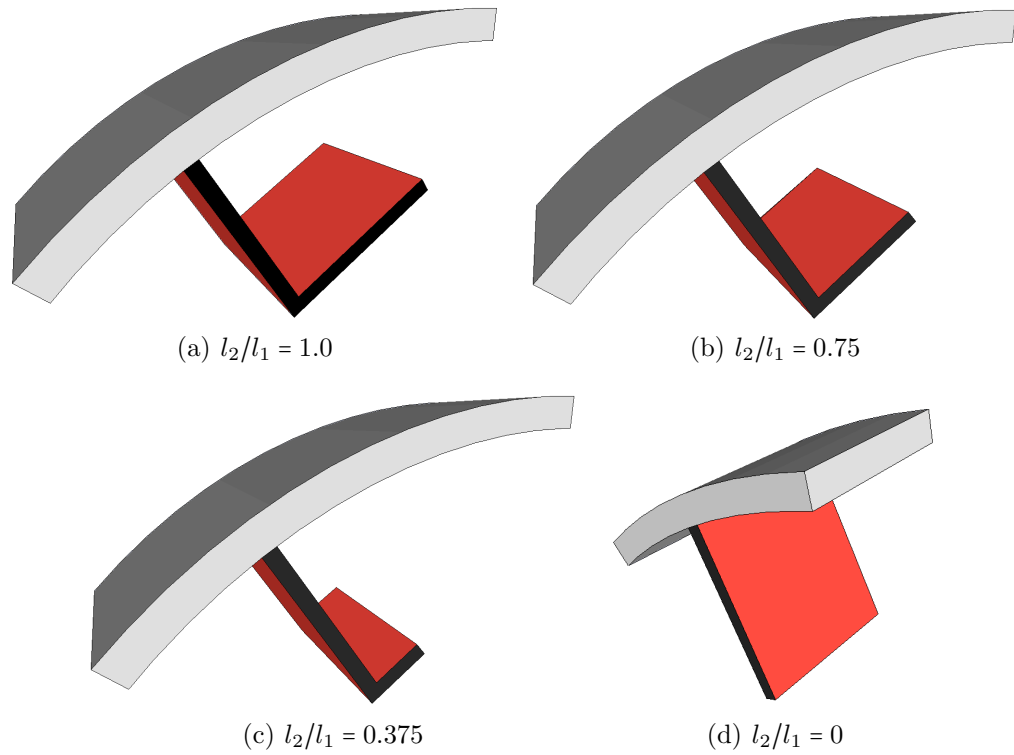


Figure 5.4: Flight profiles used in the experiments

temperature. The dynamic angle of repose of the test materials was measured from the images of the flat surface of the bed when the material was rotated in a drum without flights ($f_D = 10\%$; $Fr = 0.0007$). Experiments were performed with four different profiles of the rectangular flight by operating the flight length ratio at 1.0, 0.75, 0.375, and 0 such as shown in Fig. 5.4. The tangential length of the flight has been systematically reduced to maintain the given ratio. Whereas l_1/R is maintained at 0.2 for all the experiments. The number of flights were operated at 12 and 18. The experiments were performed for all combinations at various rotational speeds up to 12 rpm. The experimental settings are listed in Table 5.2.

Chapter 6

Experimental measurements and model validation

6.1 Kinetic angle of repose

The kinetic angle of repose was calculated from Eq. (3.12) and plotted against the discharge point of the flight for quartz sand at different Fr_m (0-1.0) as shown in Fig. 6.1. The dimensions of the flight include $l_1/R = 0.2$, $l_2/l_1 = 1.0$. It depicts that the discharge point has no significant effect on kinetic angle at low Froude numbers, but it is increasingly dependent at higher values. The extreme value of the kinetic angle at a given Fr can be found at $\delta = \sin^{-1} Fr_m$. At $Fr_m = 1$ $d\gamma/d\delta = 0.5$ at all discharge angles (δ). Earlier authors studied the validity of the model at ($Fr > 0.1$) [44], but the practical range of Froude number is much lower than 0.1. Hence in the present study the predictions and the measurements were carried out at $Fr=0.0011$.

Experiments were performed at different flight length ratios in order to validate the model. The data points of kinetic angle of repose were calculated for a series of frames extracted from the videos of the experiments at different intervals by focusing on one single flight until the emptying point. The calculation of the kinetic angle from one such image is exemplified in Fig. 6.2(a)-(d) at different flight length ratios. The center of the drum can be located with the use of the plumb line as shown in the figure, which is used to measure the position of the flight. This procedure was repeated for several other images to measure the surface angle at the other positions of the same flight. In order to reduce the errors, more data was collected from another flight, which is selected randomly and the procedure was repeated for the same experiment.

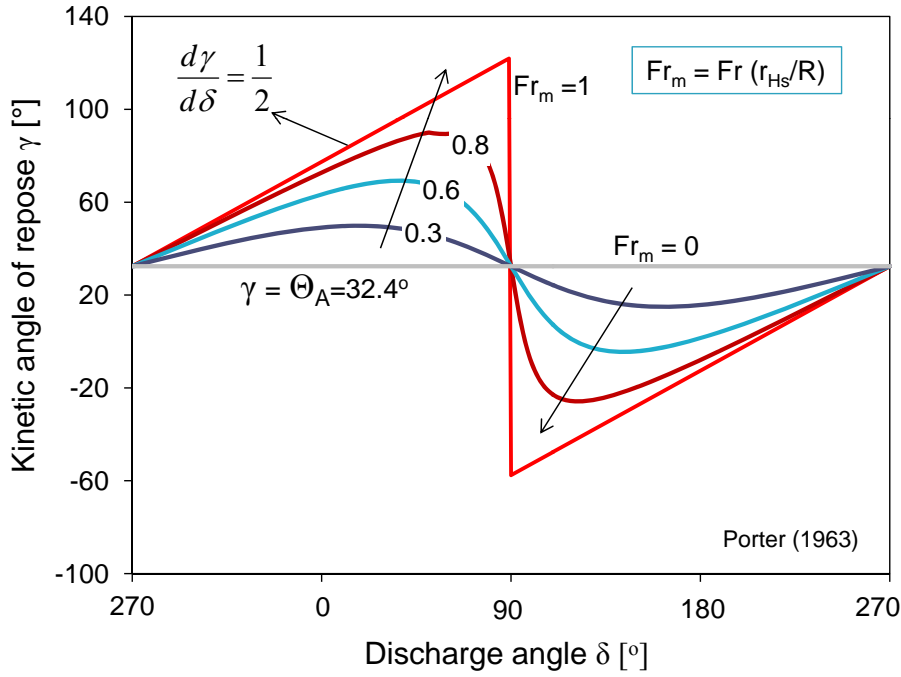


Figure 6.1: Kinetic angle of repose versus discharge angle and Froude number, calculated for quartz sand

The experimental findings are compared against the model predictions for quartz sand at $Fr=0.0011$ as shown in Fig. 6.3. Figure 6.3(a) - (d) represent the effect of the discharge angle on the kinetic angle of repose at different l_2/l_1 values 1.0, 0.75, 0.375, and 0 respectively. The model predictions in the figure are represented with solid lines and the measured data is denoted with the symbol (\circ). Each data point in the figure corresponds to one single image that was collected for one flight at that specific position. From the figure, it is clear that the KAR is observed to be constant for Schofield and Glikin [43] model. Since, it was assumed only a single particle layer by neglecting the flowing layer at the flight surface. The experimental measurements noticed $\approx 5^\circ$ increase in KAR during the initial period of discharge and then decreases in later stages. Due to considerable difference is observed between the measured data and the model of Schofield and Glikin, the model was extended by considering the inertial force at the flight surface as given by Eq. (3.18) which is solved numerically and the predictions were represented with red color in the figure. This extended model depicted the similar tendency as it was observed with the measured data. However, the slight shift of the experimental data can be attributed to measurement errors, effect of glass front wall, and the angle of flight to the camera position. The percentage error is approximately 5-10%, which falls under the

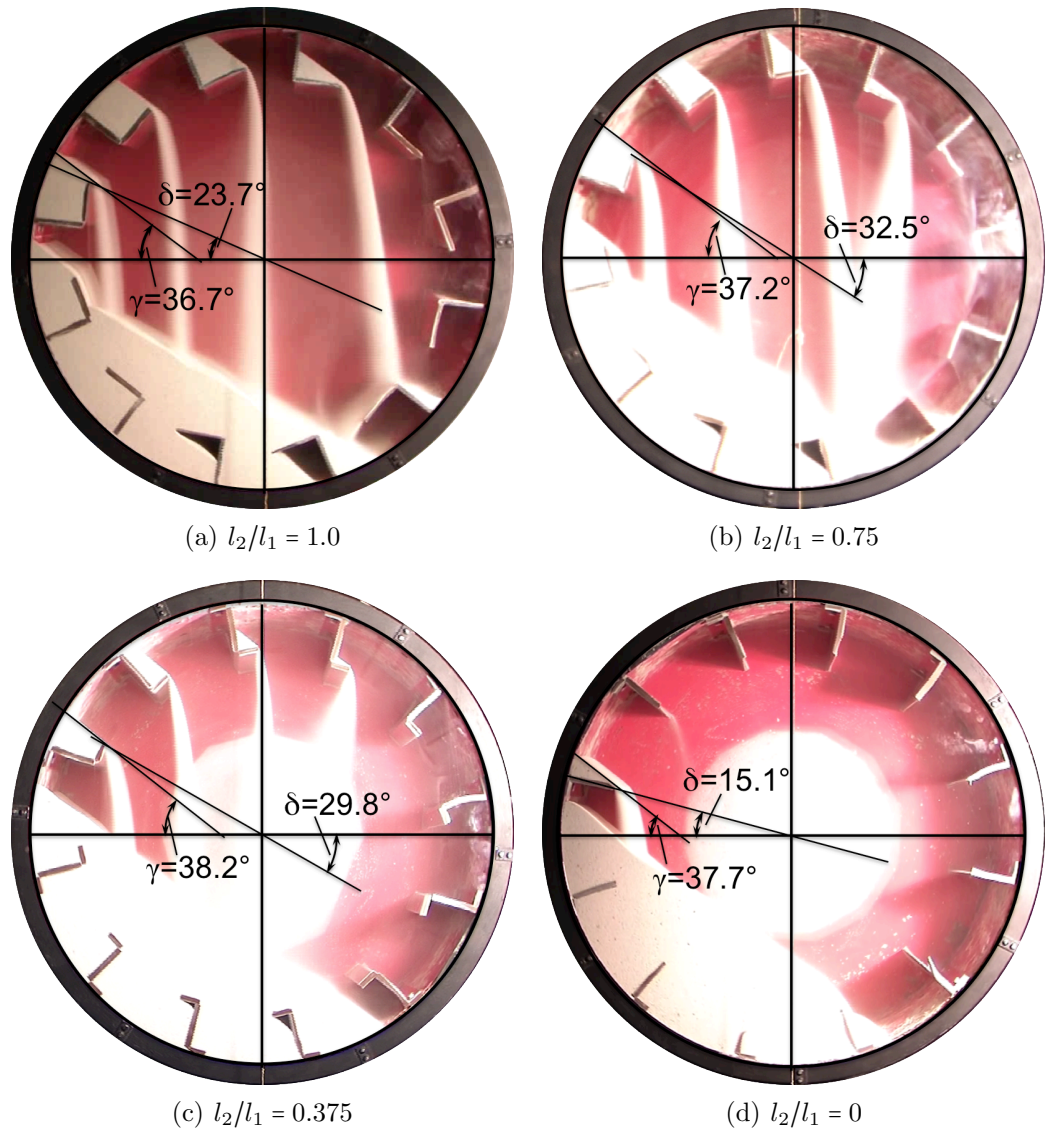


Figure 6.2: Images of the experimental drum showing the calculation of kinetic angle at different flight length ratios: Quartz sand (0.2 mm), $Fr=0.0011$, $n_F=12$

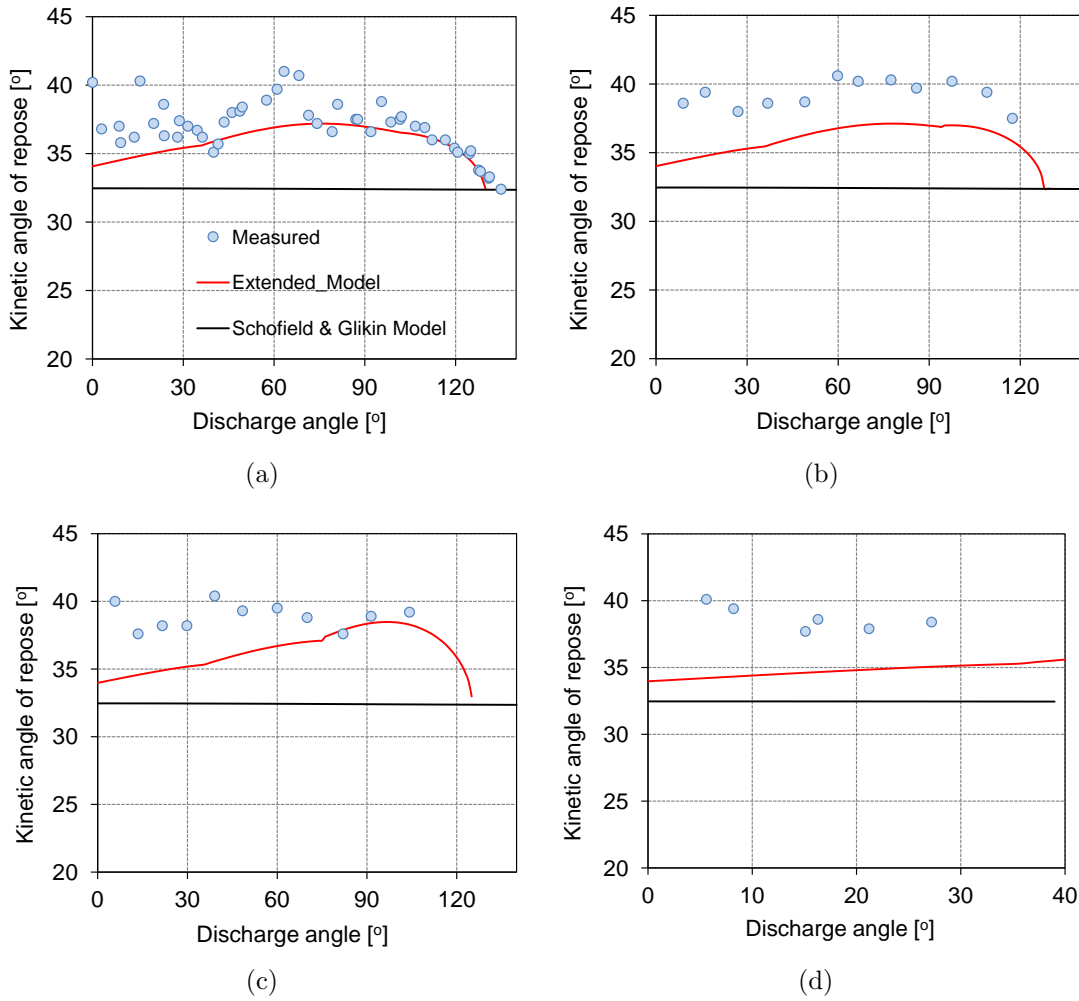


Figure 6.3: Experimental validation of Eqs. (3.12) and (3.18): Kinetic angle of repose versus discharge angle at different length ratio's for quartz sand ($Fr = 0.0011$) a) $l_2/l_1 = 1.0$, b) $l_2/l_1 = 0.75$, c) $l_2/l_1 = 0.375$, d) $l_2/l_1 = 0$

practical range. Similar behavior is observed for glass beads under the similar operating conditions which is shown in Fig. 6.4.

The validity of the extended model needs thorough investigation, since this equation depends on the velocity gradient at the layer surface. Again this gradient depends on the parameter v_A , which was determined based on an empirical equation. Hence, the velocity and layer thickness profiles also need to be validated before using this extended model in the geometrical modeling of flight which is out of scope of this thesis. Therefore, the model of Schofield and Glikin [43] has been considered to determine the different phases of the drum for flight design. According to Kelly and Ó Donnell [45] this equation

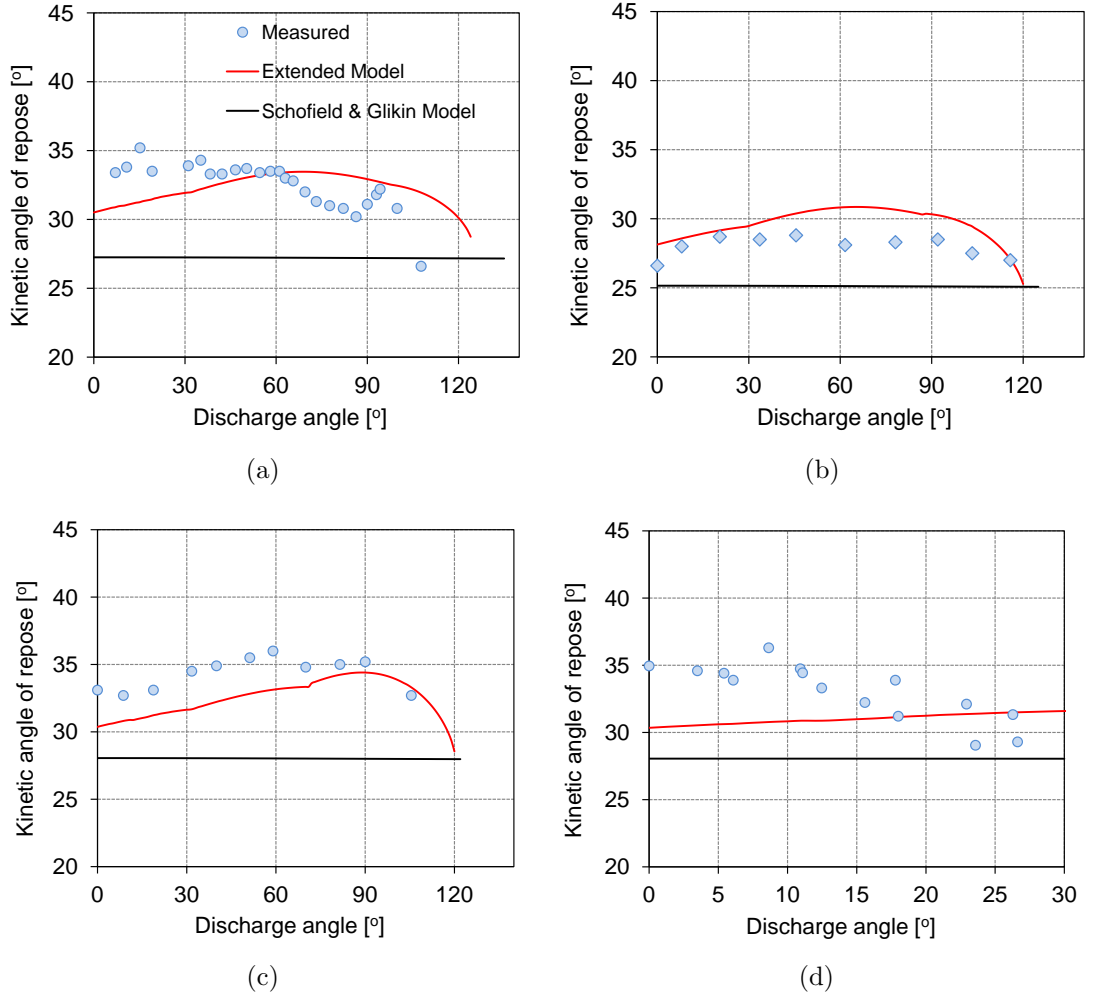


Figure 6.4: Experimental validation of Eqs. (3.12) and (3.18): Kinetic angle of repose versus discharge angle at different length ratio's for glass beads a) $l_2/l_1 = 1.0$, b) $l_2/l_1 = 0.75$, c) $l_2/l_1 = 0.375$, d) $l_2/l_1 = 0$. Symbols denote measurement values (\circ for $\Theta_A = 28^\circ$, $d_p = 0.7$ mm, \diamond for $\Theta_A = 25.1^\circ$, $d_p = 1.2$ mm) and solid lines represent model predictions

(Eq. (3.12)) is valid for Froude numbers less than 0.4.

6.2 Flight holdup

The holdup of the rectangular flight along the discharge point is given by Eqs. (3.26), (3.33), and (3.35) for all the three regions. Figure 6.5 shows the dependency of the flight position on the flight filling degree for different flight length ratios varying between 0 and

2.5. It depicts that as the discharge point rises; the mass of the material in the flight diminishes, and finally empties at a certain angle (δ_L) less than 180° . Increasing the tangential length of the flight leads to lift more material and shifts the final discharge angle to right, i.e. more close to 180° , which is clearly observed in the figure. At higher l_2/l_1 the change in filling degree is observed to be flat in the first two regions, however the bulk movement of the solids is observed in the third region, which designates nonuniform distribution of the solids. The radial flight with $l_2/l_1 = 0$ empties at an angle when the final discharge angle is equal to the kinetic angle of repose ($\delta_L = \gamma_L = 32.4^\circ$). The most suitable discharge characteristic can be expected from the flight length ratio of $l_2/l_1 = 1.0$ where the flight filling degree decreases almost linearly resulting in a homogeneous material distribution over the cross-section.

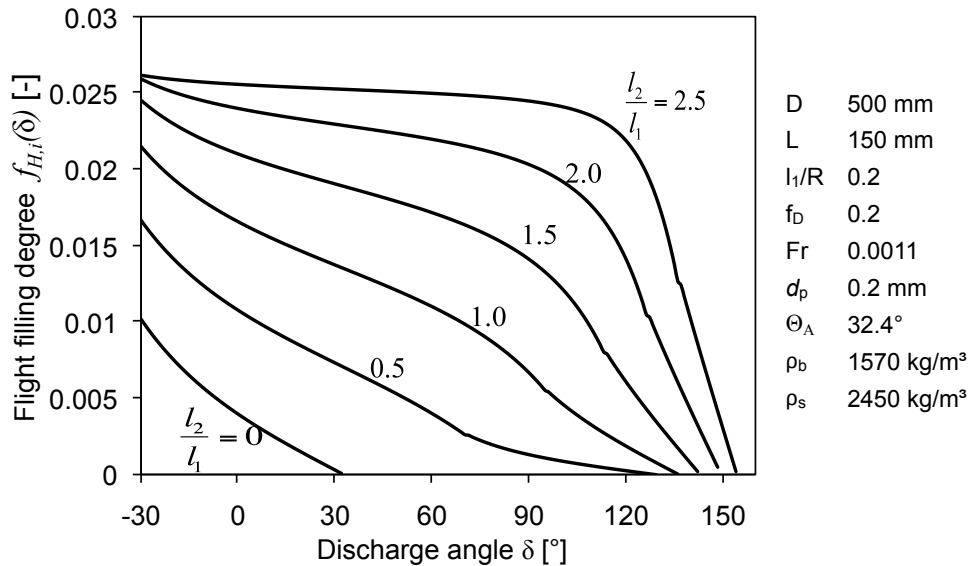


Figure 6.5: Flight filling degree in dependence on discharge angle for different flight length ratios, predicted for quartz sand

The total holdup of the active flights can be determined by studying the average dense phase holdup of the flights and the total number of active flights (see Eq. (3.36)). The influence of the flight length ratio was studied against the total holdup of the material in the active flights as shown in Fig. 6.6. As seen from the figure, the total dense phase of the flights increases as the ratio of the flight length increases. As expected the holdup also increases with increase in l_1/R .

The validation of the flight holdup at various flight length ratios for quartz sand has been shown in Fig. 6.7. The symbols in the figure represent the measured values and the

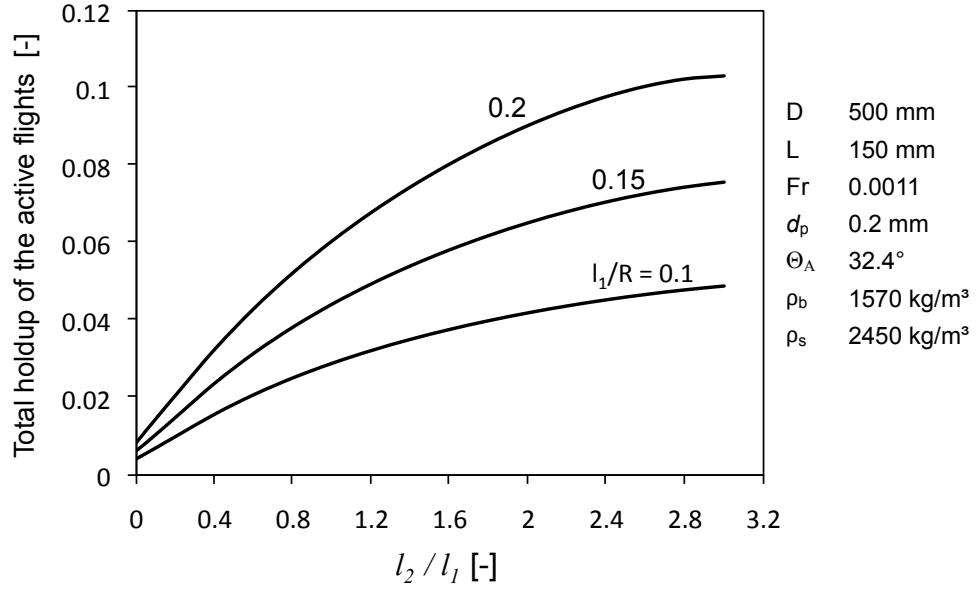


Figure 6.6: Total holdup ($f_{F,\Sigma}$) of the active flights in dependence on the flight length ratio, calculated for quartz sand

lines represent the predicted values of the corresponding l_2/l_1 . The measured values of the holdup were estimated by providing the measured kinetic angle to the model. This method had been chosen due to the complication involving the estimation of flight holdup along the discharge, when the drum is under operation. However, the measurements for all lifter types are above the predictions due to the higher measured values of angle of repose. At small l_2/l_1 , the flight holdup profile can be approximated to linear behavior. A single flight holds approximately 1.6% of the total volume when l_2/l_1 is 1.0, which is the maximum amount of material when the tip is at 9'o clock position ($\delta = 0^\circ$). Similar act is observed for glass beads when the experiments were performed by varying the drum size at 500 mm and 1000 mm which are presented in Figs. 6.8 and 6.9 respectively.

6.3 Flight cascading rate

The influence of the flight length ratio has been studied against the rate of material lost from the flight as a function of the flight position, which is illustrated in Fig. 6.10. It was calculated as the change in filling degree of the flight over the change in flight position which can be directly related to the cascading rate according to Eq. (3.42).

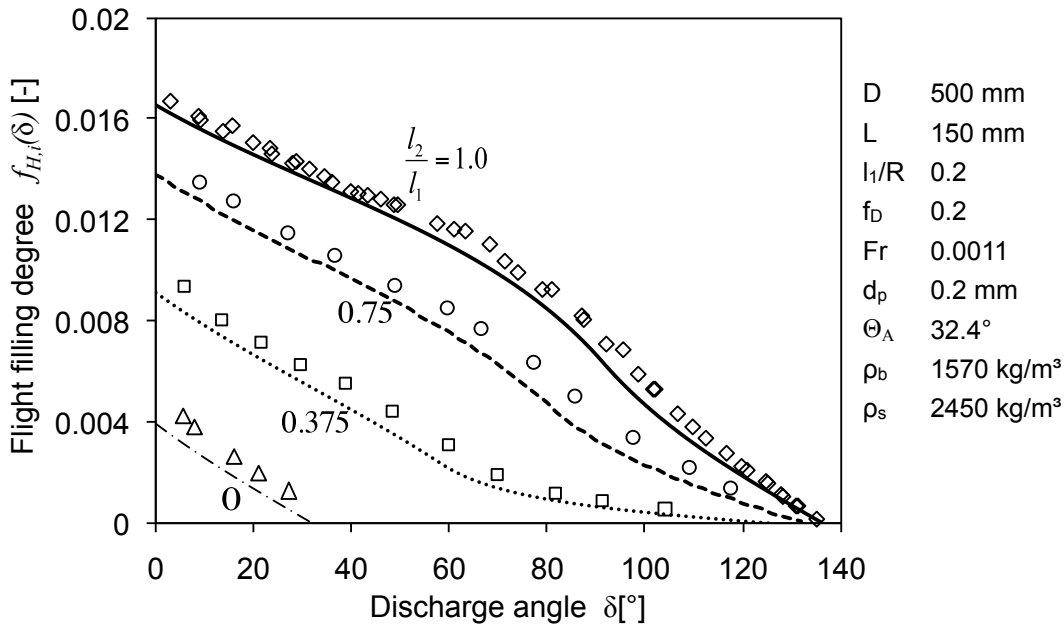


Figure 6.7: Experimental validation: Flight filling degree versus discharge angle at different l_2/l_1 ratios for quartz sand. Symbols denote measured values and the lines represent the model predictions

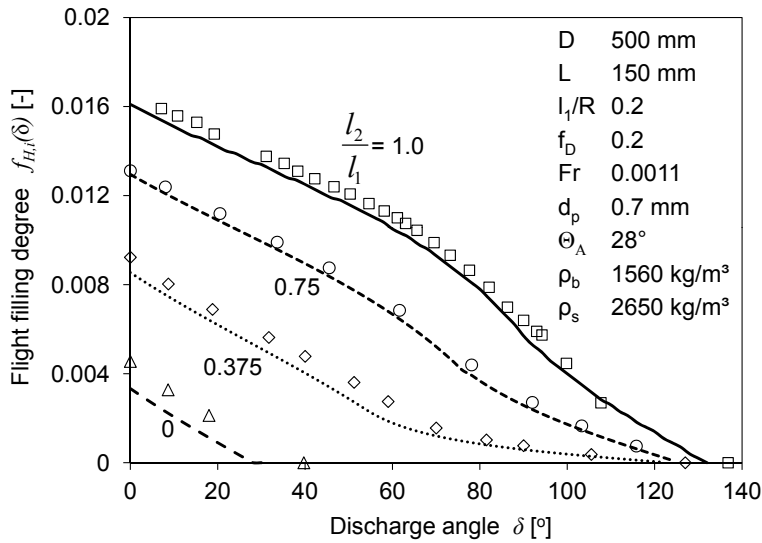


Figure 6.8: Experimental validation: Flight filling degree versus discharge angle at different l_2/l_1 ratios for glass beads. Symbols denote measured values of $D=500$ mm and the lines represent the model predictions

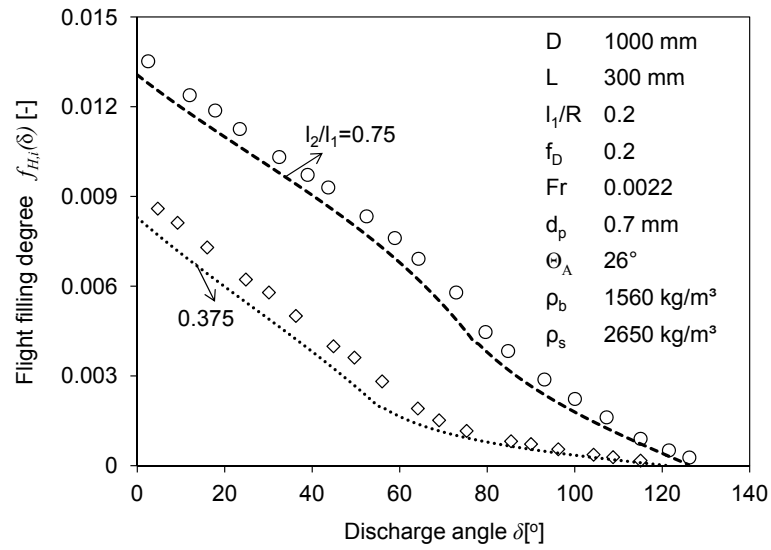


Figure 6.9: Experimental validation: Flight filling degree versus discharge angle at different l_2/l_1 ratios for glass beads. Symbols denote measured values of $D=1000$ mm and the lines represent the model predictions

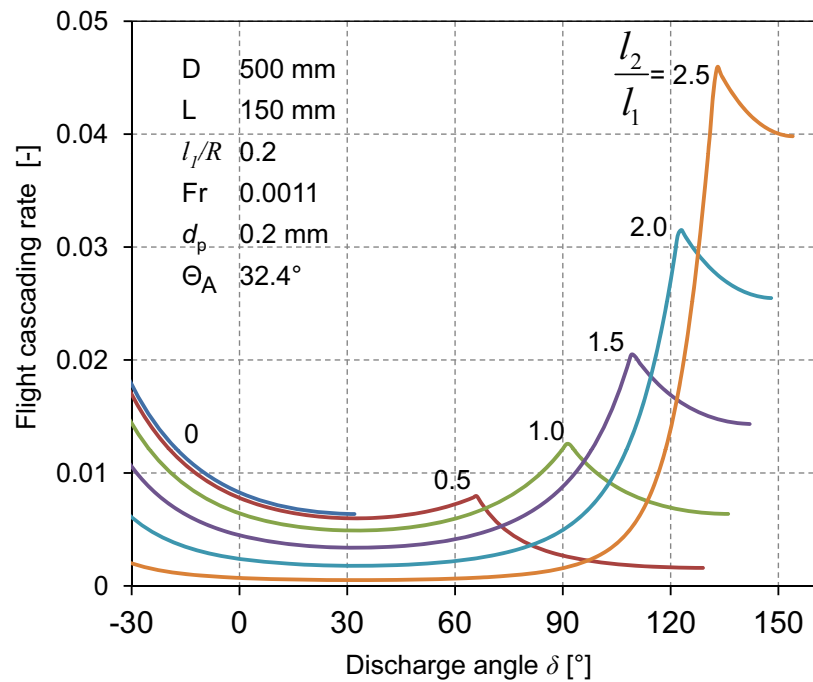


Figure 6.10: Flight cascading rate as a function of discharge angle at different l_2/l_1 ratios

It assumes that the flight is occupied to its maximum extent and starts discharging when the flight leaves the bed. As the figure depicts, the trend is not uniform over

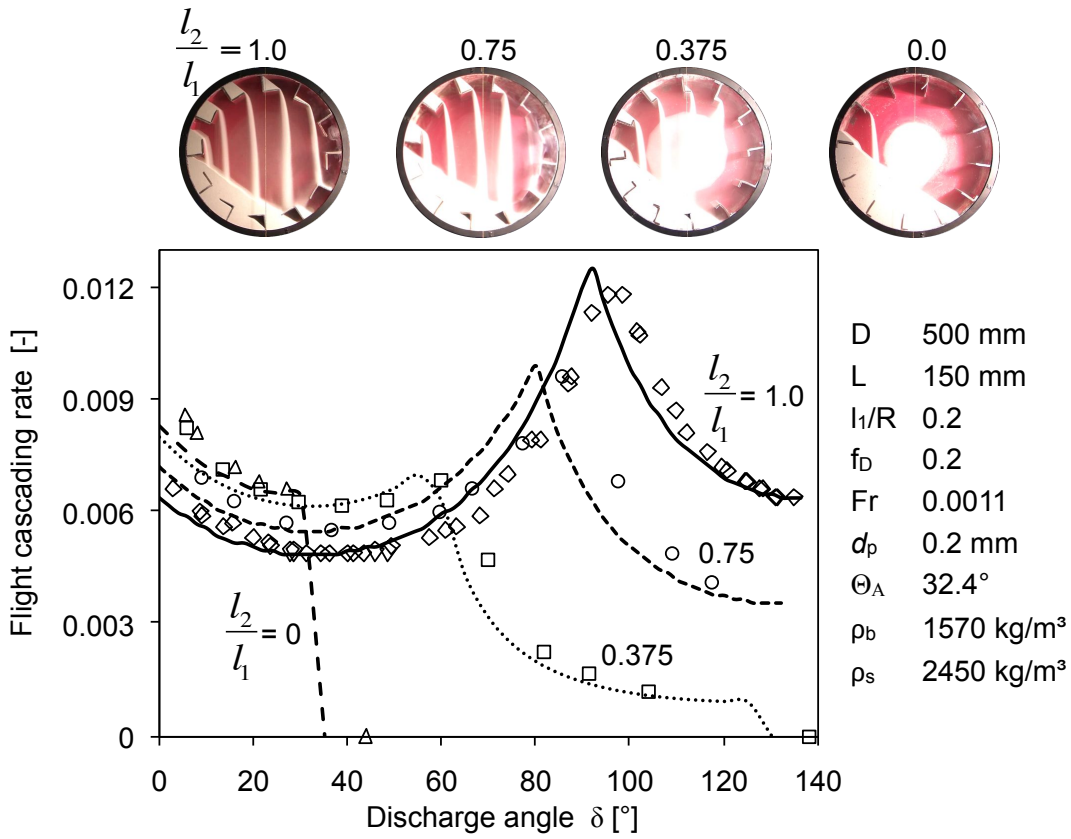


Figure 6.11: Experimental validation of Eq. (3.42): Flight cascading rate as a function of discharge angle at different l_2/l_1 ratios for quartz sand. Symbols represent measured values for quartz sand and the lines represent the model predictions

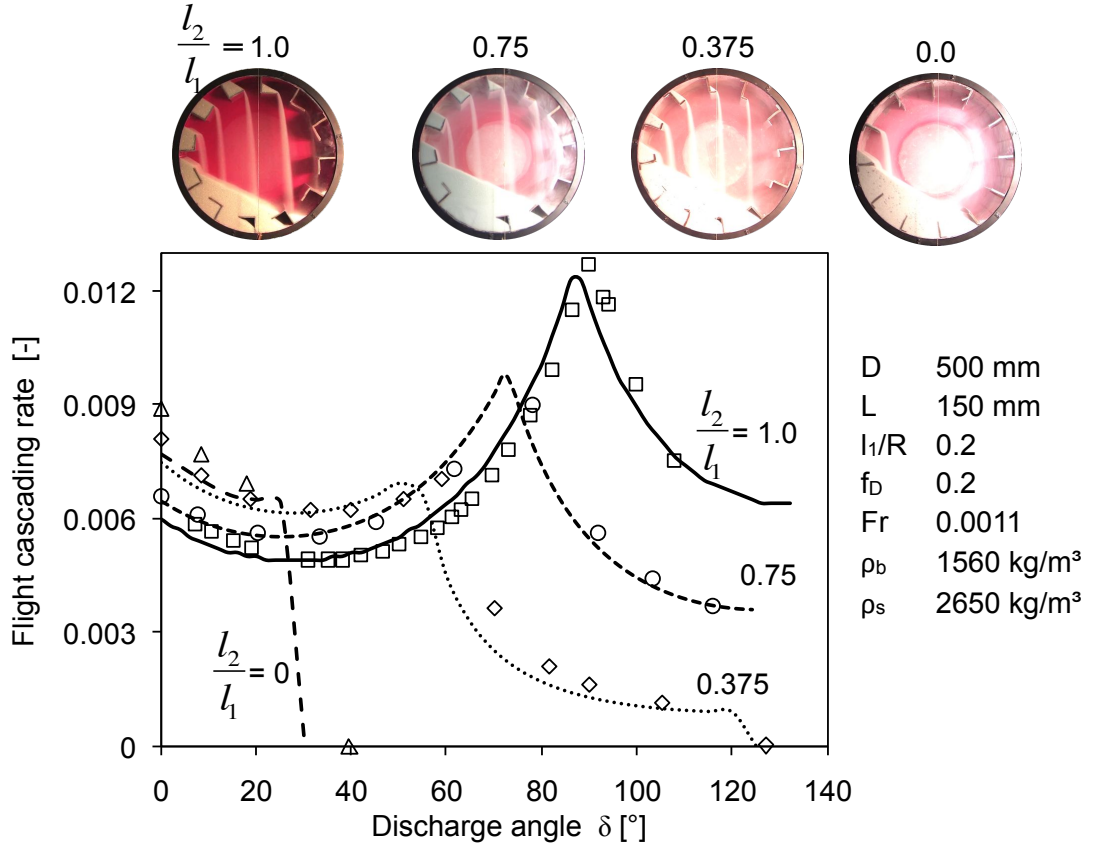


Figure 6.12: Experimental validation of Eq. (3.42): Flight cascading rate as a function of discharge angle at different l_2/l_1 ratios for glass beads. Open symbols denote measurements for $\square, \diamond, \triangle$ for $\Theta_A = 28^\circ, d_p = 0.7$ mm; \circ for $\Theta_A = 25.1^\circ, d_p = 1.2$ mm; when $D=500$ mm, $Fr=0.0011$), and the lines represent the model predictions

the discharge plotted for different flight profiles. The area under this curve depicts the amount of material distributed over the cross section of the drum. Local minima and maxima can be observed at the interfaces between 1st and 2nd region as well as 2nd and 3rd region respectively. The material from the flight initially trickles from large bulk quantities; therefore, the unloading rate is relatively high during the initial discharge. The cascading rate decreases until it attains a minimum at $(\delta = \gamma)$. After that, as the flight is elevated to higher discharge angles, the cascading rate increases and attains its maximum at $\delta = \gamma + \alpha + \beta$. This increase is caused by the phenomenon that the portion of bed material which is transferred from the static layer at the flight into the active flowing layer at the bed surface continuously increases. The mass flow rate is approximately proportional to the length of the bed surface line AE at the flight, see Fig. 3.5(a)-(c).

The length of the line AE reaches its maximum at the same position ($\delta = \gamma + \alpha + \beta$) when point A has approached point C [54, 90]. This is the transition between the second and the third zone. Later the cascading rate declines sharply until the emptying point of the flight. As the flight length ratio l_2/l_1 increases the flow rate also increases, but the rate of material loss during the initial discharge is observed to be poor. The sharp increase in the second region leads to poor performance of the dryers, due to the bulk movement of the solids developing a shielding effect of the neighboring particles. However, the initial rate of discharge is observed to be higher in case of the lower tangential lengths of the flight due to the less resistance offered by the tangential length.

The measured values of the holdup were used to evaluate the rate of change in filling degree. It is the change in the filling degree over the corresponding change in the discharge angle. The results are plotted against the discharge points of the flight as shown in Fig. 6.11. The lines in the plot represent the model predictions and the experimental values are depicted with symbols for quartz sand at different profiles of the flight. The trend of the measured points show good agreement with the model predictions. The three zones defined for the flight discharge can be clearly differentiated in the figure. Similar manner is observed for the glass beads as shown in Fig. 6.12.

6.4 Final discharge angle

The performance of the dryer mainly depends on the contact area and contact time between the gas and the solids. If the flight is under-loaded then the cascading of the flight starts at some angle much greater than zero and ends at some angle less than 180° . In addition to that, if the flight length ratio is small, then the final discharge occurs much lower than 180° . Under these conditions the drying operation can not be uniform, thus results the poor quality of the product. These aspects has motivated us to investigate the final discharge angle.

From Eq. (3.49) it is known that FDP is a direct function of Fr and flight dimensions and the kind of material. Figure 6.13 shows how the FDP varies with the Fr at different l_1/R values. It is almost constant until $Fr = 0.1$ but later a steep decrease in the curve has been observed at all l_1/R . It is also observed that increase in l_1/R , the final discharge angle switched towards right part of the drum. The plot depicts that the emptying angle falls as the Froude number increases. The curves for all l_1/R , asymptotically approach a value of 1.6 which is a critical Froude number ($Fr_c = 1/\sin(\Theta_A + \alpha)$) for the centrifugation of a single particle [11, 14].

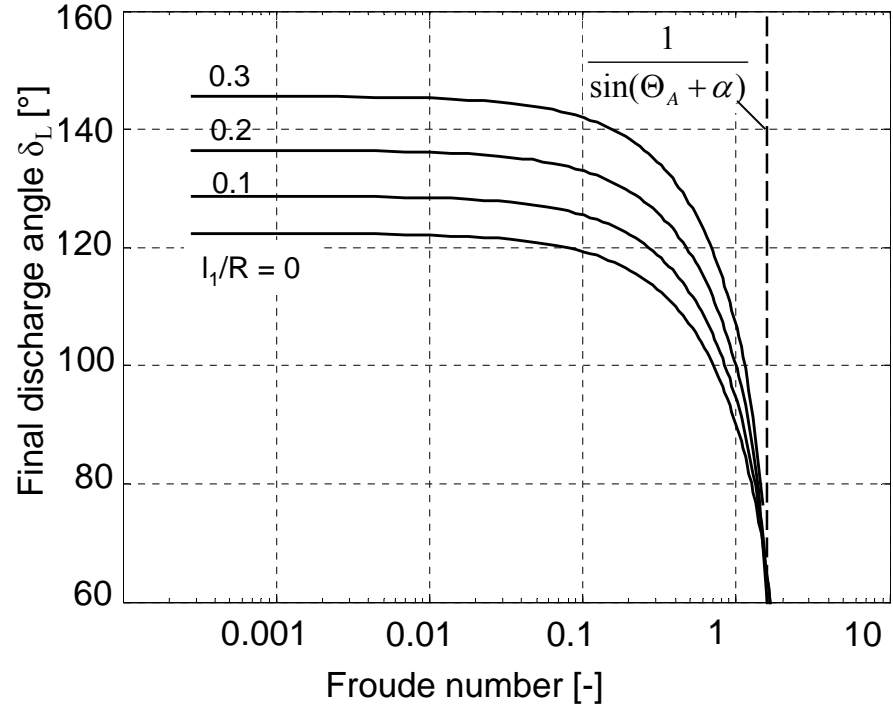
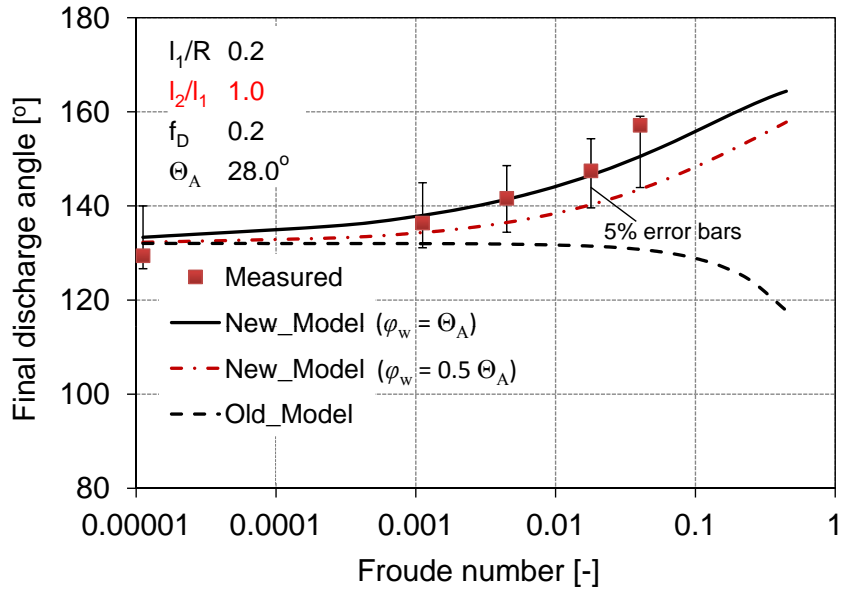
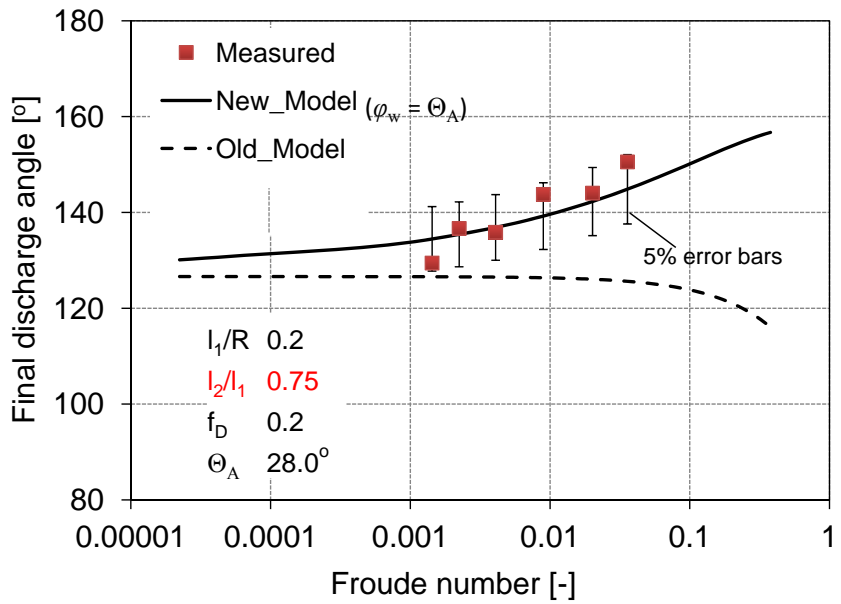


Figure 6.13: Influence of Froude number on final discharge angle

Figures 6.14 and 6.15 depict the validation of FDP of the flight as a function of Froude number at different flight length ratios. They illustrate the comparison between experimental data and the model predictions for glass beads. The experimental data had been measured by calculating the mean angle of last discharge of the flight from the images of several flights. The measured data illustrated late discharge of the flight while increasing the Froude number, whereas the Mellmann's FDP model depicted fast discharge on the other hand. Therefore, an attempt has been made in the present study such as presented in Section 3.6.2, to improve the model in order to understand the conflicting tendency of the measurements with Mellmann's FDP model. The simulations of the new model depicted similar tendency as compared to the experiments. Since μ_w is not available for these materials, as a initial study it was assumed to be equal to the coefficient of friction ($\mu_w = \mu = \tan \Theta_A$). The deviation between the predictions and the model increases while changing the wall friction angle to half of the dynamic angle as illustrated in Fig. 6.14(a). But in most cases the experimental data fall in the range of 5% error to the predicted data. However in the case of quartz sand as shown in Fig. 6.16, it takes little longer duration than that occurred for glass beads. Since glass beads are more uniform and slightly bigger in size than quartz sand, they become less cohesive as

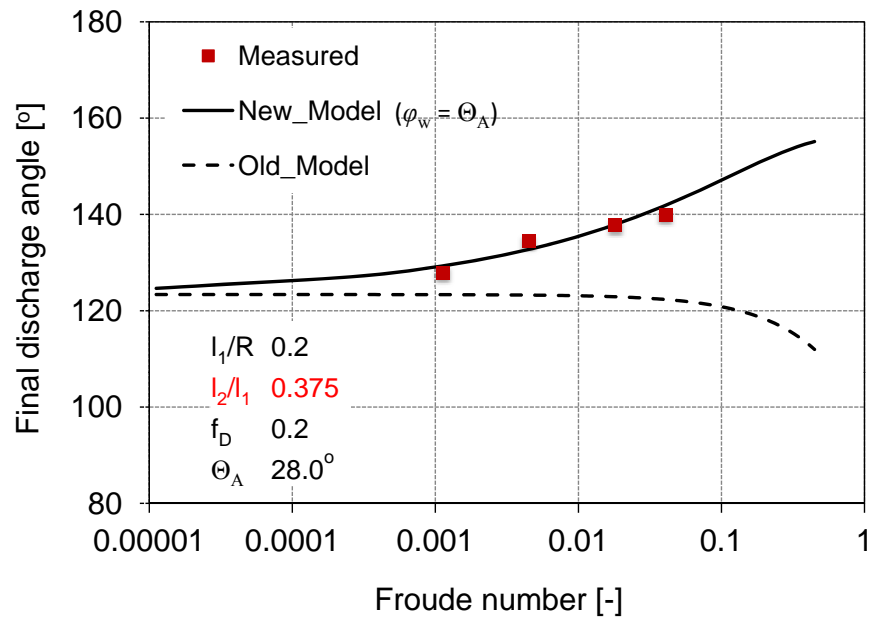


(a)

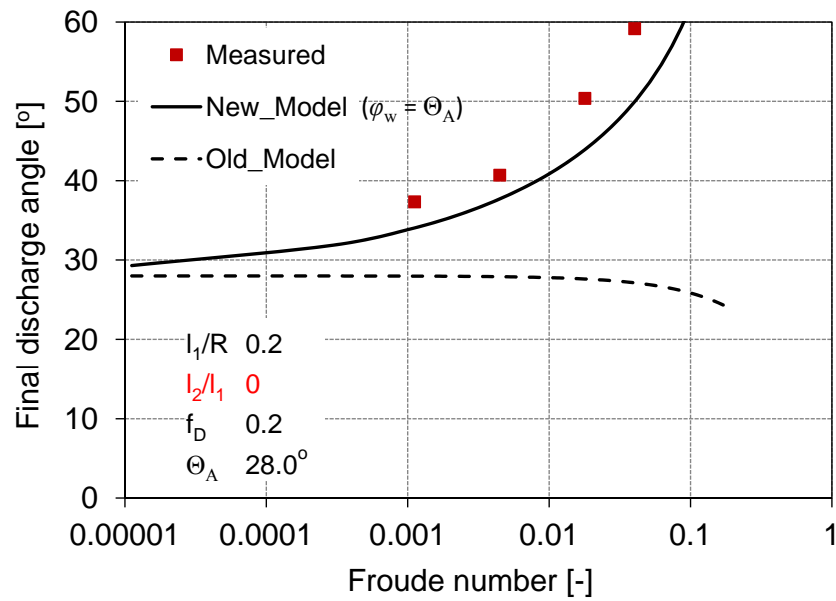


(b)

Figure 6.14: Variation of final discharge angle with Froude number for glass beads. a) $l_2/l_1 = 1.0$, $D = 500$ mm, b) $l_2/l_1 = 0.75$, $D = 1000$ mm



(a)



(b)

Figure 6.15: Variation of final discharge angle with Froude number for glass beads. a) $l_2/l_1 = 0.375$, $D = 500$ mm, b) $l_2/l_1 = 0$, $D = 500$ mm

a)

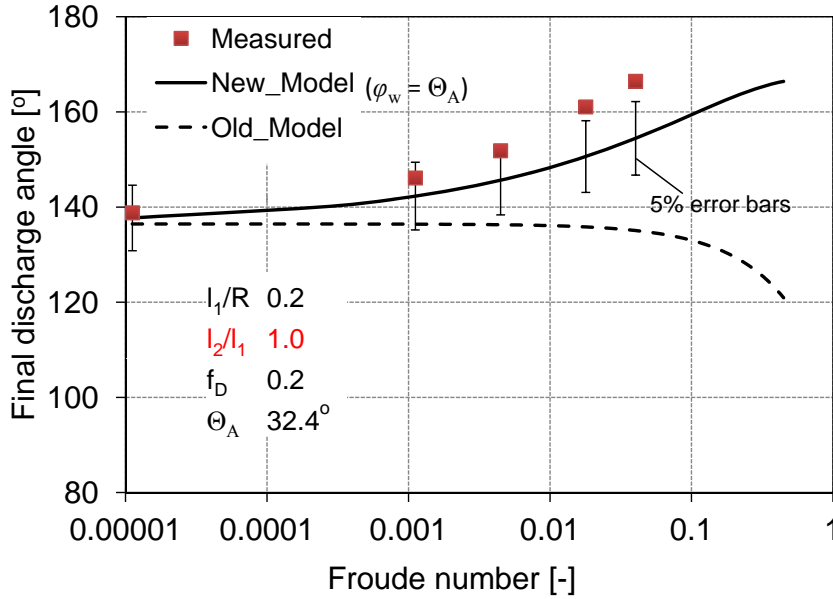


Figure 6.16: Variation of final discharge angle with Froude number for quartz sand ($D = 500$ mm, $l_1/R = 0.2$, $l_2/l_1 = 1.0$, $\Theta_A = 32.4^\circ$)

compared to quartz sand, which results in free flow of glass beads.

As could be demonstrated, the new model for FDP can now predict the similar tendency that has been observed from the measurements. This demonstrates that the bulk material at the flight should be considered as a diluted phase from a certain point of discharge, where the bed height has decreased to a certain value. Hence, it is necessary to consider the transition from the dense phase to diluted phase in the geometrical model. However, this transition point is still unknown and needs further investigation. Therefore, in the present study we used the old model to determine FDP for predicting the particle surface area.

6.5 Theoretical number of flights

The influence of the flight length ratio on the number of flights is presented in Fig. 6.17. It depicts that as increasing this ratio the theoretical number of flights allowed in a given drum dimensions decreases. The rate of decrease is observed to be high during the small ratios and low at higher ratios. One needs more theoretical number of flights at small l_1/R ratio for a given flight length ratio.

The comparison between the active flights and the theoretical number of flights are

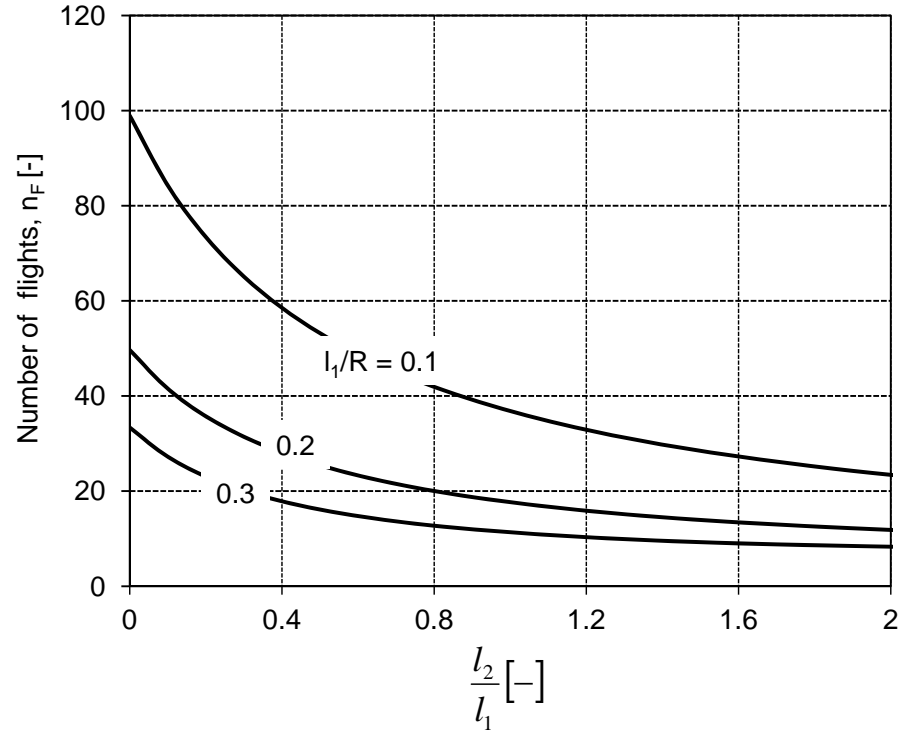


Figure 6.17: Influence of l_2/l_1 on the number of flights from Eq. (3.82) for quartz sand ($\Theta_A = 32.4^\circ$)

presented in Fig. 6.18. Primary axis in the figure represent the number of curtains to be formed in the drum for a known number of theoretical number of flights which is shown in secondary axis. As an example, the theoretical number of flights predicted for the drum are approximately 18 and the corresponding number of active flights are in between 6 or 7, when the length ratios of the flight is equal to 1.0. Experiments were performed

Table 6.1: Comparison of the active flights between model and the measurements

l_2/l_1	Model $n_{F,a}(n_F)$	Measurements	
		$n_{F,a}(n_F=12)$	$n_{F,a}(n_F=18)$
1.0	6-7 (18)	5	-
0.75	7-8 (21)	5	7
0.375	9-10 (28)	4-5	5-6
0	4-5 (50)	2	2

by operating the number of flights at 12 and 18 and the number of curtains formed

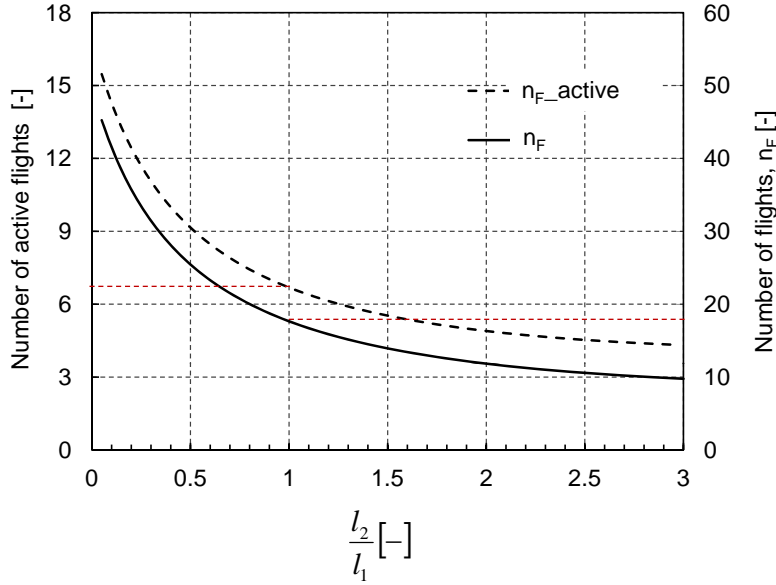


Figure 6.18: Comparison between active flights and the theoretical number of flights

during both the cases were presented in Table 6.1. The data had been presented for four different flight length ratios. For example, theoretically close to 6 flights are active out of 18 flights in the case of $l_2/l_1 = 1.0$ (Fig. 6.18). Whereas the measured data noticed 5 active flights when 12 flights were equipped to the drum. In case of $l_2/l_1 = 0.75$, both the model predictions and the measurements are approximately similar. In this case, the experiments were performed with 18 flights whereas the model predictions observed were 21 flights. It states that the drum can still be operated at less number of flights in order to produce the similar number of curtains. We still require more data from the experiments, in order to understand about the factor that can be reduced from the theoretical number to get same number of curtains.

6.6 Height of fall

Figure 6.19 shows the dimensionless height of the particles falling from the flight tip to the bottom of the drum as a function of the discharge angle. The present model was compared with the model from Blumberg and Schlünder [53], which does not account for the impact of the particles on the metal surface. The curtain height has been predicted for both the sectors of impact of the particles according to Eqs. (3.85) to (3.87). The model from Blumberg clearly over-predicted the real scenario as compared to our model

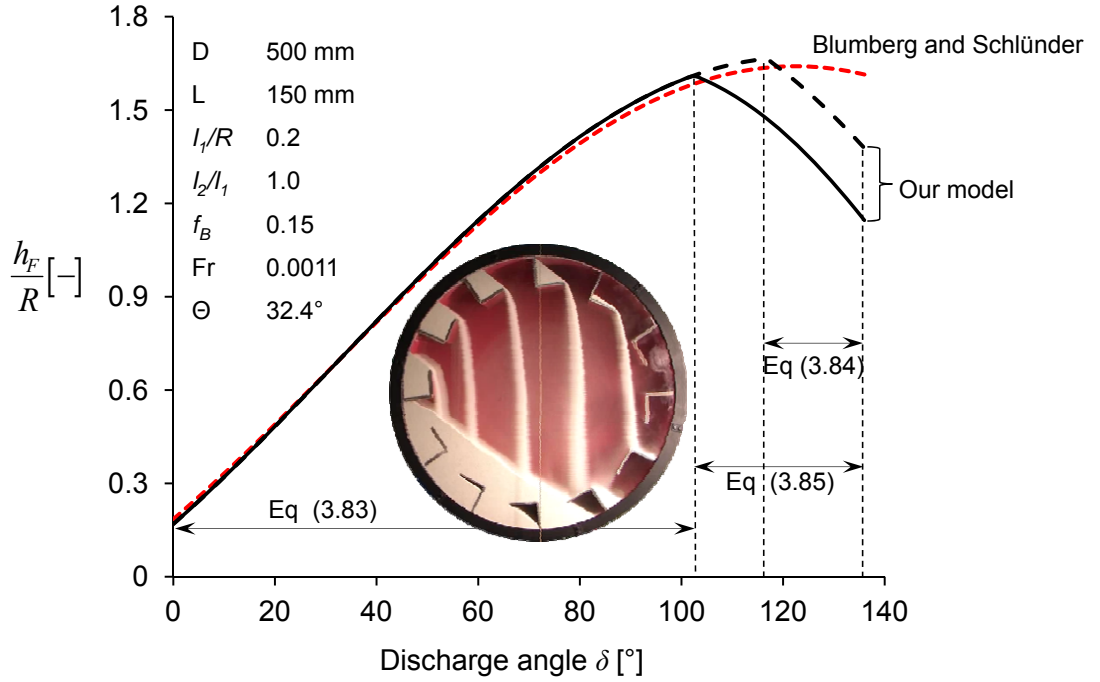


Figure 6.19: Dimensionless curtain height as a function of the discharge angle. Comparison between the present model (Eqs. (3.85) to (3.87)) with the model from Blumberg and Schlünder [53]

under over-loaded conditions. This over prediction of the curtain height by Blumberg's model is significant, since it suggests a greater heat transfer than is possible. The fall height increases until the end of the bed where the material has more time of exposure and then drops again. The smaller the bed filling degree the greater will be the height of the curtains.

The model was validated with the experiments at two different Froude numbers as illustrated in Fig. 6.20 for quartz sand. The symbols represent the measurements and the solid lines represent the model predictions. The measured values of the curtain height were calculated from the images of the recorded videos. They are in good agreement with the model in both sectors at small Froude numbers. As the drum speed and Froude number increased (Fig. 6.20(b)), the end point of the bed shifted to the left due to the decrease in bed filling degree. This is caused by more material carried away by the flights. The deviation can be attributed only for the fine material due to the change in trajectories of the curtains at high discharge rates (see Fig. 6.20(b)), which is not accounted in the model. However this deviation is not observed for glass beads even at

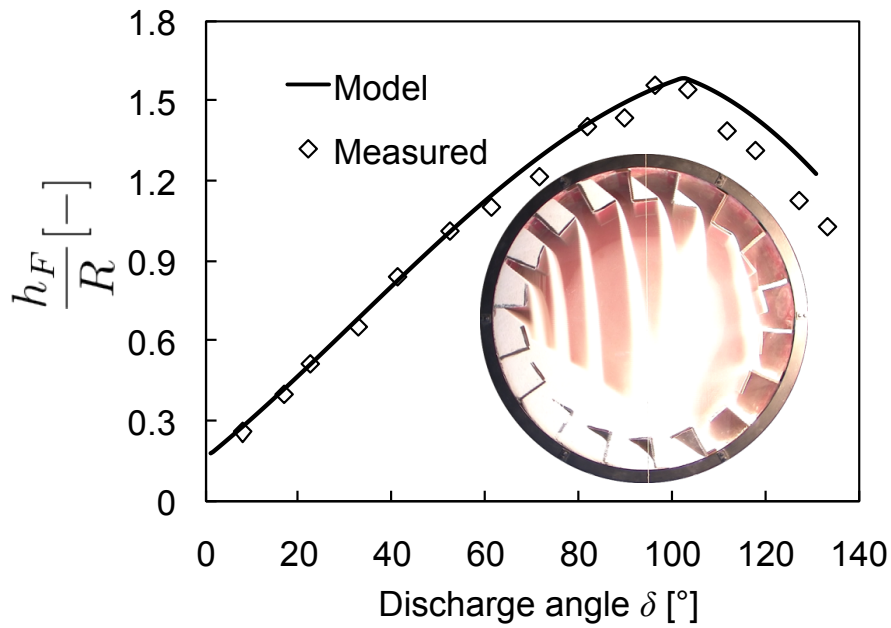
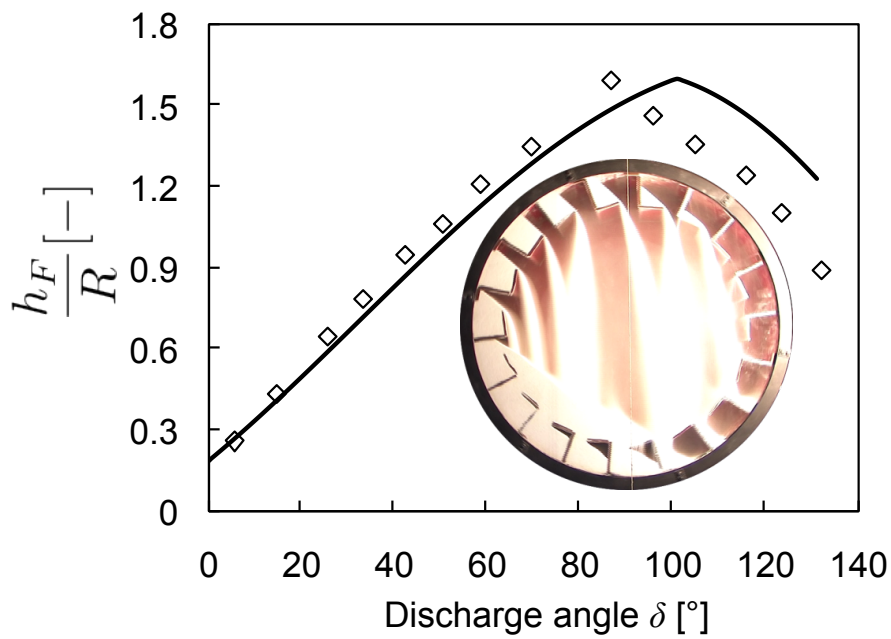
(a) $Fr=0.0011$ (b) $Fr=0.00447$

Figure 6.20: Comparison between the model predictions and the experimental results of the dimensionless height of the curtain for quartz sand ($D = 500$ mm, $l_2/l_1 = 0.75$, $l_1/R = 0.2$, $f_D = 0.2$, $n_F = 18$)

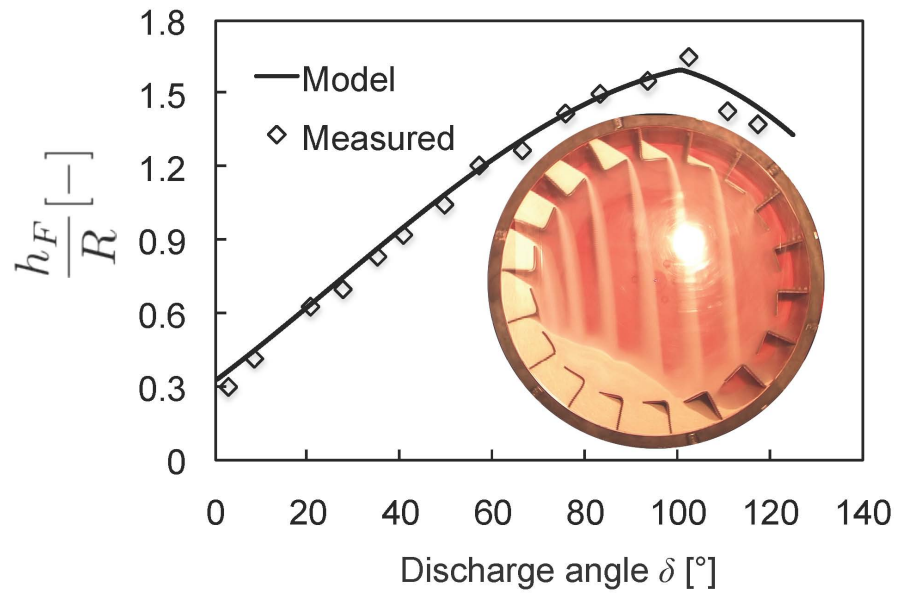
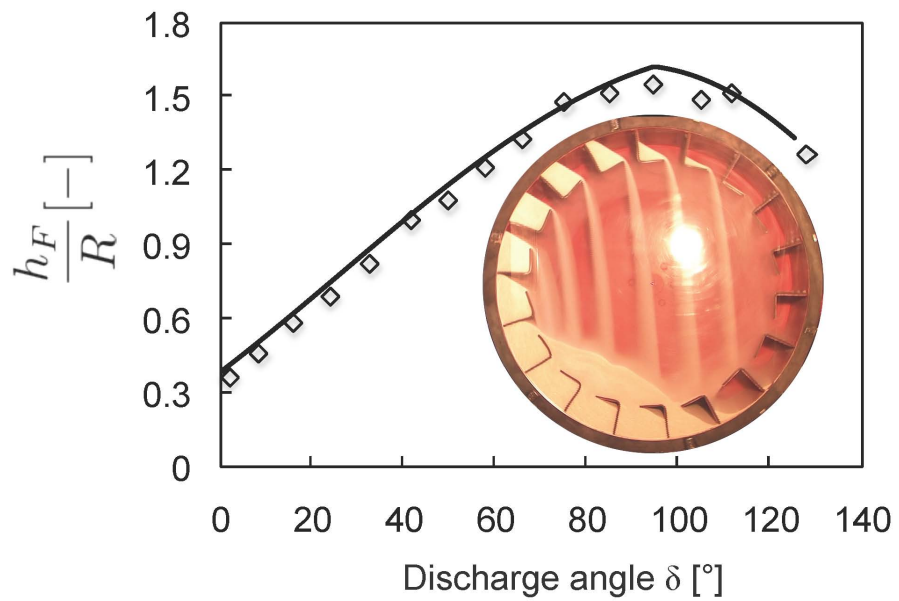
(a) $Fr=0.0014$ (b) $Fr=0.0041$

Figure 6.21: Comparison between the model predictions and the experimental results of the dimensionless height of the curtain for glass beads ($D = 1000$ mm, $l_2/l_1 = 0.75$, $l_1/R = 0.2$, $f_D = 0.2$, $n_F = 18$)

higher Froude numbers which is shown in Fig. 6.21.

6.7 Surface area of the falling particles

The exposed area of the particles is a strong function of the particle diameter and the bulk density of the particles as given in Eq. (3.97). The influence of Fr , and l_1/R on the contact area as a function of the flight length ratio (l_2/l_1) has been presented in Fig. 6.22. The total exposed area was found to be very small at small l_1/R ratios. For example, the maximum contact area was observed at $l_2/l_1 = 2.2$ in case of $l_1/R = 0.1$ and $Fr=0.001$, which is approximately 221 m^2 . Whereas, it was increased by four times when l_1/R is doubled at the same Froude number. This maximum area for this case was observed at $l_2/l_1 = 1.5$. Besides to that the contact area was increased only by 1.5 times although the Froude number has been increased to 0.01.

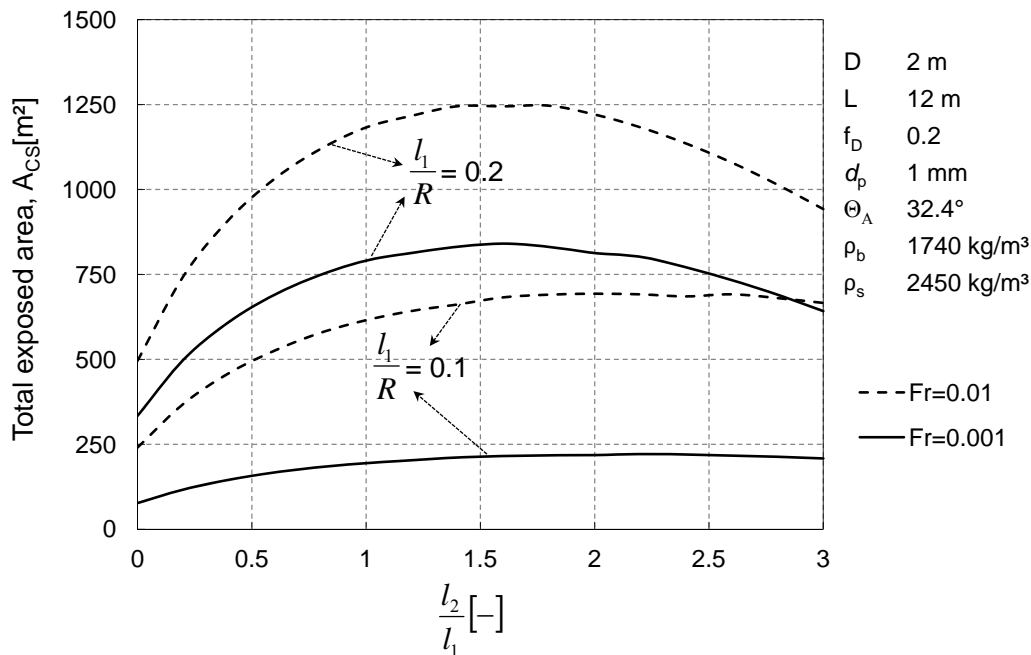


Figure 6.22: Influence of Froude number and flight length ratio on the surface area of the falling particles

Figure 6.23 illustrates the dependence of total contact area of the particles in the airborne phase on the flight length ratio. The total surface area of the particles increases until $l_2/l_1 = 1.5$ where it becomes maximum. Further increase in l_2/l_1 leads to increase in the mean cascading rates such as depicted in Fig. 6.10, but also decreases the num-

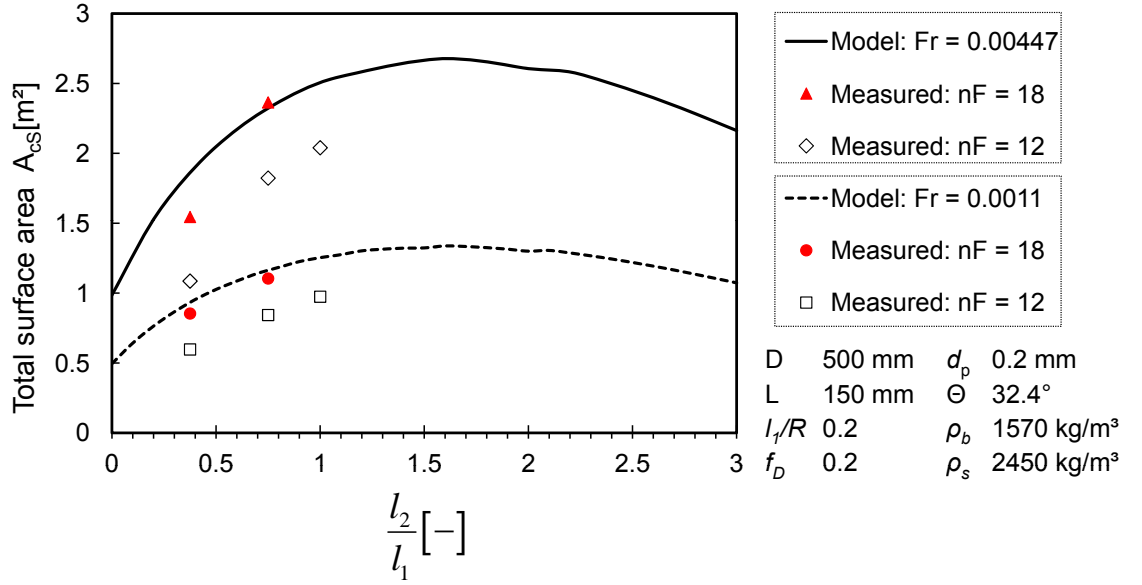


Figure 6.23: Total surface area of the particles in the curtains in dependence on l_2/l_1 calculated for quartz sand. Solid symbols denote for $n_F=18$ and open symbols for $n_F=12$

ber of curtains formed. The product of these two parameters attain local maximum at a particular flight length ratio as seen in the figure. However, during the low flight length ratios the slope of the curve is higher, but at higher flight length ratios (1-1.5) the change is almost insignificant. The figure also illustrates the experimental validation of the Eq. (3.98), at two different Froude numbers of three different flight profiles (l_2/l_1 at 1.0, 0.75, and 0.375). The solid symbols denote the data when the drum was allocated with 18 flights, the open symbols denote for 12 flights, whereas the corresponding model predictions were calculated for the theoretical number of flights. The data points were obtained by supplying the experimental data of the cascading rate and the height of the curtains to Eq. (3.95). Figure 6.23 clearly depicts that the total particle area increases by increasing l_2/l_1 with a small deviation between the experiments and the model predictions. However, the deviation becomes smaller when the number of flights approaches the theoretical number of flights. As the figure illustrates, the increase in Froude number also increases this area, due to increase in the holdup of the airborne phase whereas this will not be the case with the industrial drums. The increase in Fr or flight length ratio also increases the curtain density which leads to increase the shielding effect of the surrounding particles. This in turn results in poor contact between the solids and the hot gases, which is not considered in the model. Therefore, the influence of the gas flow further affects the optimal design of the flights which brings further down the estimated

factor of l_2/l_1 from 1.5.

6.8 Estimation of fractional filling degrees

For a given drum filling load, the fractional filling degrees of the different phases were predicted based on the model. The results for an over-loaded drum ($f_D = 0.2$) are shown in Fig. 6.24(a) where the fractional filling degrees are depicted over the flight length ratio. As can be seen from the graphs, the filling degree of the rolling bed f_B decreases as the flight length ratio increases. At the same time, the filling degree in the flights $f_{F,\Sigma}$ increases. For example at $l_2/l_1 = 1.0$, 68.6% of total material reside in the dense phase of the rolling bed, 30.2% in the active flights and the remaining 1.2% in the airborne phase. As the drum filling degree is reduced to half (Fig. 6.24(b)), the fraction of the airborne phase increased by approximately two times, while the fraction of the flight borne phase increased to about 60.4% and the fraction of the rolling bed was decreased to about 37%. However in this case, no change in the absolute amount of material in the flight borne phase is observed. This is due to the assumption that the flight is already crowded with enough material for unloading while it is in the upper half of the drum. The main limitation of the model is that it assumes the first unloading of the flight should start when the flight tip is at or below the horizontal axis, hence it can not be applied for under-loaded drums.

Table 6.2: Fractional filling degrees measured for $f_D = 0.2$ (see Fig. 6.24a)

l_2/l_1	n_F	Rolling bed f_B/f_D in [%]	Active flights $f_{F,\Sigma}/f_D$ in [%]	Airborne phase $f_{cs,\Sigma}/f_D$ in [%]
0.75	18	70.0 ± 1.4	26.4 ± 1.1	3.6 ± 0.83
0.375	18	82.3 ± 1.6	14.9 ± 1.8	2.8 ± 1.02
0	18	96.1 ± 0.4	3.6 ± 0.4	0.3 ± 0.1

The symbols shown in Fig. 6.24(a) corresponds to the filling degrees calculated from the cross sectional areas of the respective phases obtained from the images. For each flight length ratio, 10 images were collected and analyzed. The cross sectional areas of each phase were measured for all images except for the airborne phase. The filling degree was calculated by scaling this mean area with the drum cross sectional area. Using these measured data, the filling degree of the total airborne phase was calculated from

Eq. (3.102) for a known drum filling degree. For a drum filling degree of $f_D = 0.2$, the measured data of the fractional filling degrees are given in Table 6.2. It denotes that as the flight length ratio increases the bed filling degree decreases whereas the fractional filling degree of the airborne phase increases.

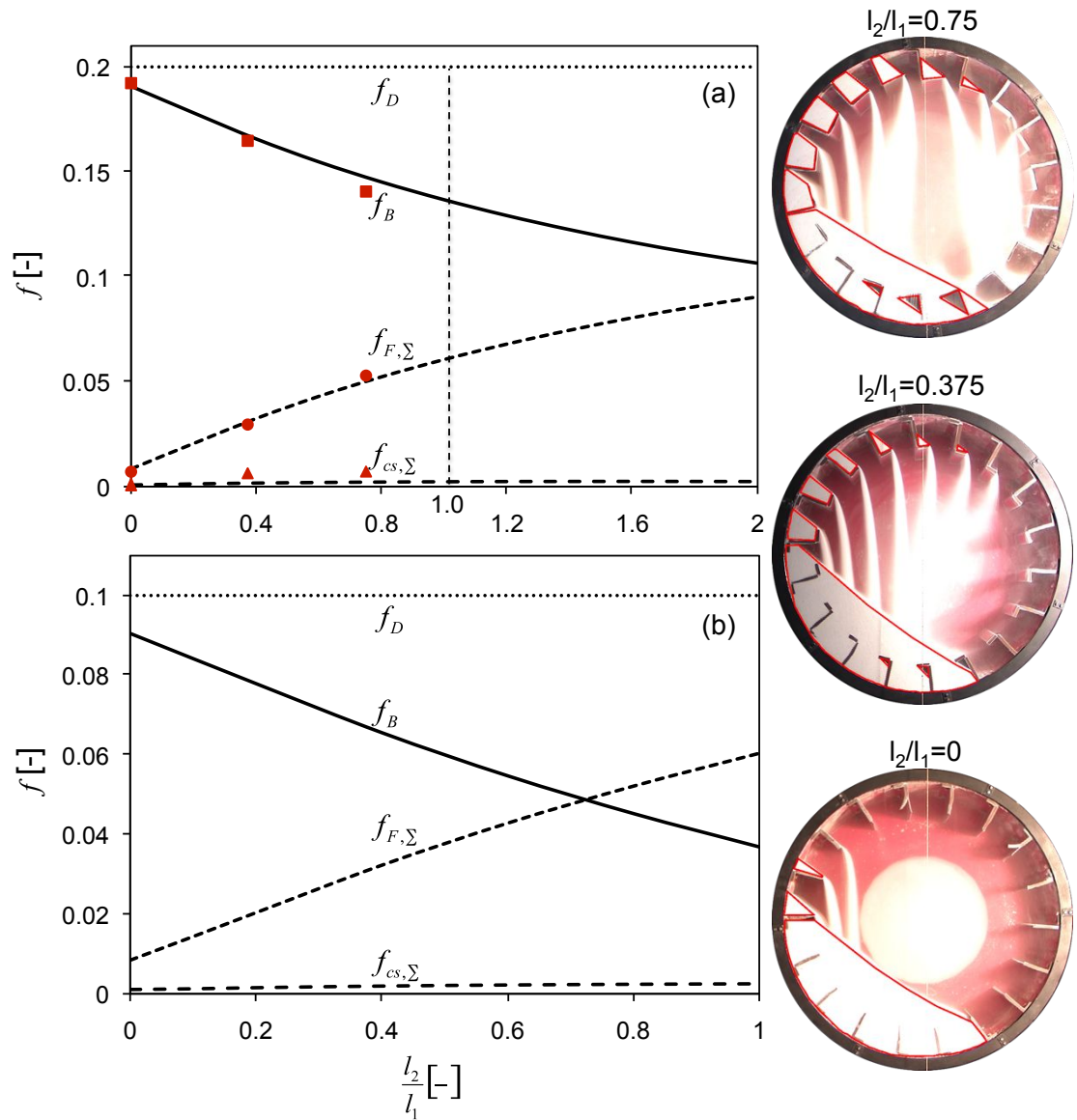


Figure 6.24: Effect of flight length ratio on fractional filling degrees ($l_1/R = 0.2$, $Fr=0.0011$, $\Theta_A = 32.4^\circ$). a) $f_D=0.2$, b) $f_D=0.1$

Chapter 7

Analysis and scale up

7.1 Analysis of experimental images

Influence of different parameters has been analyzed from the digital images of the experiments performed for different materials. The properties of these materials are listed in the Table 5.1. Experiments were performed at different filling degrees varying between 5-30% and the Froude number in between 0.0014 to 0.018. Each of these experiments were carried out by varying the number of flights at 12 and 18.

7.1.1 Number of rotations

Figure 7.1 shows the digital images collected from the recorded videos of the high definition camera. It illustrates the images of the drum filled up to 20% with glass beads and operated at different rotational speeds. The formation of the curtains and the unloading behavior of the flights can be clearly seen in this figure. A very thin layer of curtains were observed at very small Froude numbers as shown in Fig. 7.1 (a). This nature of the curtains is because of the small cascading rates at relatively small Froude numbers. This unwanted nature of the curtain can lead to higher particle entrainment. Since under practical applications, the drag applied by the gas on such curtains becomes more significant, as the drum is operated at relatively higher gas velocities. Further increasing the Froude number, the density of the curtains also increased simultaneously, which then reduces the entrainment of the solids. However, much higher Froude number leads to shielding of the particles due to higher curtain densities. Hence it is more important to operate the drum at optimal speeds in order to give better performance. Another important observation is that the emptying point of the flight was increased while the

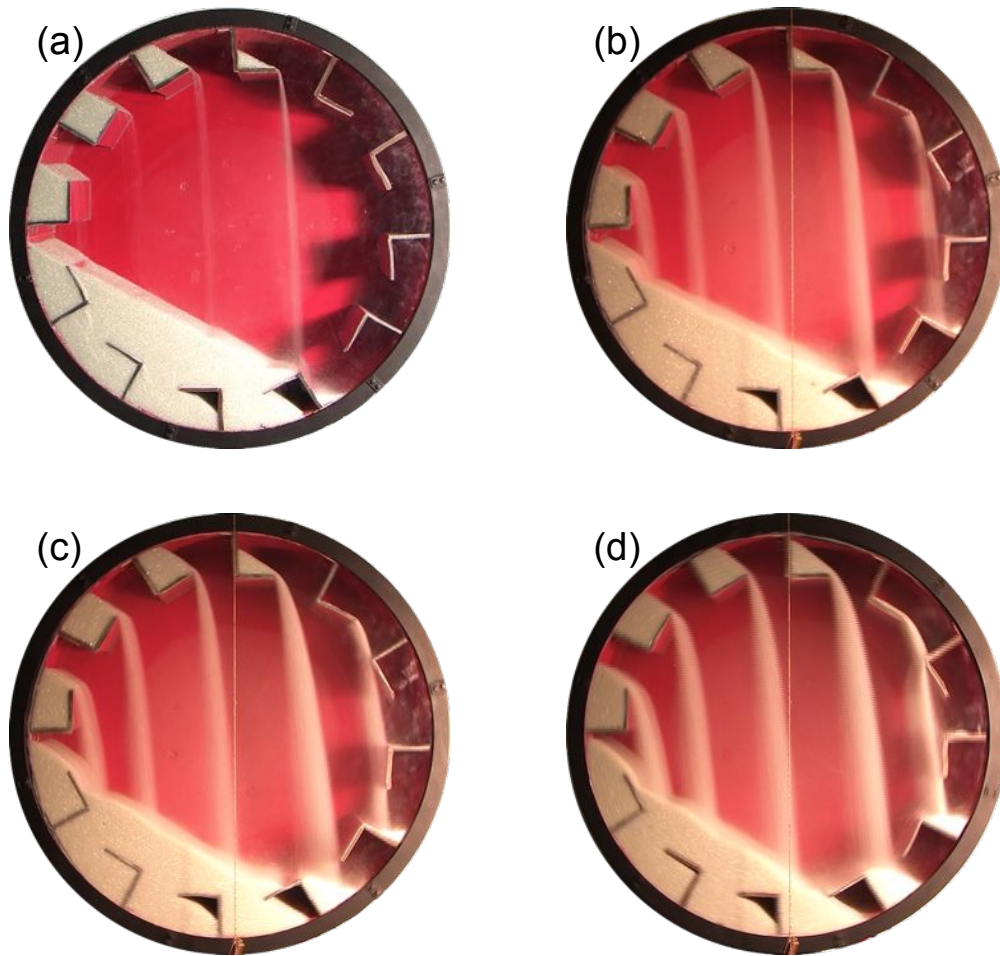


Figure 7.1: Experimental images of a 500 mm drum at different Froude numbers a) 0.000011 b) 0.0011 c) 0.00447 d) 0.0179. The drum is 20% filled with 0.7 mm glass beads and $l_2/l_1 = 1.0$

Froude number has been increased. Further the material at the end of the discharge, cascades on the neighboring flight sheet leading to form a secondary curtain as shown in Fig. 7.1 (c)-(d).

7.1.2 Filling degree

The rotary dryers operating at higher filling degrees offer poor performance due to less contact time between the gas and the solids. Figure 7.2 depicts the influence of filling degree by varying the amount of glass beads from 5% to 30% of the drum volume at a given Froude number. Figure 7.2 (a) clearly indicates that the filling degree of 5% is definitely under-crowded, since the unloading of the flight started at discharge angles

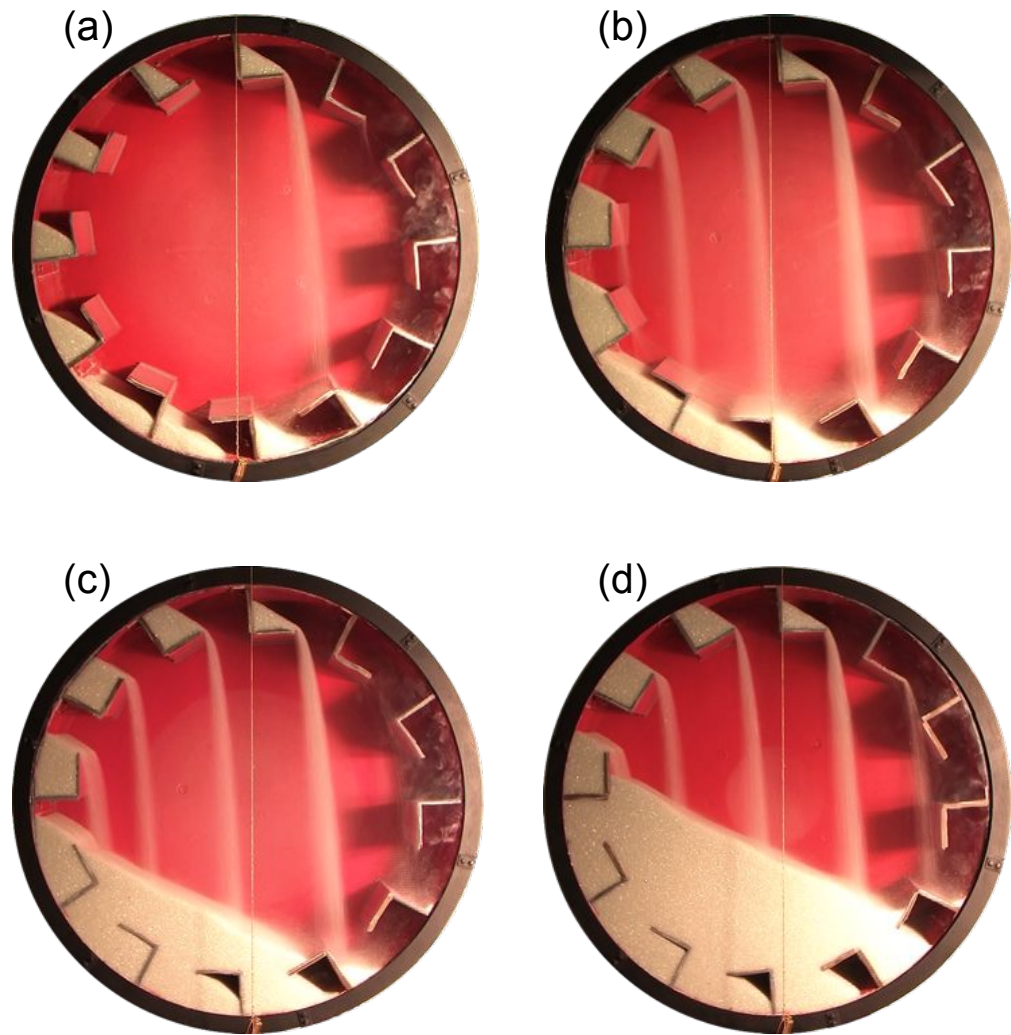


Figure 7.2: Experimental images of a 500 mm drum at different filling degrees filled with 0.7 mm glass beads a) 5% b) 10% c) 20% d) 30%. The drum is operated at $Fr=0.0011$ and $l_2/l_1 = 1.0$

above 90° yielding only one curtain. In Fig. 7.2 (b) the filling degree of the drum is doubled at the same Froude number, which then increased the series of curtains to be formed, however the starting point of discharge for this case is close to 0° . The particles in such curtains have higher exposure times to the hot gas due to lower bed heights and longer times of fall. Further increasing the filling degree to 20% (Fig. 7.2 (c)), the drum has become completely over-crowded, where the flight is being completely covered by the bed surface at the bottom. In this particular case, although the number of curtains increased by one than earlier, the total height of the curtains may have negative impact

on the contact time due to increase in the bed height. This can be more clearly observed in Fig. 7.2 (d), where the drum is 30% filled. The total height of all curtains formed in this case is definitely less than the previous case, hence leads to poor performance. Whence, the operating range of the filling degree for free flow materials should fall in the range of 10% and 15% to provide a better performance.

7.1.3 Number of flights

The influence of number of flights has been studied by varying the flight numbers at 12 and 18. Figure 7.3 illustrates the number of curtains formed when the drum was filled with quartz sand. It can be seen that only 5 curtains were noticed when 12 flights were fitted in the drum, whereas 7 curtains were observed for 18 flights. The increase in number of curtains increase the amount of material exposed to the hot gas, but also increases the flight borne phase simultaneously. Hence it results in a decrease of the filling degree of the rolling bed at the bottom which can lead to under-loaded case. Therefore enough care must be taken while operating the drum at higher flight number.

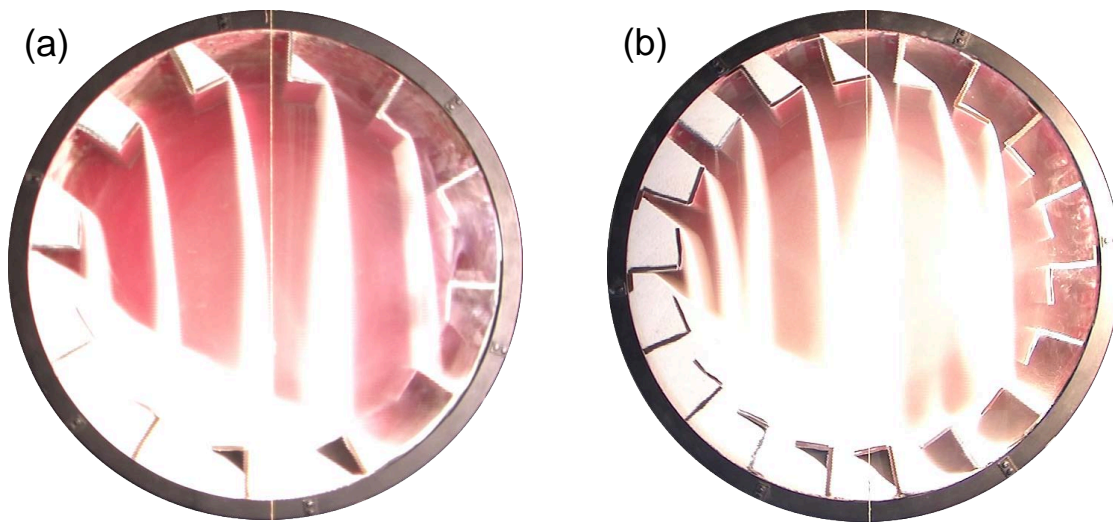


Figure 7.3: Experimental images comparing the formation of curtains operating at different number of flights (n_F) a) 12 b) 18. The drum is operated with 0.2 mm quartz sand at $Fr=0.0011$, $f_D=20\%$, and $l_2/l_1 = 0.75$

7.1.4 Flight length ratio

The experimental images of the series of curtain formation for quartz sand at different flight length ratios and two different Froude numbers were presented in Fig. 7.4. Fig-

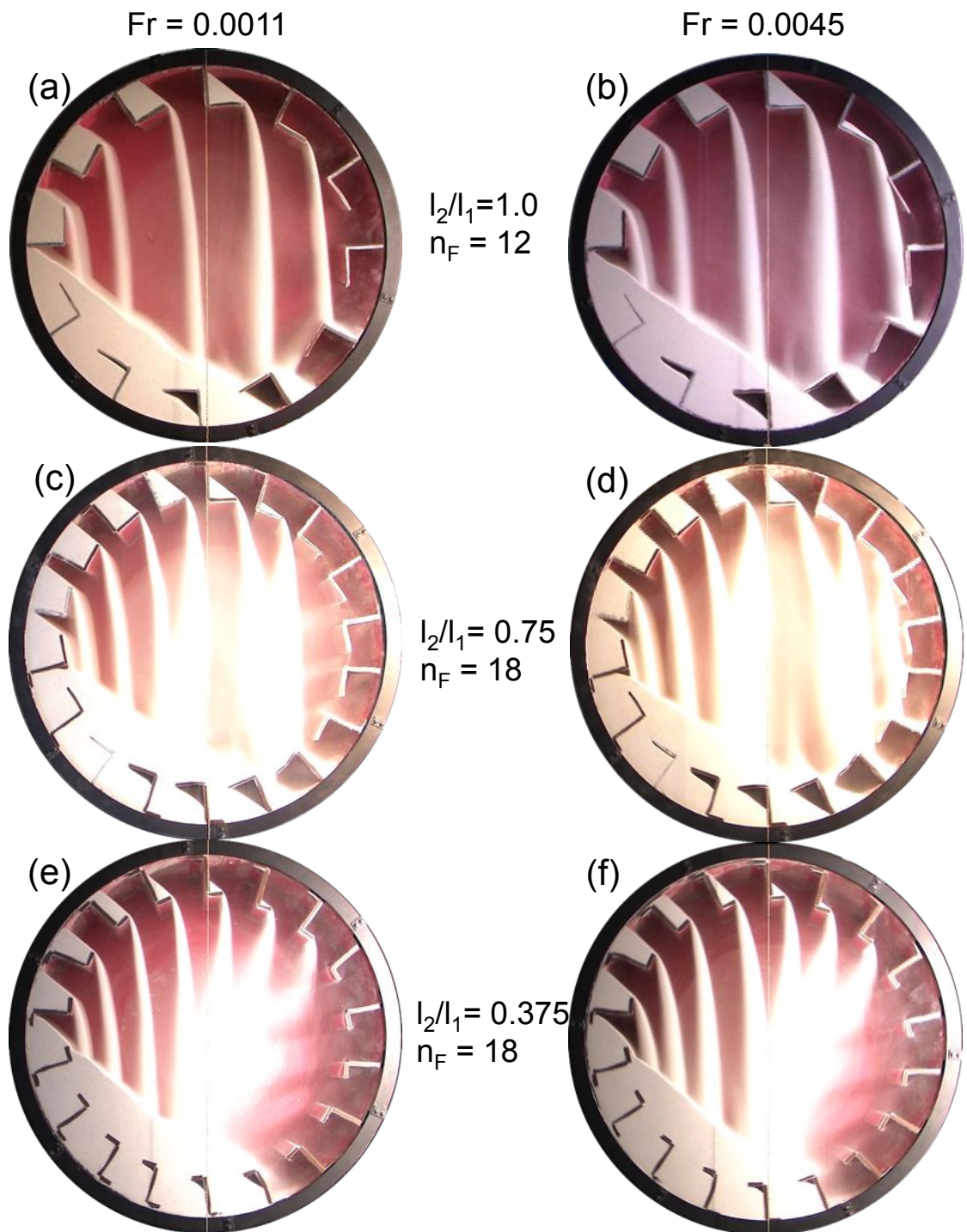


Figure 7.4: Experimental images of the drum at different flight length ratios ($f_D=20\%$)

ure 7.4 (a)-(b) depict the flight unloading process when 12 flights were equipped to the drum. The other images represent experiments with 18 flights. At a higher flight length ratio of $l_2/l_1 = 1.0$, the increase in Froude number did not show much influence on the uniformity of the curtains for a fine material. As the number of flights were elevated from 12 to 18, the number of falling curtains appropriately increased which were then increasingly influenced by the up-flowing air stream in the closed drum. This is due to the phenomenon that the more particles are falling down, the more gas is entrained by the solids flowing down with the curtains. As a result, the entrained air is recirculated upwards in counter current direction, thus influencing the falling curtains in turn. As can be seen from Figs. 7.4 (c)-(d), the up-flowing air cleaved through the falling curtains pushing them aside. Hence, individual air channels were formed between two certain curtains. From the experimental video it was observed that this happened after every third or fourth curtain. After the flight length ratio has been halved to 0.375, the up-flowing behavior of the entrained air changed, see Figs. 7.4 (e)-(f). Due to the lower flight length ratio, the emptying point of the flight is declined, in addition to that the cascading rates considerably reduced (Fig. 6.11). As a result, the up-flowing air stream was shifted to the right side of the drum where the particle concentration in the airborne phase was low. Similar manner as in Figs. 7.4 (c)-(d) can be observed as the drum size is increased to 1000 mm by operating at double the Froude number which is shown in Fig. 7.5. As can be expected, under practical conditions this vertical entrainment effect will interfere with the axial flow of the dry air, which has to be considered while designing the industrial dryer.

7.1.5 Influence of type of material

The formation of uniform curtains is mainly regulated by the behavior of the material, hardly no curtains can be observed when the material is highly cohesive. The granular nature of the material is controlled by the cohesive and adhesive forces. The influence of these forces becomes more significant when the moisture content of the material increases. Hence the formation of the curtains becomes difficult when the dryer is operated under these conditions, especially during the initial stage of drying.

In order to study the better design of the flights for such materials, experiments were performed with the drum filled up to 25% with limestone(Y14) at different flight profiles as shown in Fig. 7.6. Figure 7.6 (a) illustrates the behavior of the wet limestone when $l_2/l_1 = 1.0$. It was observed that this material does not have good flow behavior, hence

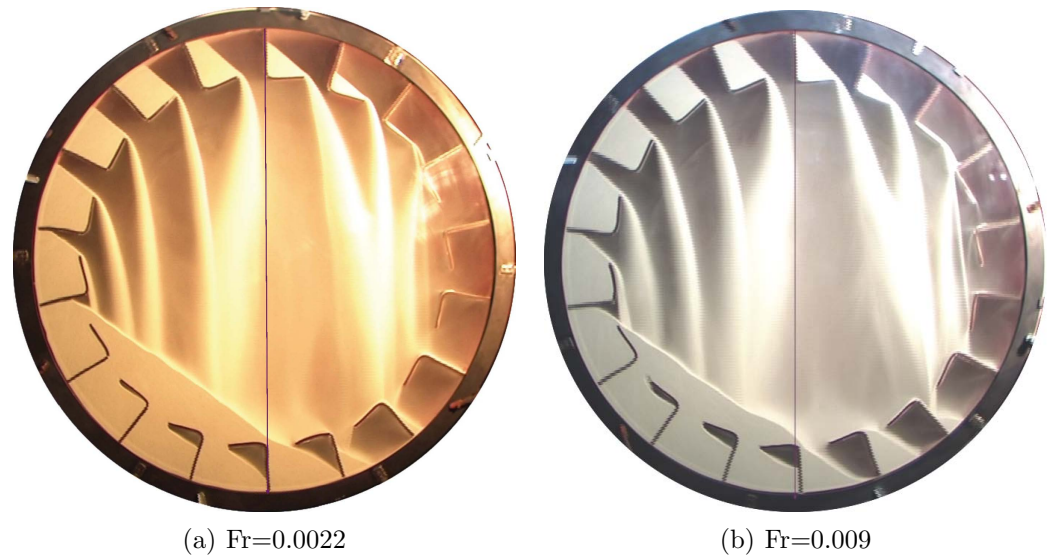


Figure 7.5: Experimental images of 1000 mm drum for quartz sand at different Froude numbers ($l_2/l_1 = 0.75$, $l_1/R = 0.2$, $f_D = 0.2$, $n_F = 18$)

no downfall of material was noticed in the free space of the drum and only clear deposits were observed at the adjacent flight sheets. As this study did not provide acceptable distribution of the material, the tangential length of the flight had been reduced to 0.75 of the radial length as shown in Fig. 7.6 (b). According to the model predictions, when the flight length ratio was decreased, the unloading rate of the flight was increased during the first two regions and emptied faster. However for a highly cohesive material, the emptying point is higher than for free flowing material. Fig. 7.6 (b) depicts the similar response showing a little improvement in flight unloading than the earlier case by forming partial curtains. Further reducing the tangential length, the frequency of formation of these discontinuous curtains had been improved, which is shown in Fig. 7.6 (c). In case of $l_2/l_1 = 0$, the material which is being carried from the solid bed into the flight cascades into the free space as a bulk. The contact time for this case is presumed to be small due to very small height of fall, hence this kind of profile is not a good suggestion for drying this type of material.

Figure 7.7 illustrates for the same material and similar conditions except the number of flights were operated in this case at 18. Figure 7.7 (a) indicates that no curtain formation was observed in case of $l_2/l_1 = 0.75$, and it was entirely sticking around the drum. However, a different behavior was noticed in Fig. 7.7 (b), where the frequency of material fall has been observed to be improved slightly. On the other hand, the material

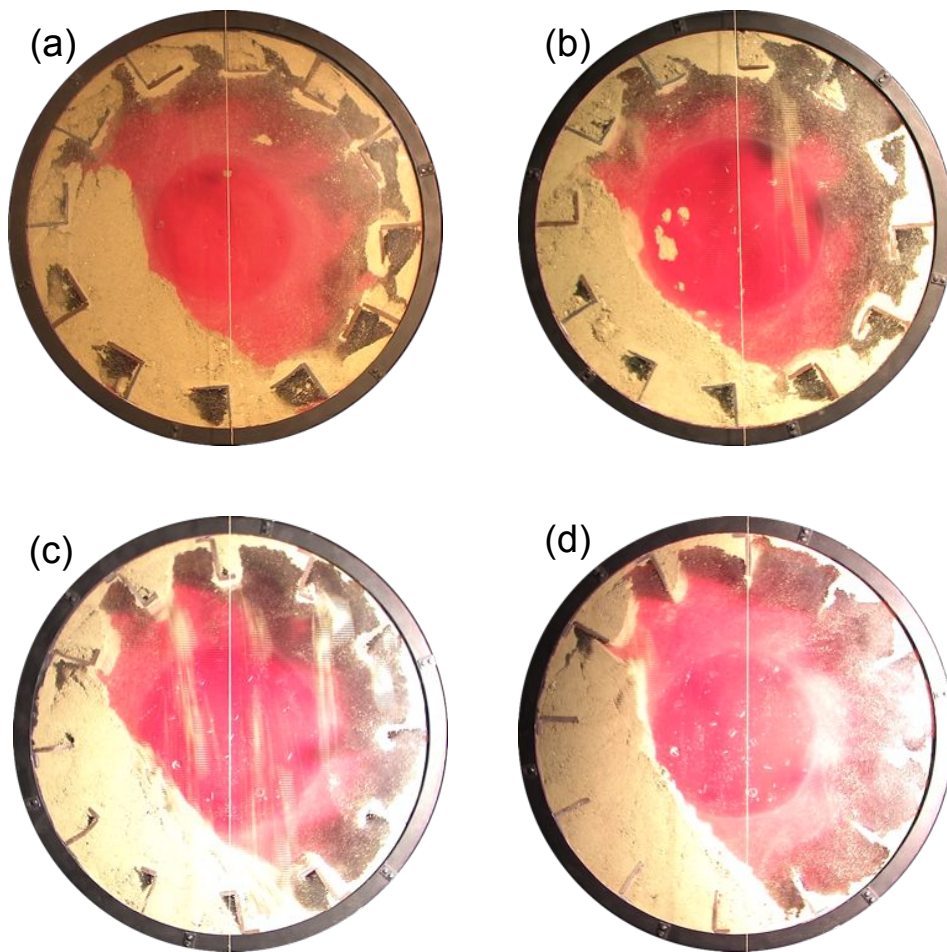


Figure 7.6: Digital images of the experiments representing the limestone(Y14) at different (l_2/l_1) flight profiles a) 1.0 b) 0.75 c) 0.375 d) 0. The drum ($D=500$ mm) is operated at $Fr=0.0011$, $f_D=25\%$, and $n_F=12$

was completely blocked between the flights and no downfall of the material from the flights was noticed in case of using radial flights (Fig. 7.7 (c)).

As this study did not provide any insight to define a proper design of the flight for the selected material (limestone(Y14)), which is due to the reason that the flowability index of this material is very poor. Therefore, in order to improve the flowability of this material, it was mixed with limestone(G5) in equal portions. Figure 7.8 depicts the motion behavior of this mixed probe filled up to 20%. The flow behavior of this material is improved slightly when compared with the earlier studies of limestone(Y14). However operating at higher number of flights as in Fig. 7.8 (b), the initial flight unloading was observed at higher discharge points as compared to the lower number of flights (see

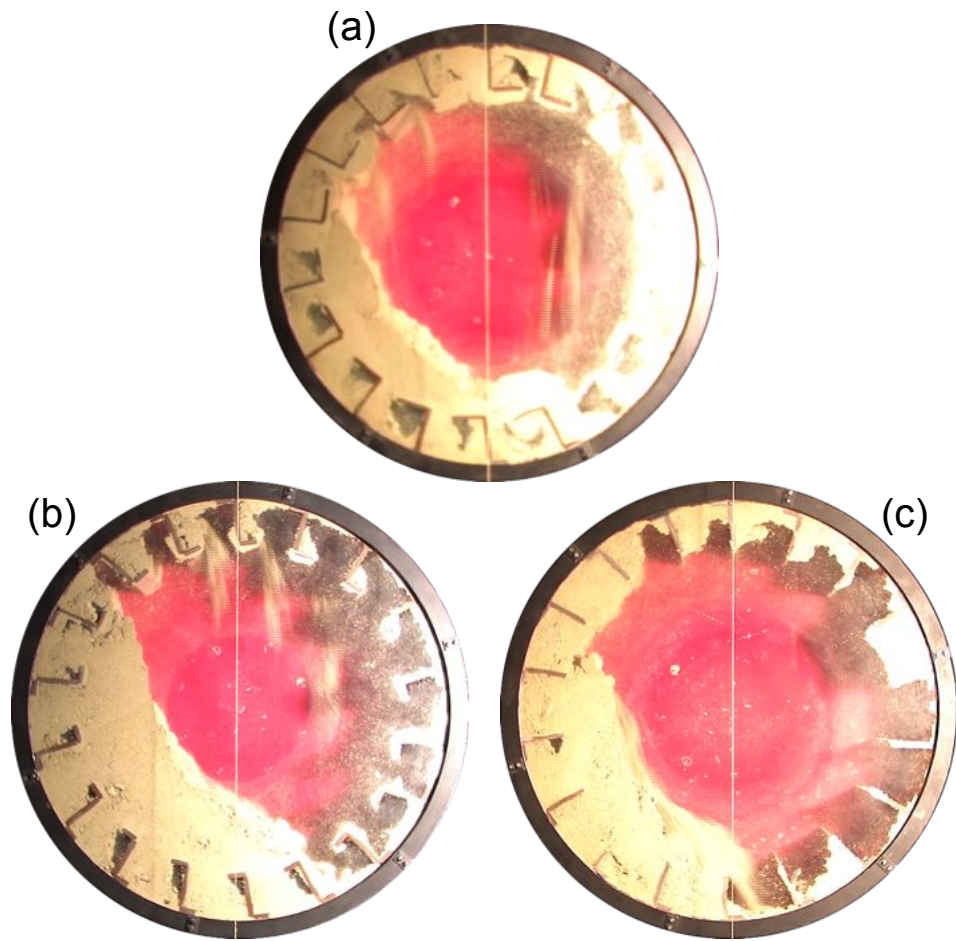


Figure 7.7: Digital images of the experiments representing the limestone(Y14) at different (l_2/l_1) flight profiles a) 0.75 b) 0.375 c) 0. The drum ($D=500$ mm) is operated at $Fr=0.0011$, $f_D=25\%$, and $n_F=18$

Fig. 7.8 (a)).

In order to study the influence of moisture content, now limestone(Y14) was completely dried and investigated the influence of flight length ratio as presented in Fig. 7.9. It is easy to understand from the figure that after complete drying, the flowability of the material had been increased drastically. Although it has better flowability, the flight unloading is not as continuous as for the glass beads and quartz sand. Further, the recirculation and fluidization behavior of the particles is even more pronounced in this case and hence more dust formation can be clearly observed. As the drum size was doubled and the flight number was increased (Fig. 7.9(d)-(f)) this entrainment action was further increased, hence it would become more complex for the gas to pass through the curtains.

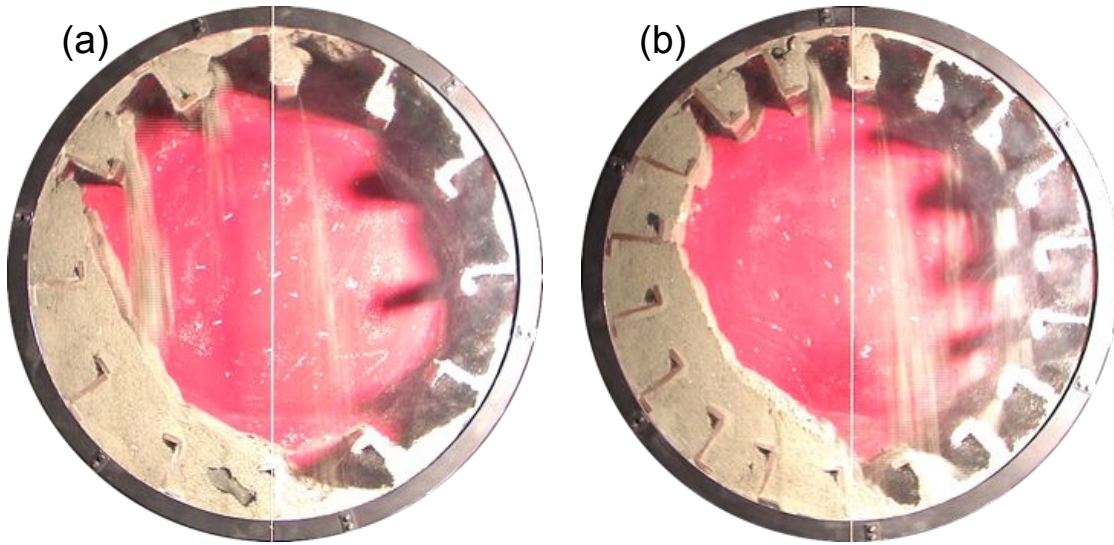


Figure 7.8: Digital images representing the motion behavior of limestone (G5+Y14). The drum is operated at $Fr=0.0014$, $f_D=20\%$, $l_2/l_1 = 0.375$. a) $n_F = 12$ b) $n_F = 18$

Therefore it is not a good advice to operate the drum always at higher flight number as it can lead to higher entrainment with this type of material. For such materials it is usual in the industries to operate the drum in counter current mode to avoid huge material loss with the gas stream.

Figure 7.10 illustrates the flow behavior of limestone(G2.5) filled up to 15% of total volume of the drum. The figure depicts the unloading process of the flight when number of flights were operated at 12 and 18. The flights are crowded with the material in case of Fig. 7.10 (a). Whereas it is noticed that the flight becomes under-loaded after increasing the number of flights at the same filling degree as shown in Fig. 7.10 (b). Due to more material resides in the active flights thereby reducing the bed filling fraction at the bottom. Consequently the flight unloading starts at discharge angles above 0° , due to insufficient amount of solids carried by the flight from the bottom of the drum. Small deposits of the material were also observed during the emptying of the flight on the adjacent flight sheets. Figure 7.10 (c)-(d) represent the same conditions except the flight length ratio is at 0.375. The flight becomes over crowded for the case shown in Fig. 7.10 (c) and becomes optimal loaded when the number of flights were increased (Fig. 7.10 (d)). The number of curtains formed in this case are 7 where as in Fig. 7.10 (b) only 6 curtains had been observed.

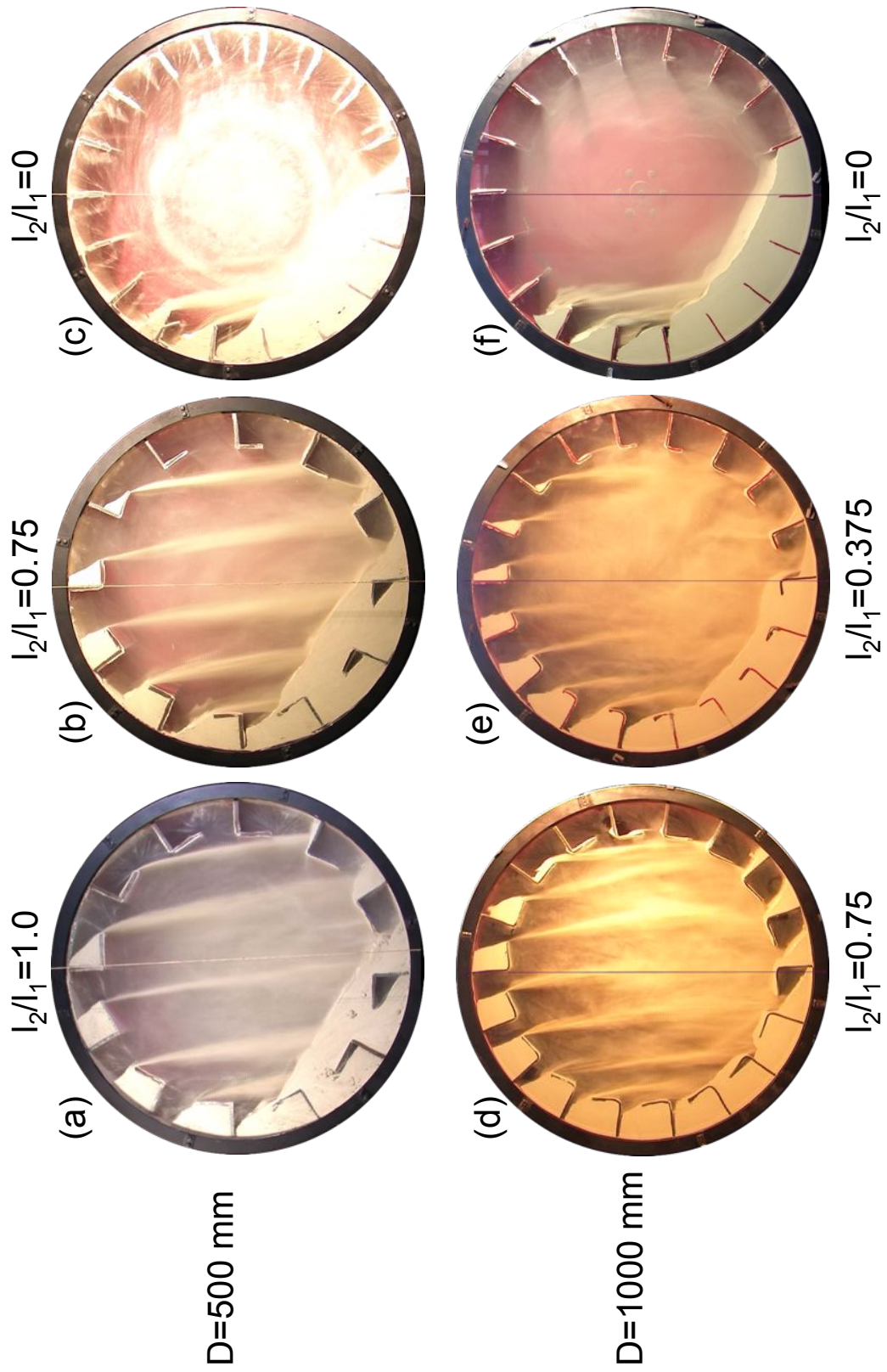


Figure 7.9: Experimental images of dry limestone comparing for two drums a,b) $n_F = 12$; c-f) $n_F = 18$. $f_D = 15\%$, $Fr = 0.0014$

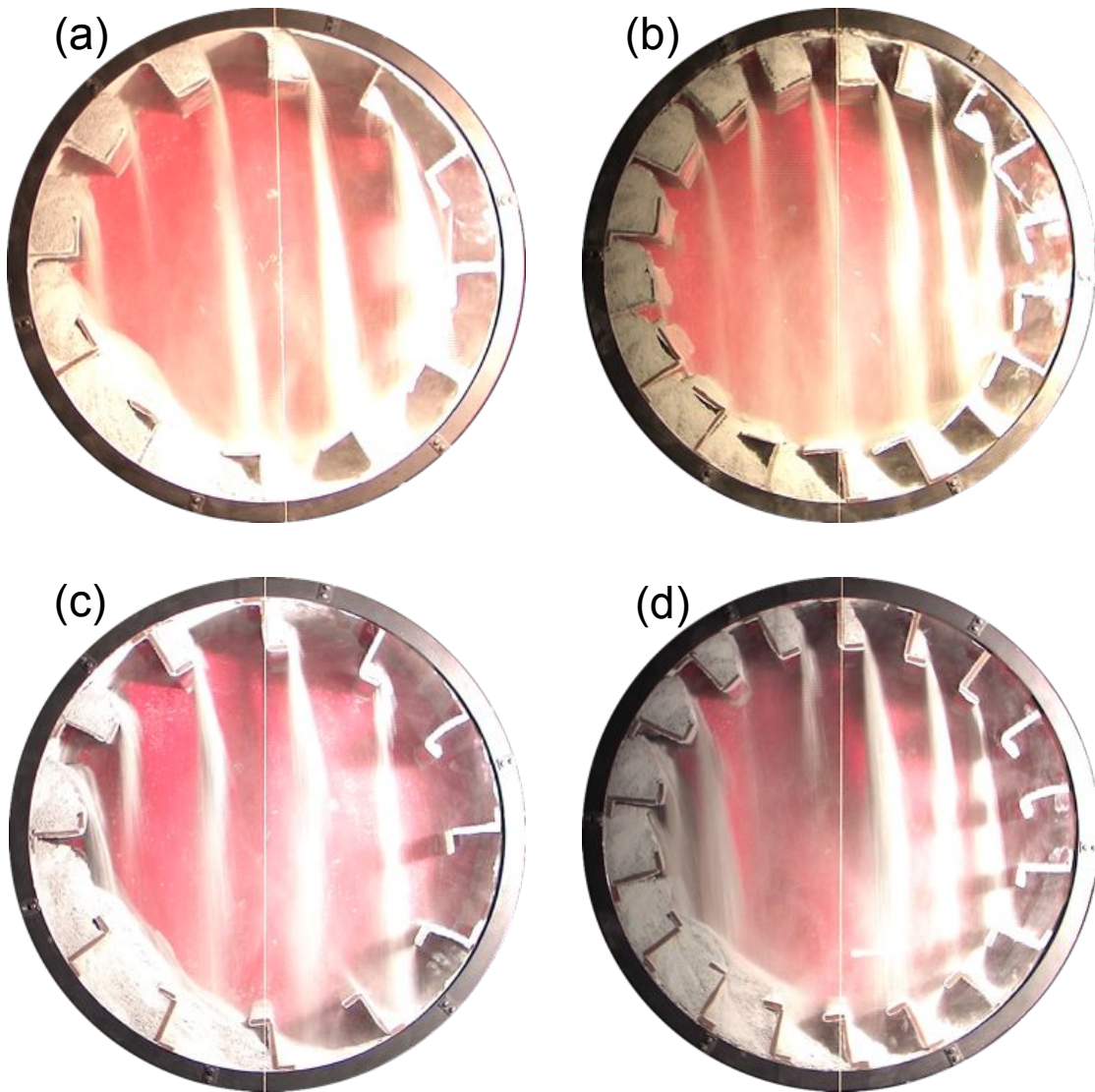


Figure 7.10: Comparison of limestone(G2.5) distribution at different (l_2/l_1) flight profiles
a) $l_2/l_1 = 0.75$, $n_F = 12$ b) $l_2/l_1 = 0.75$, $n_F = 18$ c) $l_2/l_1 = 0.375$, $n_F = 12$ d) $l_2/l_1 = 0.375$,
 $n_F = 18$. The drum is operated at $d_p = 2.5$ mm, $Fr=0.0014$, $f_D=15\%$

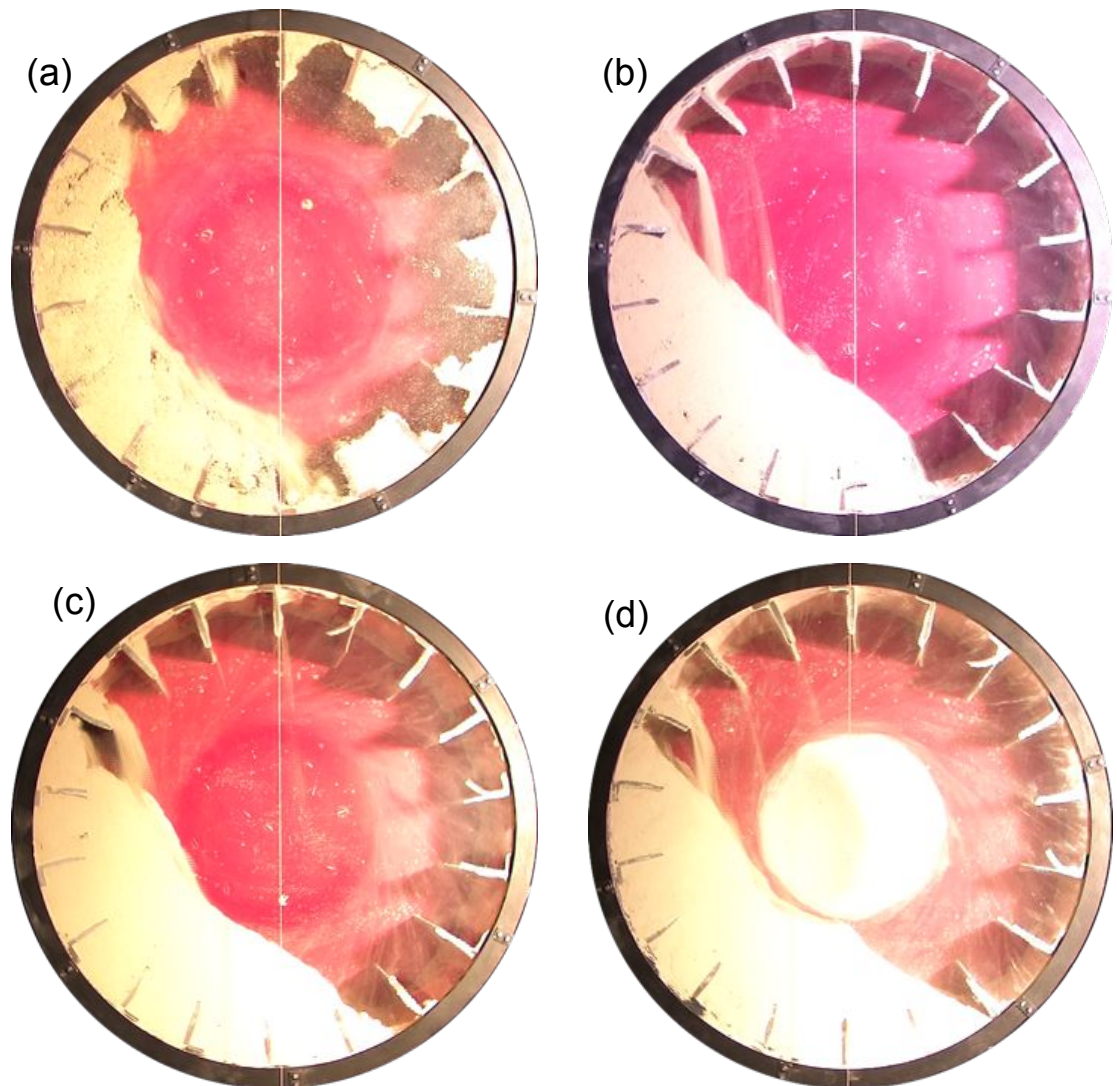


Figure 7.11: Digital images of the experiments representing the influence of moisture a) 14%, b) 7%, c) 3.5%, d) 0%. The drum ($D=500$ mm) is operated at $Fr=0.00147$, $f_D=25\%$, and $n_F=18$

7.1.6 Influence of moisture

The moisture levels change in the drum during the axial transportation of the material from the feed end to the discharge end. Therefore it is necessary to investigate the material distribution at different moisture levels. Figure 7.11(a)-(d) depicts the unloading process of radial flights at different moistures 14, 7, 3, and 0% respectively. According to the figure, as the moisture level decreases, the flowability of the material increases. The material has good free flowing conditions when it is completely dried. As the material

being dried, the angle of repose of the material varies along the drum length. Fine particles become more fluidized which can easily escape with the hot gas. This material can be recycled to the feed section again in order to improve the flowability of the bed material to be processed. With this approach the performance of the dryer can be enhanced.

7.2 Scale up to real dimensions

The experimental drum of 0.5 m is now scaled up to the industrial drum of 3.35 m in diameter and 6.1 m in length. In the industrial dryers the flights can be offset for some specific distance. The l_1/R ratio is maintained approximately around 0.2. In the present study the length of the flight is considered to be same as the length of the dryer. The effect of parameters such as Froude number, filling degree, dynamic angle of repose, and the length ratio of the flights has been investigated and presented in the following sections.

7.2.1 Froude number

The effect of Froude number has been studied for flight holdup, unloading rate, and the total contact area by varying it between 0.0018 - 0.0075, while keeping the other parameters constant. Figure 7.12 represents the influence of Froude number on the holdup of flight as a function of discharge angle. It shows that no significant variation has been observed in the quantity of material carried by the flight while changing the Froude number. The figure shows that a single flight carries an amount of approximately 1.23 tons of material. Therefore the thickness of the drum and the flight has to be considered while designing the drum that can handle the strain developed due to handling such bulk quantity of the material. The dependency of discharge rate of the flight over the discharge angle at various Froude numbers has been presented in Fig. 7.13. It represents that the amount of discharge per unit time increases as the Froude number increases. Since, the flight navigates farther in the same interval as the flight with lower speed travels, hence higher cascading rates and higher curtain densities can occur. The discharge rate increased by two folds when the Froude number increased by 4 times. However, the behavior of the curves has been observed similar in all the cases and also the maximum cascading rate occurs at the same discharge point.

To understand the influence of Froude number on the total surface area of the particles

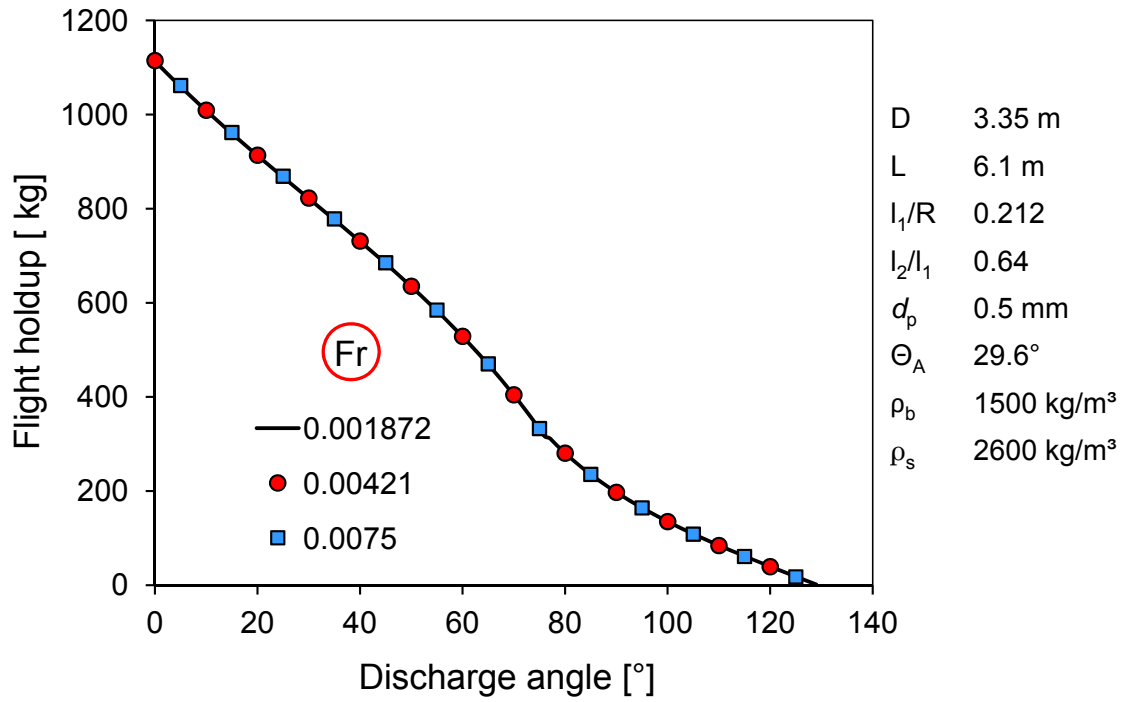


Figure 7.12: Influence of Froude number on flight holdup

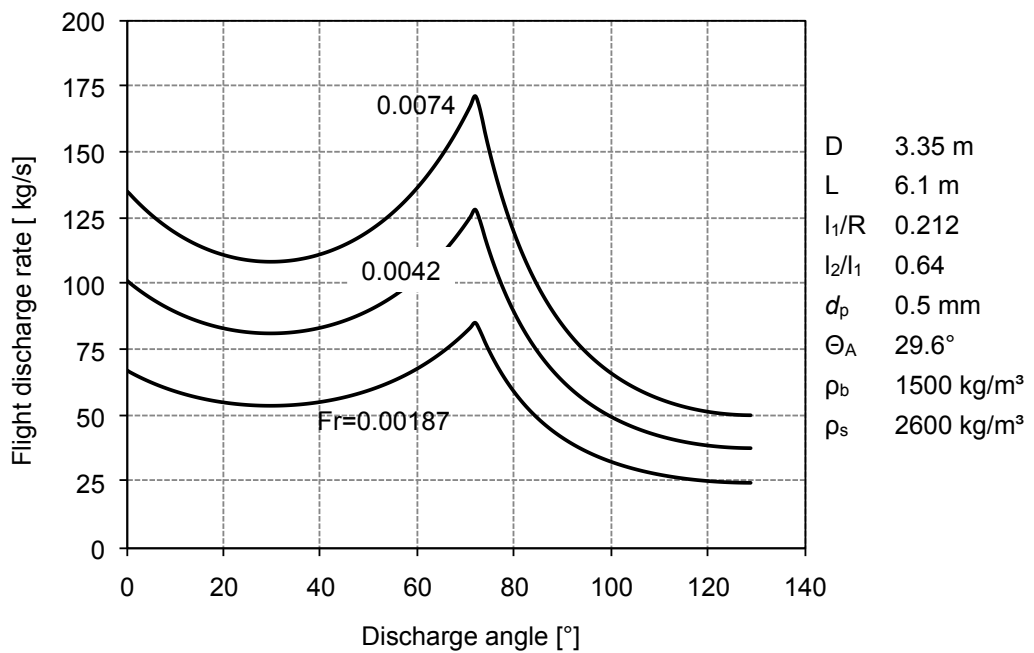


Figure 7.13: Influence of Froude number on flight discharge rate

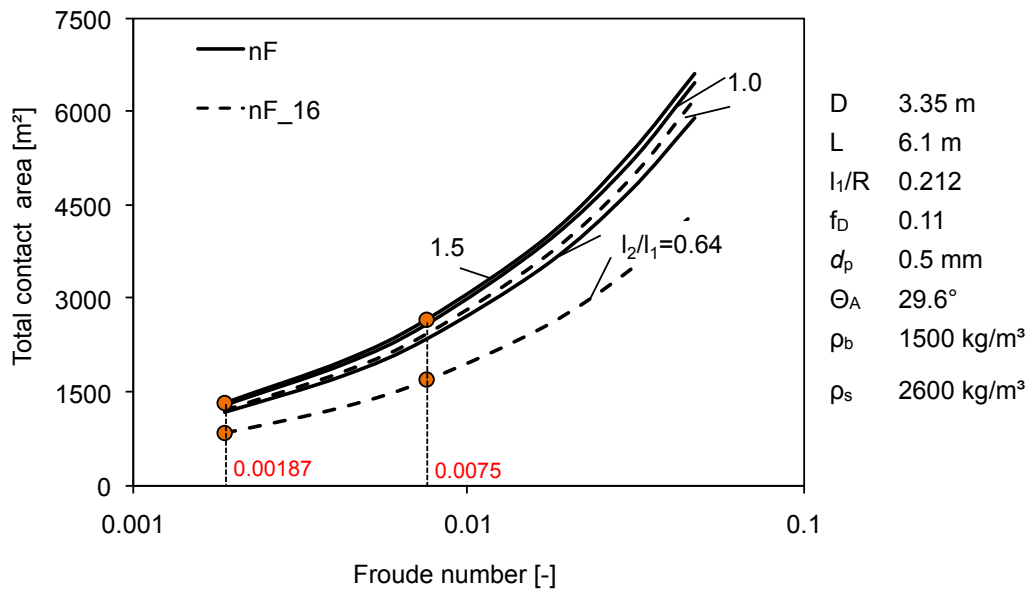


Figure 7.14: Influence of Froude number on total surface area of the particles in airborne phase

in the curtains, Fig. 7.14 is plotted at various flight length ratios. It can be observed that as the Froude number increases, the total particle surface area also increases due to increase in cascade rate and height of the curtain. The area increases steadily from 1181 m^2 at $Fr=0.0018$ to 2368 m^2 at $Fr=0.0075$ when $l_2/l_1 = 0.64$. However the increase at lower Froude number is not rapid as it is at higher Froude values. The figure also shows that as increasing the flight length ratio between 0.64 and 1.0 the surface area increases rapidly, where as the rate of increase decreases between 1.0 and 1.5. Further, the influence of flight number is also shown in the figure. The solid lines represent the model predictions when the number of flights are operated at theoretical number and the dashed lines represent when the number of flights are fixed at 16. In all the cases the surface area is always greater for the case of the theoretical number as compared to the fixed flight number. This is due to the fact that the active flights calculated during both the cases is greater for the theoretical number of flights as related to 16 flights case.

7.2.2 Dynamic angle of repose

Dynamic angle of repose is a material property, which depends on the moisture of the material. Highly cohesive solids expose higher dynamic angles, which is the case of high moistures material in dryers at the feed section. Therefore, the influence of this angle

on the contact area of gas to solids has to be studied thoroughly. The influence of this parameter over flight holdup, cascade rate, and the particles surface area of the airborne phase by fixing the particle diameter has been discussed in the following.

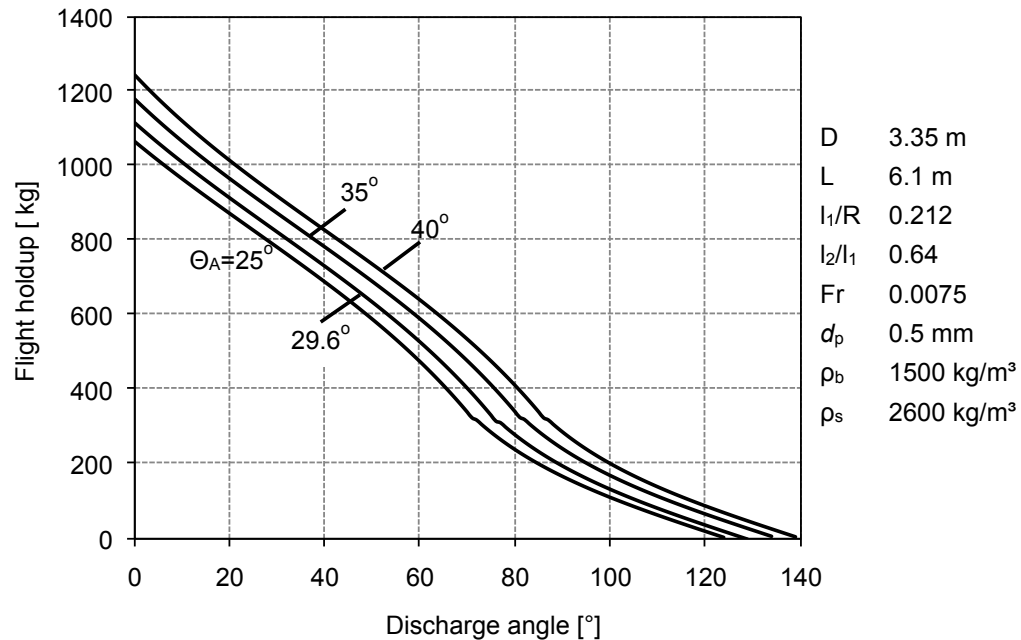


Figure 7.15: Influence of dynamic angle of repose on flight holdup

Figure 7.15 depicts the amount of material carried away by the flight at various dynamic angles. It indicates that the increase in the dynamic angle also increases the initial holdup of the flight at a constant drum filling degree and Froude number. The flight holdup is witnessed to be maximum for the material having high angle of repose at any discharge point. It is also observed that the flight is being emptied at higher discharge points at higher repose angles.

The influence of dynamic angle on the flight discharge rate has been shown in Fig. 7.16. As can be seen from the graph, the maximum discharge rate is not affected by the dynamic angle of repose. However, higher cascading rates were observed at higher dynamic angles during the initial period of discharge. The period of flight unloading is noticed longer for higher dynamic angles when compared to the smaller angles of repose. The surface area of particles in the curtains as a function of angle of repose is presented in Fig. 7.17 at $l_2/l_1 = 1.0$ and 0.64 . Two cases for the flight number had been shown for this purpose. Firstly the number of flights are calculated using the theoretical model shown with the solid lines, and secondly a constant number of flights are considered at 16 which is

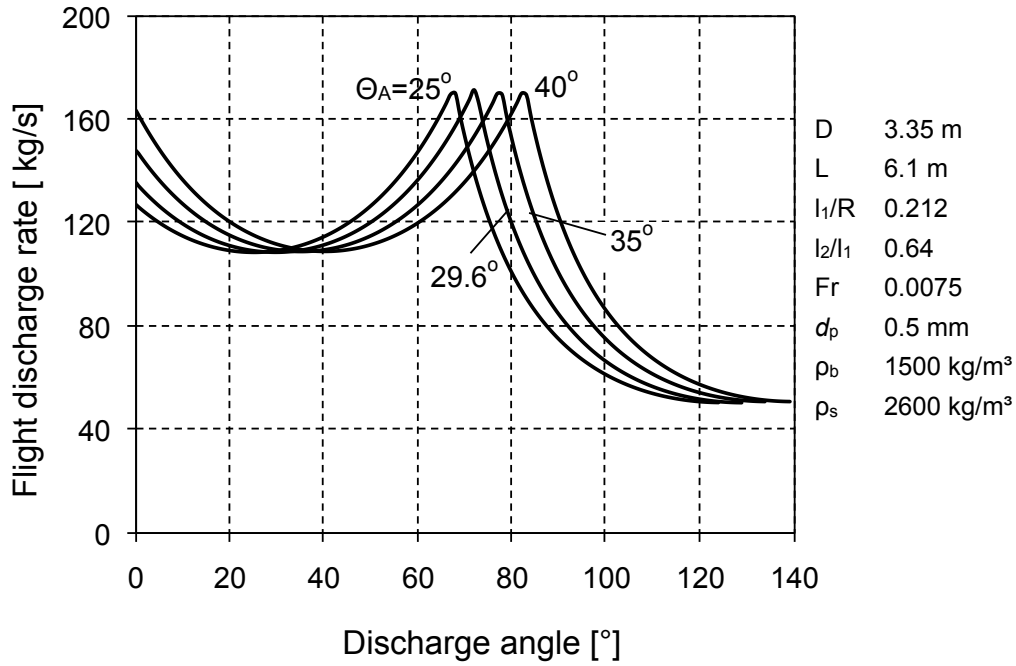


Figure 7.16: Influence of dynamic angle of repose on cascading rate of the flight

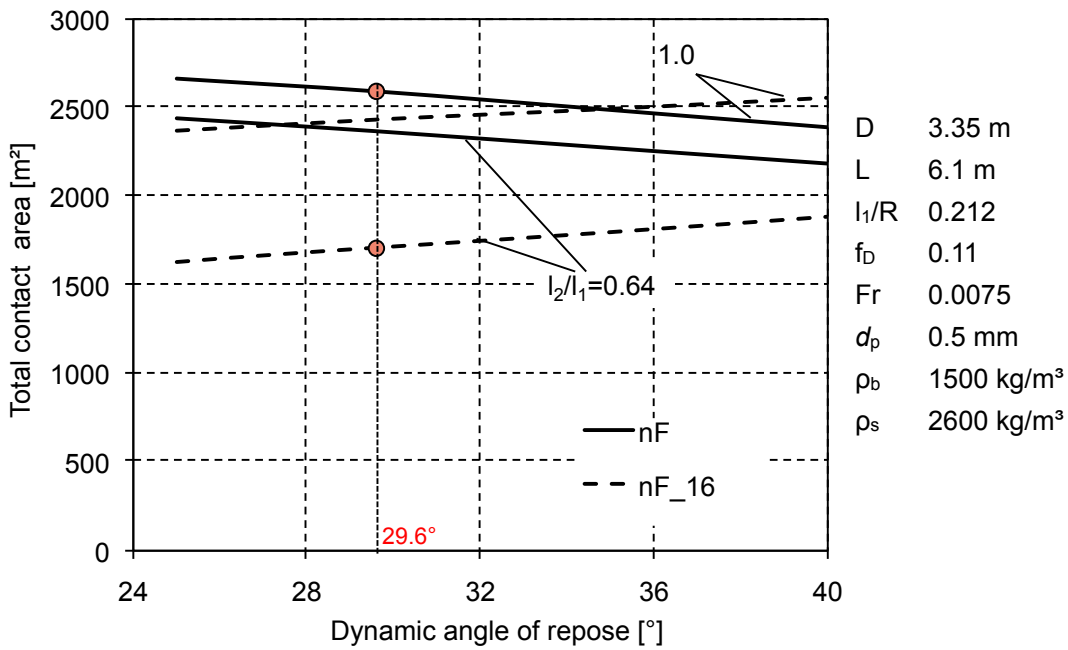


Figure 7.17: Influence of dynamic angle of repose on curtains total particle surface area

represented with dashed lines. It shows that increase in dynamic angle decreases the total surface area of the particles in the first case at any flight length ratio. It can be regarded due to the fact that increasing the dynamic angle decreases the number of active flights. As a result the number of curtains decreases. Whereas, in the second case increasing the angle of repose resulted an increase in the surface area at any flight length ratio, but this is not true in practice. Since, the flight holdup increases for an increase in dynamic angle, which then it should increase the allowed angular distance (see Fig. 3.10) between the two adjacent flights and results in decrease in number of flights. But while operating at fixed number of flights, this angular distance is kept constant and allowed to determine the flight holdup theoretically. Which then resulted an over predicted holdup according to the assumption that the flight is crowded with enough material at $\delta = 0^\circ$. This over prediction of flight holdup resulted in an increase in the surface area. Indeed at fixed flight number, and higher DAR the initial holdup (at $\delta = 0^\circ$) may be much smaller than the predicted.

7.2.3 Filling degree

Filling degree in rotary dryers is an important parameter which has to be studied thoroughly. It varies along the axial direction, due to the inclination of the drum and varying moisture levels of the material. Initially at the feed end section of the drum, the filling degree must be high enough to control the filling degree at the discharge end. During the transport from upstream end to downstream end the moisture from the material will be evaporated and hence the filling degree decreases. However, the filling degree does not vary much by considering a small section of the drum. Therefore in the current study the total filling degree was held constant and the influence of the filling degree on the curtain height and the contact area has been presented in this section.

Figure 7.18 represents the variation of the height of the curtains at different filling degrees operating in between 11-25%. As expected, the height of the curtain is always higher for the lower filling degrees due to small bed height present at the bottom of the drum, and the maximum point of curtain is observed at higher discharge points in case of higher filling degrees. Therefore, smaller filling degrees prevail better area of heat transfer due to larger contact times. Following this study, the influence of filling degree on the particle surface area is presented in Fig. 7.19. The figure depicts the influence of the flight length ratio and number of flights. From the figure, it is easy to understand that as less is the filling degree the higher is the particle surface area. However the filling

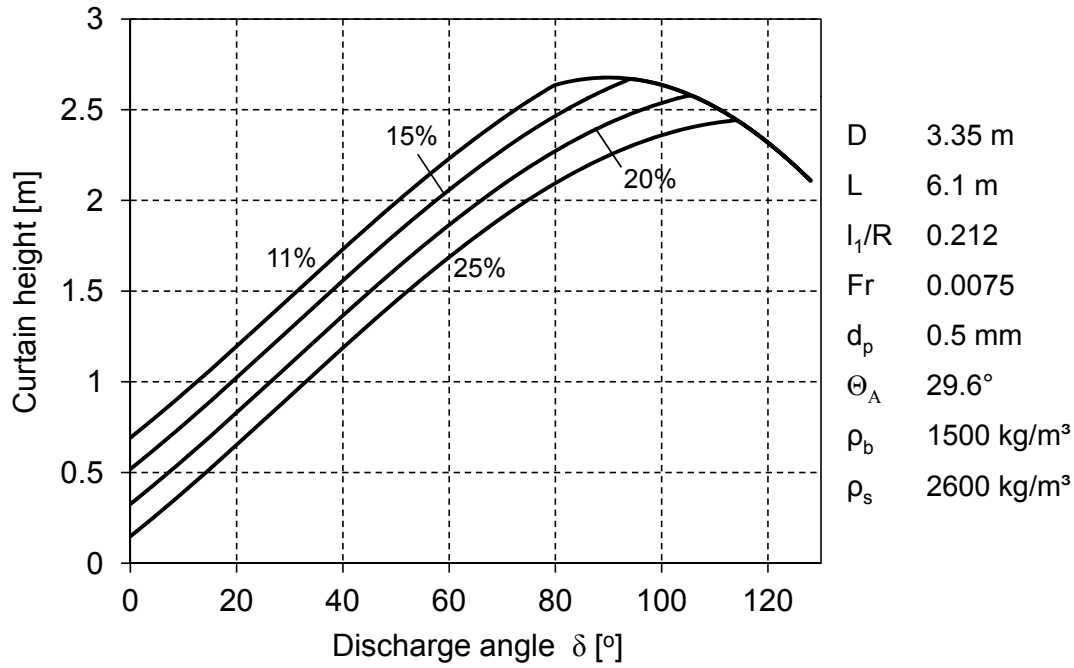


Figure 7.18: Influence of filling degree on the height of curtain

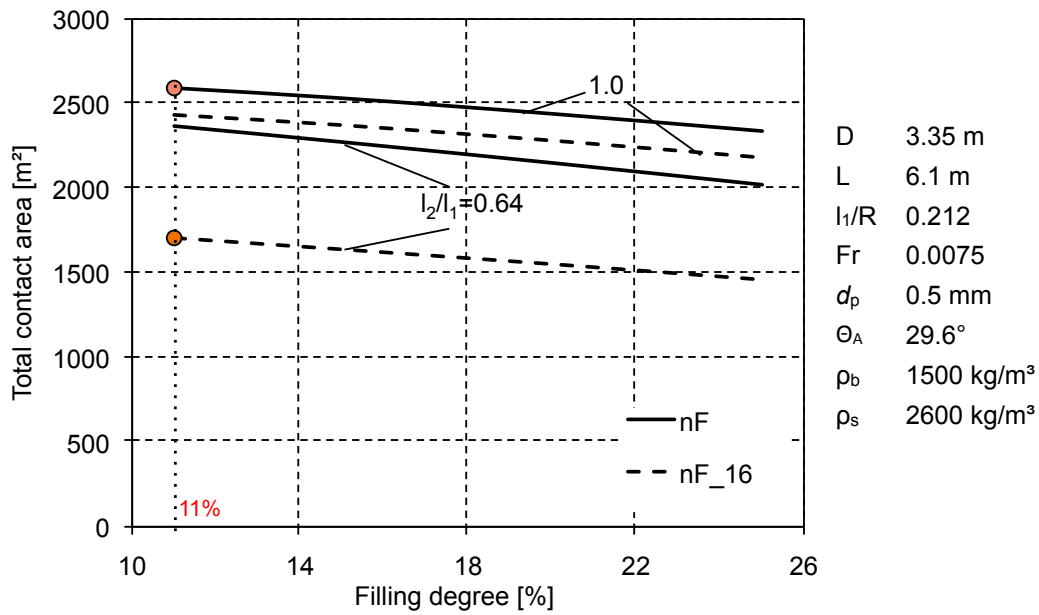


Figure 7.19: Influence of filling degree on total particle surface area of curtains

degree cannot decrease beyond the design loaded conditions, since further decrease in filling degree can lead to late discharge of the flight thus reducing the total surface area.

7.2.4 Flight length ratio

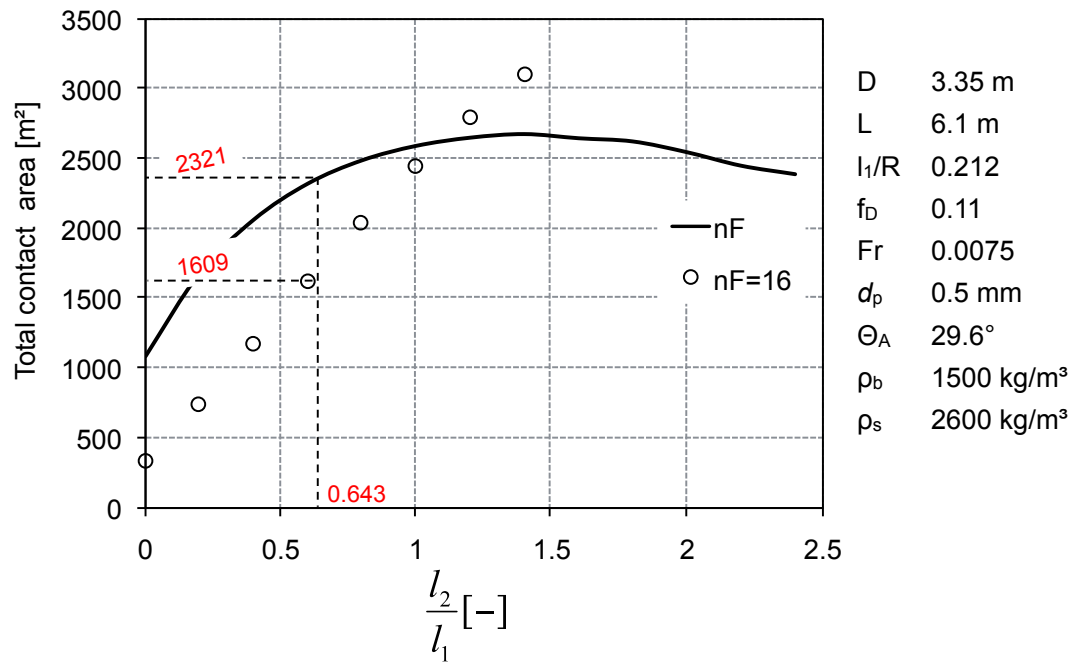


Figure 7.20: Influence of length ratio on total particle surface area in airborne phase

The influence of the tangential length on the total surface area of particles in the airborne phase has been investigated for two cases as shown in Fig. 7.20. In the first case theoretical number of flights are considered which is represented with the solid line. In the second case the number of flights are fixed at 16 depicted with (o) symbol. As the figure illustrates for $l_2/l_1 = 0.64$, the total area in the first case is 1.5 times higher than the second case. However, the area is almost equal when $l_2/l_1 = 1$, since the number of flights in the first case is almost close to 16. In the first case, the maximum area (2769 m^2) occurred at $l_2/l_1 = 1.4$, i.e. the area increased only by 1.4 times when the flight length ratio increased by 2.2. Therefore while designing the drum, this factor can be considered, since the higher ratios increases the cascading rates which then increases the shielding of the particles. In the second case this area increased linearly while fixing the flight number, the data is shown only until the flight length ratio of 1.5.

Chapter 8

Conclusions and Outlook

8.1 Conclusions

With the developed model it is possible to simulate the influence of process and operating parameters on the material distribution which include: a) drum diameter, b) flight length ratio (l_2/l_1), c) number of flights (n_F), d) filling degree, e) rotational speed, and f) dynamic angle of repose (Θ_A).

High initial unloading rates were observed at small l_2/l_1 , but the range of discharge was short when compared to higher l_2/l_1 . The use of higher flight length ratios revealed bulk movement of solids during the final stage of discharge, which can lead to poor performance.

The maximum contact area for heat and mass transfer was obtained at a flight length ratio of 1.5 presuming no gas flow conditions, and neglecting the particle shielding effect. Not much variation was observed for the contact area between the flight length ratio 1-1.5. Moreover, operating the drum at $l_2/l_1 > 1$ can lead to higher particle shielding effects due to higher curtain densities. Hence, the optimal design of the drum can be expected at flight length ratio close to 1 and the number of flights equal or slightly less than the theoretical number ($n_F \approx 18$). However, further investigation is necessary to confirm this tendency, as it was also dependent on the loading state of the drum.

Increasing the number of flights increases the contact area, while the drum was operated at flight number less than the theoretical number. In contrast to that, the experimental observations witnessed a vertical entrainment effect for quartz sand at higher flight number. At higher Froude numbers this effect further increases under the same operating conditions. It disturbs the uniformity of the curtains and can interfere with

the axial flow of dry air under practical conditions, which has to be addressed carefully while designing the drum. Therefore for very fine material a possible suggestion is to operate the drum at less number of flights (i.e. at higher flight length ratio's $l_2/l_1 \approx 1$) rather than at higher flight number.

The angle of repose of the material changes during the drying process due to varying levels of moisture along the axial transportation. The material behavior can be simulated with the developed model by accommodating the change in angle of repose. The experimental observations discussed in the thesis and the results presented from the geometrical model will serve as a bench mark to the field experience while scaling the drum to the industrial units.

Mellmann's final discharge angle model depicted fast discharges at higher Froude number, while the experimental observations showed late discharges indeed. This undesirable nature is addressed by the extended model in the present work. However, this approach suggested that there still exists an another region (4^{th}) of the unloading flight which can be regarded as a diluted phase that has to be incorporated further in the geometrical model.

8.2 Outlook

1. This study was focused only on the transverse distribution of material by considering constant filling degree of the drum in a given section. However, in flighted rotary drums the filling degree changes due to varying moisture levels of the solids along the length of the dryer. It is recommended that the geometrical transverse model can be coupled with the model of axial transport.
2. In this work no heat transfer studies were developed. As a next step it is recommended to study the heat and mass transfer effects both experimentally and theoretically. The predicted contact area from the geometrical model can be used as a basis for this work.
3. The extended model for kinetic angle of repose was in good agreement with the experiments as compared to Schofield and Glikin model. However before using this model completely, it is necessary to validate it further as it depends on the mean velocity and layer thickness. Since the mean velocity at the flight surface was formulated based on the Eulerian approach by assuming a linear velocity profile in the active layer. Further, it was also assumed that the coefficient of friction vary along the boundary line

with linear profile at each flight position. Therefore, the validation of this model is certainly necessary which was rather difficult to perform with the available experimental setup.

4. Angular flights are used in some sections of flighted rotary drums depending on the material behavior. The geometrical model presented in this work is easy to extend when compared to the models from other authors for studying the behavior of angular flights.

Bibliography

- [1] P. G. de Gennes. Granular matter: a tentative view. *Reviews of Modern Physics*, 71(2):374–382, 1999.
- [2] C. S. Bierwisch. *Numerical Simulations of Granular Flow and Filling*. PhD thesis, University of Freiburg, Germany., 2009.
- [3] GDR Midi. On dense granular flows. *The European Physical Journal E*, 14(4): 341–365, 2004.
- [4] P. Jop, Y. Forterre, and O. Pouliquen. A constitutive law for dense granular flows. *Nature*, 441(7094):727–30, 2006.
- [5] S. Longo and A. Lamberti. Grain shear flow in a rotating drum. *Experiments in Fluids*, 32(3):313–325, 2002.
- [6] Y. Forterre and O. Pouliquen. Flows of dense granular media. *Annual Review of Fluid Mechanics*, 40(1):1–24, 2008.
- [7] D. V. Khakhar, A. V. Orpe, P. Andresen, and J. M. Ottino. Surface flow of granular materials: model and experiments in heap formation. *Journal of Fluid Mechanics*, 441:255–264, 2001.
- [8] H. M. Jaeger and S. R. Nagel. Physics of the granular state. *Science*, 255:1523–1531, 1992.
- [9] V. Frette, K. Christensen, A. Malthe-Sørensen, J. Feder, T. Jøssang, and P. Meakin. Avalanche dynamics in a pile of rice. *Nature*, 379(6560):49–52, 1996.
- [10] H. Henein, J. K. Brimacombe, and A. P. Watkinson. Experimental study of transverse bed motion in rotary kilns. *Metallurgical Transactions B*, 14B:191–205, 1983.

-
- [11] J. Mellmann. The transverse motion of solids in rotating cylinders-forms of motion and transition behavior. *Powder Technology*, 118(3):251–270, 2001.
- [12] J. Mellmann and E. Specht. Mathematische Modellierung des Übergangsverhaltens zwischen den Formen der transversalen Schüttgutbewegung in Drehrohren, Teil 1. *ZKG International*, 54:281–296, 2001.
- [13] A. Boateng. Boundary layer modeling of granular flow in the transverse plane of a partially filled rotating cylinder. *International Journal of Multiphase Flow*, 24(3):499–521, 1998.
- [14] J. Mellmann. *Zonales Feststoffmassstrommodell für flammenbeheizte Drehrohrreaktoren*. PhD thesis, TU Magdeburg, Germany, 1989.
- [15] X. Liu, E. Specht, and J. Mellmann. Experimental study of the lower and upper angles of repose of granular materials in rotating drums. *Powder Technology*, 154(2-3):125–131, 2005.
- [16] Arun S. Mujumdar. Principles, classification, and selection of dryers. In A. S. Mujumdar, editor, *Handbook of Industrial Drying*, pages 4–31. Taylor & Francis Group, 3rd edition, 2007.
- [17] G.S.V. Raghavan, T.J. Rennie, P.S. Sunjka, V. Orsat, W. Phaphuangwittayakul, and P. Terdtoon. Overview of new techniques for drying biological materials with emphasis on energy aspects. *Brazilian Journal of Chemical Engineering*, 22(2):195–201, 2005.
- [18] C. M. Van't Land. *Industrial Drying Equipment Selection and Application*. Marcel Dekker, Inc., 1991.
- [19] R. B. Keey. *Drying of loose and particulate materials*. Hemisphere Publishing Corporation, A member of the Taylor & Francis Group, 1992.
- [20] A. R. Shirley, L. M. Nunnally, and F. T. Carney. Melt granulation of urea by the falling-curtain process. *Industrial & Engineering Chemistry Product Research and Development*, 21:617–620, 1982.
- [21] P. L. Douglas, A. Kwade, P. L. Lee, and S. K. Mallick. Simulation of a Rotary Dryer for Sugar Crystalline. *Drying Technology*, 11(1):129–155, 1993.

- [22] S. M. Savaresi, R. R. Bitmead, and R. Peirce. On modelling and control of a rotary sugar dryer. *Control Engineering Practice*, 9(3):249–266, 2001.
- [23] Y. Song, J. Thibault, and T. Kudra. Dynamic characteristics of solids transportation in rotary dryers. *Drying Technology*, 21(5):755–773, 2003.
- [24] P.F. Britton, P.A. Schneider, and M.E. Sheehan. Flight unloading in rotary sugar dryers. In *2004 Conference of the Australian Society of Sugar Cane Technologists held at Brisbane, Queensland, Australia, 4-7 May 2004.*, pages 1–7. PK Editorial Services Pty Ltd, 2004.
- [25] F. Geng, Z. Yuan, Y. Yan, D. Luo, H. Wang, B. Li, and D. Xu. Numerical simulation on mixing kinetics of slender particles in a rotary dryer. *Powder Technology*, 193(1):50–58, 2009.
- [26] O.O. Ajayi and M.E. Sheehan. Design loading of free flowing and cohesive solids in flighted rotary dryers. *Chemical Engineering Science*, 73:400–411, 2012.
- [27] A. J. Matchett and J. Baker. Particle residence times in cascading rotary dryers. part 1-derivation of the two-stream model. *J Separ Proc Technol*, 8:11–17, 1987.
- [28] S. J. Friedman and W. R. Marshall. Studies in rotary drying: Part 1 - holdup and dusting. *Chemical Engineering Progress*, 45:482– 573, 1949.
- [29] E.B. Arruda, J. M. F. Façanha, L. N. Pires, A.J. Assis, and M.A.S. Barrozo. Conventional and modified rotary dryer: Comparison of performance in fertilizer drying. *Chemical Engineering and Processing: Process Intensification*, 48(9):1414–1418, 2009.
- [30] A. Williams-Gardner. Industrial drying. In *Rotary Dryers*, chapter 7, pages 121–150. Chem. & Proc. Eng. Ser., London Hill, 1971.
- [31] F. Kneule. Trommeltrockner. In *Das Trocknen*, chapter 7, pages 289–303. Sauerlander AG, Aarau, 1975.
- [32] K. Kröll. Trockner und trocknungsverfahren. In *Trocknungstechnik*, volume 2, chapter 2, pages 444–461. Springer-Verlag, Berlin, 1978.
- [33] D. Green and R. Perry. In *Perrys Chemical Engineers Handbook*, chapter 12, pages 52–65. McGraw-Hill, New York, 6 edition, 1997.

- [34] E. Canales. Steady state modelling and simulation of an indirect rotary dryer. *Food Control*, 12(2):77–83, 2001.
- [35] P. Britton, M. Sheehan, and P. Schneider. A physical description of solids transport in flighted rotary dryers. *Powder Technology*, 165(3):153–160, 2006.
- [36] S. Shahhosseini, I. T. Cameron, and F. Y. Wang. A simple dynamic model for solid transport in rotary dryers. *Drying Technology*, 18(4):867–886, 2000.
- [37] C. G. J. Baker. The design of flights in cascading rotary dryers. *Drying Technology*, 6:4:631–653, 1988.
- [38] R. G. Sherritt, R. Caple, L. A. Behie, and A. K. Mehrotra. The movement of solids through flighted rotating drums. part i: Model formulation. *The Canadian Journal of Chemical Engineering*, 71(3):337–346, 1993.
- [39] M. Krokida, D. Marinos-Kouris, and Arun S. Mujumdar. Handbook of industrial drying. In A. S. Mujumdar, editor, *Rotary Drying*, pages 151–172. Taylor & Francis Group, 3rd edition, 2007.
- [40] C. G. Moyers and G. W. Baldwin. Psychrometry, evaporative cooling, and solids drying. In D. W. Green, editor, *Perry's Chemical Engineers Handbook*, chapter 12. McGraw-Hill, 7th edition, 1997.
- [41] S. E. Papadakis, T. A. G. Langrish, I. C. Kemp, and R. E. Bahu. Scale-up of cascading rotary dryers. *Drying Technology*, 12(1):259–277, 1994.
- [42] O.O. Ajayi and M.E. Sheehan. Application of image analysis to determine design loading in flighted rotary dryers. *Powder Technology*, 223:123–130, 2011.
- [43] F. R. Schofield and P. G. Glikin. Rotary dryers and coolers for granular fertilizers. *Trans. Inst. Chem. Eng.*, 40:183–190, 1962.
- [44] S. J. Porter. The design of rotary driers and coolers. *Trans. Inst. Chem. Eng.*, 41: 272–280, 1963.
- [45] J. J. Kelly and P. Ó Donnell. Dynamics of granular material rotary dryers and coolers. *ICE Symp Serial*, 29:33–41, 1968.
- [46] P. G. Glikin. Transport of solids through flighted rotating drums. *Trans. Inst. Chem. Eng.*, 56:120, 1978.

- [47] M. H. Lisboa, D. S. Vitorino, W. B. Delaiba, J. R. D. Finzer, and M. A. S. Barrozo. A study of particle motion in rotary dryer. *Brazilian Journal of Chemical Engineering*, 24(3):365–374, 2007.
- [48] J. J. Kelly. The kinetic angle of repose of powders. *Journal of the Society of Cosmetic Chemists*, 21(1):37–51, 1970.
- [49] A. Lee and M. E. Sheehan. Development of a geometric flight unloading model for flighted rotary dryers. *Powder Technology*, 198(3):395–403, 2010.
- [50] John. Kelly. Flight design in rotary dryers. *Drying Technology*, 10(4):979–993, 1992.
- [51] D. Revol, C. L. Briens, and J. M. Chabagno. The design of flights in rotary dryers. *Powder Technology*, 121(2-3):230–238, 2001.
- [52] F. Y. Wang, I. T. Cameron, and J. D. Litsler. Further theoretical studies on rotary drying processes represented by distributed systems. *Drying Technology*, 13(3):737–751, 1995.
- [53] W. Blumberg and E.-U. Schlünder. Transversale Schüttgutbewegung und konvektiver Stoffübergang in Drehrohren. Teil 2: Mit Hubschaufeln. *Chemical Engineering and Processing: Process Intensification*, 35(6):405–411, 1996.
- [54] D. Van Puyvelde. Modelling the hold up of lifters in rotary dryers. *Chemical Engineering Research and Design*, 87(2):226–232, 2009.
- [55] W.F. Cao and T.A.G. Langrish. Comparison of residence time models for cascading rotary dryers. *Drying Technology*, 17(4):825–836, 1999.
- [56] B. A. Smith. Factors influencing rotary dryer performance. *Transactions, American Institution of Chemical Engineers*, 38:251–257, 1942.
- [57] W. C. Saeman and T. R. Mitchell. Analysis of rotary dryer and cooler performance. *Chemical Engineering Progress*, 50(9):467–475, 1954.
- [58] A. J. Matchett and M. S. Sheikh. An improved model of particle motion in cascading rotary dryers. *Trans.Inst.Chem.Eng.*, 68(3):139–148, 1990.
- [59] F. Miskell and W. R. Marshall. A study of retention time in a rotary dryer. *Chemical Engineering Progress*, 52(1):35–38, 1956.

- [60] H. F. Johnstone and A. D. Singh. *Univ. Ill. Eng. Expt. Sta. bull*, 56:324, 1940.
- [61] J. D. Sullivan, C. G. Maier, and O. C. Ralston. Passage of solid particles through rotary cylindrical kilns. *U.S. Bureau of Mines Tech Paper 384*, page 44, 1927.
- [62] F. A. Kamke. *Engineering analysis of a rotary dryer: drying of wood particles*. PhD thesis, Dept. Forest Prod., Oregon State Univ., Corvdlis, 1984.
- [63] R. G. Sherritt, R. Caple, L. A. Behie, and A. K. Mehrotra. The movement of solids through flighted rotating drums. part ii solids-gas interaction and model validation. *The Canadian Journal of Chemical Engineering*, 72(2):240–248, 1994.
- [64] C. Wardjiman, A. Lee, M. Sheehan, and M. Rhodes. Behaviour of a curtain of particles falling through a horizontally-flowing gas stream. *Powder Technology*, 188(2):110–118, 2008.
- [65] C. Wardjiman, A. Lee, M. Sheehan, and M. Rhodes. Shape of a particle curtain falling in stagnant air. *Powder Technology*, 192(3):384–388, 2009.
- [66] F. A. Kamke and J. B. Wilson. Computer simulation of a rotary dryer. Part I: Retention time. *AIChE Journal*, 32(2):263–268, 1986.
- [67] A. J. Matchett and J. Baker. Particle residence times in cascading rotary dryers. part 2-application of the two-stream model to experimental and industrial data. *J Separ Proc Technol*, 9:5–13, 1988.
- [68] C. Duchesne, J. Thibault, and C. Bazin. Modeling of the solids transportation within an industrial rotary dryer: A simple model. *Industrial and Engineering Chemistry Research*, 35(7):2334–2341, 1996.
- [69] I. C. Kemp and D. E. Oakley. Simulation and scale-up of pneumatic conveying and cascading rotary dryers. *Drying Technology*, 15(6-8):1699–1710, 1997.
- [70] M. Renaud, J. Thibault, and A. Trusiak. Solids transportation model of an industrial rotary dryer. *Drying Technology*, 18(4):843–865, 2000.
- [71] S. Shahhosseini, I. T. Cameron, and F. Y. Wang. A dynamic model with on-line identification for rotary sugar drying processes. *Drying Technology*, 19(9):2103–2129, 2001.

- [72] M. Sheehan, P. Britton, and P. Schneider. A model for solids transport in flighted rotary dryers based on physical considerations. *Chemical Engineering Science*, 60(15):4171–4182, 2005.
- [73] K. Cronin, M. Catak, J. Bour, A. Collins, and J. Smee. Stochastic modelling of particle motion along a rotary drum. *Powder Technology*, 213(1-3):79–91, 2011.
- [74] F. A. Kamke and J. B. Wilson. Computer simulation of a rotary dryer. Part II: Heat and Mass Transfer. *AIChE J.*, 32(2):269–275, 1986.
- [75] F. Groves and T. H. Wu. Dynamic mathematical model of a rotary dryer: Method of characteristics. *Chemical Engineering Communications*, 49(1):35–49, 1986.
- [76] J. Hruby, R. Steeper, G. Evans, and C. Crowe. An experimental and numerical study of flow and convective heat transfer in a freely falling curtain of particles. *Journal of fluids engineering*, 110:172–181, 1988.
- [77] C. Shene, F. Cuhillos, R. Perez, and P.I. Alvarez. Modelling and simulation of a direct contact rotary dryer. *Drying technology*, 14(10):2419–2433, 1996.
- [78] J.R. Pérez-Correa, F. Cubillos, E. Zavala, C. Shene, and P. I. Álvarez. Dynamic simulation and control of direct rotary dryers. *Food Control*, 9(4):195–203, 1998.
- [79] F. T. Ademiluyi, M. F. N. Abowei, Y. T. Puyate, and S. C. Achinewhu. Effects of Drying Parameters on Heat Transfer during Drying of Fermented Ground Cassava in a Rotary Dryer. *Drying Technology*, 28(4):550–561, 2010.
- [80] F. Castaño, F. R. Rubio, and M. G. Ortega. Modeling of a cocurrent rotary dryer. *Drying Technology*, 30(8):839–849, 2012.
- [81] C. O. Miller, B. A. Smith, and W. H. Schuette. Factors influencing the operation of rotary dryers. part ii. the rotary dryer as a heat exchanger. *Trans. Am. Inst. Chem. Eng.*, (38):841–864, 1942.
- [82] H. Hirosue and A. S. Mujumdar. Effect of Particle Cascade From Flights on Heat Transfer and Pressure Drop in Rotary Dryers and Coolers. *Drying Technology*, 11(1):195–207, 1993.
- [83] H. Hirosue. Influence of particles falling from flights on volumetric heat transfer coefficient in rotary dryers and coolers. *Powder Technology*, 59(2):125–128, 1989.

- [84] C. Wardjiman and M. Rhodes. Heat transfer in a particle curtain falling through a horizontally-flowing gas stream. *Powder Technology*, 191(3):247–253, 2009.
- [85] R. A. Bagnold. Experiments on a gravity-free dispersion of large solid spheres in a newtonian fluid under shear. 225(1160):49–63, 1954.
- [86] H. M. Jaeger, C. Liu, S. R. Nagel, and T. A. Witten. Friction in granular flows. *Europhysics Letters*, 11(7):619–624, 1990.
- [87] J. M. N. T. Gray. Granular flow in partially filled slowly rotating drums. *Journal of Fluid Mechanics*, 441:1–29, 2001.
- [88] J. Mellmann and E. Specht. Particle motion, filling degree and surface area of the flying curtain in cascading rotary dryers. *EFCE Working Party on Drying, Magdeburg*, 2002.
- [89] Y. Ding, R. Forster, J. P. K. Seville, and D. J. Parker. Scaling relationships for rotating drums. *Chemical Engineering Science*, 56(12):3737–3750, 2001.
- [90] K. R. Sunkara, F. Herz, E. Specht, J. Mellmann, and R. Erpelding. Modeling the discharge characteristics of rectangular flights in a flighted rotary drum. *Powder Technology*, 234:107–116, 2013.
- [91] F. P. Beer, E. R. Johnston, D. F. Mazurek, P. J. Cornwell, and E. R. Eisenberg. *Vector mechanics for engineers: Statics and Dynamics*. McGraw-Hill, 9 edition, 2009.
- [92] P. Smith and R. C. Smith. *Mechanics*. John Wiley & Sons, 1995.
- [93] G. D. Riquelme and G. Navarro. *Analysis and Modeling of Rotatory Dryer - Drying of Copper Concentrate, Drying of Solids - Recent International Developments*. Wiley Eastern, New Delhi, mujumdar edition, 1986.
- [94] T. A. G. Langrish. *The mathematical modeling of cascading rotary dryers*. PhD thesis, University of Oxford, 1988.
- [95] I. Evripidis. *Kombinierte Kontakt- und Konvektionstrocknung in einem Trommeltrockner*. PhD thesis, Univ. Karlsruhe, Germany, 1991.
- [96] C. G. J. Baker. Air-solids drag in cascading rotary dryers. *Drying Technology*, 10(2):365–393, 1992.

-
- [97] C. G. J. Baker. Cascading rotary dryers. In A. S. Mujumdar, editor, *Advances in Drying*, pages 1–51. Hemisphere Publishing Co, 1983.
- [98] W. Blumberg. Selective Konvetions- und Kontakttdrocknung im Drehrohr. Fortschritt-Berichte. VDI series 3, VDI-Verlag 384, Düsseltdorf, 1995.
- [99] A. A. Boateng and P. V. Barr. A thermal model for the rotary kiln including heat transfer within the bed. *International Journal of Heat and Mass Transfer*, 39(10): 2131–2147, 1996.
- [100] K. R. Sunkara, F. Herz, E. Specht, and J. Mellmann. Influence of flight design on the particle distribution of a flighted rotating drum. *Chemical Engineering Science*, 90:101–109, 2013.
- [101] J. Mellmann, E. Specht, and X. Liu. Prediction of rolling bed motion in rotating cylinders. *AIChE Journal*, 50(11):2783–2793, 2004.
- [102] X. Liu. *Experimental and theoretical study of transverse solids motion in rotary kilns*. PhD thesis, Otto-von-Guericke-Universität Magdeburg, Germany, 2005.
- [103] J. Perron and R.T. Bui. Rotary cylinders: transverse bed motion prediction by rheological analysis. *The Canadian Journal of Chemical Engineering*, 70:223–231, 1992.
- [104] D. V. Khakhar, J. J. McCarthy, Troy Shinbrot, and J. M. Ottino. Transverse flow and mixing of granular materials in a rotating cylinder. *Physics of Fluids*, 9(1): 31–43, 1997.
- [105] T. Elperin and A. Vikhansky. Granular flow in a rotating cylindrical drum. *Europhysics Letters*, 42(6):619–624, 1998.

List of Publications

International Journals

- **Sunkara, K. R.**, Herz, F., Specht, E., Mellmann, J. and Erpelding, R, *Modeling the discharge characteristics of rectangular flights in a flighted rotary drum*. Powder Technology. 234, 107-116, 2013.
- **Sunkara, K. R.**, Herz, F., Specht, E. and Mellmann, J, *Influence of flight design on the particle distribution of a flighted rotating drum*. Chemical Engineering Science. 90, 101-109, 2013.

Conferences and Proceedings

- **Sunkara, K. R.**, Herz, F. and Specht, E, *Thermal fluctuations and heat transfer measurements in a externally heated rotary cylinder*. In: ASME/JSME 2011 8th Thermal Engineering Joint Conference, AJTEC, Honolulu, Hawaii, USA, 2011.
- **Sunkara, K. R.**, Mellmann, J., Herz, F. and Specht, E, *Theoretical and Experimental Analysis of the Optimal Surface Area of the Cascading Particles in a Flighted Rotating Drum*. In: 5th Asian Particle Technology Symposium, National University of Singapore, Singapore, 2012.
- **Sunkara, K. R.**, Herz, F., Mellmann, J. and Specht, E, *Influence of flight cascading rate on the particle distribution in a flighted rotary drum*. In: XXVI International Mineral Processing Congress, New Delhi, India, 2012.
- **Sunkara, K. R.**, Herz, F., Mellmann, J. and Specht, E, *Influence of flight cascading rate on the particle distribution in a flighted rotary drum*. In: 7th International Conference for Conveying and Handling of Particulate Solids - CHoPS 2012, Friedrichshafen, Germany, 2012.

Curriculum Vitae

First name	Koteswara Rao
Family name	Sunkara
Nationality	Indian
Date of birth	02-08-1984
Place of birth	Guntur, Andhra Pradesh, India.
Parents	S.V. Sankara Rao and S. Siva kumari
Marital status	Single
Email	koti.iitm555@gmail.com



1995 - 2001	HSE in Sri sai junior college, Tenali, AP, India.
2001 - 2005	Bachelor of Technology in Chemical Engineering, BEC Bapatla, Acharya Nagarjuna University, AP, India.
2005 - 2007	Master of Technology in Chemical Engineering, Indian Institute of Technology Madras, Chennai, TN, India.
2007 - 2009	Associate S/W developer in Sybrant technology, Chennai, India.
2009 oct - 2013	Ph.D study, ISUT, Otto von Guericke University, Magdeburg, Germany. under the guidance of Prof.Dr.-Ing. E. Specht and Dr.-Ing. J. Mellmann.